HU ISSN 2063-6997

GEOSCIENCES AND ENGINEERING

A Publication of the University of Miskolc

Volume 12, Number 1

Miskolc, University Press
2024

GEOSCIENCES AND ENGINEERING
A Publication of the University of Miskolc
Volume 12, Number 1
Miskolc, University Press
UNIVERSITY OF MISKOLC
FACULTY OF EARTH AND ENVIRONMENTAL SCIENCES & ENGINEERING
HU ISSN 2063-6997

TABLE OF CONTENTS

Brigitta Turai-Vurom, Mihály Dobróka:
Joint inversion of laboratory-measured acoustic phase velocity and quality factor data 5

Tamás Bacsó, Márton Tóth:
Investigation of heavy metals desorption enhancement procedures in low-permeability contaminated soils 20

Okoli Emeka Austin, Agbasi Okechukwu Ebuka, Akaolisa Casmir Chukwuemeka Zanders, Ikoro Diugo Okereke, Ubechu Bridget Odochi, Ifeanyichukwu Kenechukwu Agbonma, Onyeawuna Uzochi Bright:
Investigation of groundwater potential utilizing geospatial techniques in owerri, Nigeria 30

Khouloud Jlaiel:
Exploring fourier transformations: benefits, limitations, and applications in analyzing two-dimensional right rectangular prism's magnetic field 57

Franklin Gómez, Marianna Vadászi:
Exploring uncertainty in flow unit identification and permeability prediction 75

Hadeer Hassan:
Comparison of different rock physics models for acoustic velocity 88

Maen Alwahsh, Gábor Mucsi:
Recycling techniques for crystalline silicon and thin film PV panels: an overview 100

Mahdi Dashti, Zoltán Virág:
Analysis of the earthquake impact on urban tunnels using modelling in phase 2 software 119

Tünde Edit Dobróka, István Szűcs, Mihály Dobróka:
Edge detection of tomographic images using traditional and deep learning tools 125

József Garai, Zsolt Vadai, Imre Kovács:
Why failures in geotechnics are less frequent than predicted 139

Geosciences and Engineering, Vol. 12, No. 1 (2024), pp. 5–19.
https://doi.org/10.33030/geosciences.2024.01.001

JOINT INVERSION OF LABORATORY-MEASURED ACOUSTIC PHASE VELOCITY AND QUALITY FACTOR DATA

BRIGITTA TURAI-VUROM[1]*, MIHÁLY DOBRÓKA[2]
[1]**Institute of Exploration Geosciences, Department of Geophysics, University of Miskolc,*
brigitta.vurom@gmail.com
[2]*Institute of Exploration Geosciences, Department of Geophysics, University of Miskolc,*
dobrokam48@gmail.com
[1]*https://orcid.org/0000-0001-7483-6458*
[2]*https://orcid.org/0000-0003-3956-2070*

Abstract: The paper presents a new rock-physical model to describe the pressure dependences of the phase velocity and quality factor (Q). Acoustic laboratory data for P-wave velocity and Q factor were measured on the sandstone sample at 40 different pressures. The spectral ratio method was used to measure the Q factor data utilizing an aluminum sample (with the size and geometry of the rock sample) as a reference. The measured velocity and Q factor data were processed in an inversion procedure. The results showed that both the velocity-pressure and the Q factor pressure dependence can be well-described utilizing the newly developed rock-physical model in forward modeling. From the estimated inversion parameters, v_p and Q can be calculated for the full pressure range.

Keywords: *model development, acoustic P wave velocity, quality factor, inversion, pressure dependence*

1. INTRODUCTION

There is a growing claim to predict rock physical parameters more accurately at various geological structures. Geophysics has a wide palette to determine these parameters, for example, acoustic velocity, porosity, permeability, and elastic moduli and it is well-known that pressure has a strong influence on them. The change of acoustic wave velocity propagating in rocks under pressure is highly nonlinear. To explain the phenomenon various models and empirical relations were developed.

It is observed that pressure has more influence on velocities in the beginning phase of loading, later it lessens and the velocities tend to have a limit value. The basic concepts link the pressure dependence of velocity and Q factor to the change in pore volume or closure of microcracks due to the increasing load, as Birch (1960) or Brace and Walsh (1964) proposed in their studies. This paper focuses on a combination of the two concepts because they simultaneously occur under real petrophysical conditions. When increasing pressure acts on rock, the microcracks are closing and at the same time grains become closer to each other (compaction occurs in the grain structure). Both the closing of the microcracks and the decrease in pore volume cause an increase in the propagation velocity and Quality factors. In the knowledge of the pressure dependence, we can estimate the pressure (pore pressures)

under real condition (Dócs and Baracza, 2022; Nagy et al., 2019a; Nagy et al., 2019b). In what follows the combined petrophysical model will be presented. The model will be validated in its application in the interpretation of laboratory-measured velocity- and Q-factor data.

2. THE COMBINED ROCK-PHYSICAL MODEL

There are two basic ideas to explain the pressure dependence of the propagation characteristics of seismic waves: Brace and Walsh (1964) declared that the main factor is the closure of the microcracks, while Birch (1960) suggested a mechanism in which an increasing pressure produces a reduction in the pore space followed by the increasing contact between the grains of the rock. Following Brace and Walsh (1964) a rock-physical model was introduced by Dobróka and Somogyi-Molnár (2012) while the model based on the concept of Birch (1960) was published by Somogyi Molnár et al. (2015). In real rock conditions both two mechanisms (microcracks closure and pore volume reduction) can occur, thus in the following we present a combined petrophysical model based on the results of Dobróka and Somogyi-Molnár (2012) and Somogyi Molnár et al. (2015).

2.1. The microcracks model

The basic assumption of the proposed model is that the *dN* change in the number of microcracks is directly proportional to the applied stress increase $d\sigma$ and the *N* total number of microcracks (per unit volume) expressed by the differential equation

$$dN = -\lambda N d\sigma \tag{1}$$

where λ is a proportionality constant. In *Equation (1)* the negative sign represents that at increasing stress – with closing microcracks – the number of the open microcracks decreases. Solving *Equation (1)* we find

$$N = N_0 \, exp(-\lambda\sigma) \tag{2}$$

where N_0 is the number of the open microcracks at a stress-free state $(\sigma = 0)$. The second item of building the model is the assumption of a linear relationship between the propagation velocity change *dv* – due to pressure increment $d\sigma$ – and *dN*

$$dv = -\alpha dN \tag{3}$$

where α is amaterial quality dependent constant. The negative sign represents that the velocity is increasing with decreasing number of cracks. Combining *Equation (3)* with *Equation (1)* and *(2)*, we obtain

$$dv = \alpha\lambda N_0 \, exp(-\lambda\sigma) d\sigma. \tag{4}$$

Solving the upper differential equation we have

$$v = K - \alpha N_0 \, exp(-\lambda\sigma) \tag{5}$$

where K is an integration constant. At a stress-free state ($\sigma = 0$) the propagation velocity v_0 can be measured and computed from *Equation (5)* as $v_0=K-\alpha N_0$. Hence, we obtain the integration constant as $K=v_0+\alpha N_0$. After this *Equation (5)* can be re-written as

$$v = v_0 + \Delta v(1 - exp(-\lambda\sigma)) \tag{6}$$

where the notation $\alpha N_0 = \Delta v$ has been used. *Equation (6)* provides a theoretical connection between the propagation velocity and rock pressure. The model equation shows that the propagation velocity – as a function of stress – starts from v_0 and increases up to the $v_{max}=v_0+\Delta v$ value according to the function of $1-exp(-\lambda\sigma)$. Thus, the value $\Delta v = v_{max} - v_0$ specifies a velocity range in which the propagation velocity can vary from the stress-free state up to the state characterized by high rock pressure. Constant λ is called the stress sensitivity.

2.2. The pore volume model

In accepting the idea of Birch (1960), the rock physical model explaining the physical relationship between the applied stress and the acoustic P-wave velocities is summarized here following Somogyi Molnár et al. (2015). Utilizing similar considerations as above, the basic model law can be formulated by *Equation (7)*

$$dV = -\gamma V d\sigma \tag{7}$$

where dV is the change of specific pore volume, $d\sigma$ is the applied stress increase and γ is the proportionality factor, a new rock physical parameter. The negative sign indicates that the pore volume is decreasing at increasing pressure. The solution to *Equation (7)* is

$$V = V_0 \, exp(-\gamma\sigma) \tag{8}$$

We assume also a linear relationship between the infinitesimal change of the appropriate propagation wave velocity dv and dV

$$dv = -\beta dV \tag{9}$$

where the β proportionality factor is a new material characteristic. The negative sign represents that the velocity and pore volume are inversely proportional. Combining *Equations (7)* and *(8)* and solving the differential equations as well as applying the notation $\Delta v_0=\beta V_0$ one can obtain

$$v = v_0 + \Delta v_0(1 - exp(-\gamma\sigma)) \tag{10}$$

where v_0 is the propagation velocity at a stress-free state, while the quantity Δv_0 means the velocity change caused by the presence of pores at a stress-free state (Ji et al., 2007) and can be considered as the difference between the velocities measured at maximum and zero stresses, i.e., $\Delta v_0 = v_{max} - v_0$.

The physical meaning of parameter γ was derived by Dobróka and Somogyi-Molnár (2012). It can be formulated as the logarithmic stress sensitivity of the velocity-change

$$S(\sigma) = -\frac{1}{\Delta v}\frac{d\Delta v}{d\sigma} = -\frac{d\,ln(\Delta v)}{d\sigma} = \gamma \tag{11}$$

2.3. The combined velocity model

If the two mechanisms are present, the infinitezimal velocity change should contain both sources of the stress-induced variation as

$$dv = -\alpha dN - \beta dV \tag{12}$$

or differentiating *Equations (2)* and *(8)*

$$dv = \alpha\lambda N_0 exp(-\lambda\sigma)d\sigma + \beta\gamma V_0\, exp(-\gamma\sigma)d\sigma \tag{13}$$

After integration, we can find

$$v = -\alpha N_0 exp(-\lambda\sigma) - \beta V_0\, exp(-\gamma\sigma) + C \tag{14}$$

where C is an integration constant determined using the initial condition that at stress-free state $(\sigma = 0)$ the propagation velocity is v_0

$$v_0 = -\alpha N_0 - \beta V_0 + C \tag{15}$$

resulting in

$$C = v_0 + \alpha N_0 + \beta V_0 \tag{16}$$

and also

$$v = v_0 + \alpha N_0(1 - exp(-\lambda\sigma)) + \beta V_0(1 - exp(-\gamma\sigma)) \tag{17}$$

This is the derived formula for the combined rock physical model.

The experiences show, that in most cases closing pores requires much higher pressure compared to the closing of microcracks, or in other words, the characteristic pressure $1/\gamma$ of the mechanism of closing the pores is much higher compared to $1/\lambda$ (the characteristic pressure belonging to the mechanism of closing microcracks). This means that in *Equation (17)*

$$\gamma\sigma \leq\leq \lambda\sigma \tag{18}$$

In such cases, *Equation (17)* can be simplified, because at moderate pressures the second exponential function can be replaced by its truncated Taylor series as

$$exp(-\gamma\sigma) \cong 1 - \gamma\sigma \tag{19}$$

Inserting this into *Equation (17)* we find

$$v = v_0 + \alpha N_0(1 - exp(-\lambda\sigma)) + \beta V_0\gamma\sigma \tag{20}$$

or introducing the notations $\alpha N_0 = \Delta v$ and $D = \beta V_0\gamma$ we find a simplified model equation

$$v = v_0 + \Delta v(1 - exp(-\lambda\sigma)) + D\sigma \tag{21}$$

This relationship is extensively used in rock physics as an empirical equation, e.g., in Ji et al. (2007), Wepfer and Christensen (1991), Wang et al. (2005), Stierman et al. (1979), Yu et al. (1993), etc. The above considerations can serve as theoretical background behind a previously introduced empirical formula.

2.4. The combined Q-factor model

We assume that the pressure dependence of the Q factor is influenced by the same intrinsic mechanisms (closing of microcracks and change in the pore volume) as it was assumed in the case of phase velocity. Consequently, the infinitezimal change in the Q factor should contain both sources of the stress-induced variation as

$$dQ = -\eta dN - \kappa dV \tag{22}$$

where the proportionality factors η and κ are new material characteristics. After differentiating *Equations (2)* and *(8)* we find

$$dQ = \eta\lambda N_0 exp(-\lambda\sigma)d\sigma + \kappa\gamma V_0\, exp(-\gamma\sigma)d\sigma \tag{23}$$

Repeating the above derivations, the final result is

$$Q = Q_0 + \eta N_0(1 - exp(-\lambda\sigma)) + \kappa V_0(1 - exp(-\gamma\sigma)) \tag{24}$$

where Q_0 is the Q factor at zero pressure. This is the combined Q factor formula. If the inequality (18) fulfills, *Equation (24)* simplifies as

$$Q = Q_0 + \Delta Q(1 - exp(-\lambda\sigma)) + E\sigma \tag{25}$$

where the notations $\Delta Q = \eta N_0$ and $E = \kappa V_0 \gamma$ were used. In the case of $\eta N_0 \leq\leq \kappa V_0$, *Equation (25)* gives the model assuming one mechanism

$$Q = Q_0 + \Delta Q(1 - exp(-\lambda\sigma)) \tag{26}$$

3. MEASUREMENTS AND INVERSION

To confirm the reliability of the combined model velocity, Q factor datasets were measured. The pulse transmission technique was used for wave velocity measurements and the method developed by Toksöz et al. (1979) was implemented to determine Q factor (see Appendix). We performed measurements on a fine-grained sandstone sample which was subjected to uniaxial stresses by the automatic acoustic test system of the Department of Geophysics, University of Miskolc *(Figure 1)*.

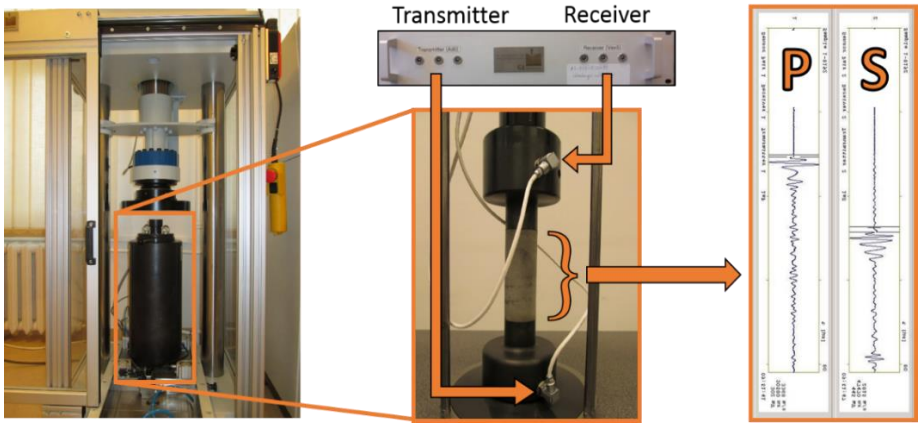

Figure 1

Experimental setup. Left: load frame and pressure cell. Middle: ultrasonic device, sandstone sample between transmitter and receiver built in the pressure stamps. Right: P and S wave arrivals

The digitally controlled test system includes a pressure cell, an ultrasonic 2-channel testing device and a load frame. P-wave velocity and Q factor – as a function of pressure – were measured at 40 discrete pressures equidistantly distributed in the [0.26, 82.15] (MPa) range. According to the Toksöz method (1979), the full waveform was also measured on the reference aluminum sample at all 40 discrete pressures. We determined the P-wave derived Q factor (Q) of the sandstone sample by

calculating spectral ratios from the spectra obtained after Discrete Fourier Transformation (DFT) of the measured waveforms. (The details are presented in the Appendix.) The measured data are shown in *Figure 2*. The velocity dataset shows a linear trend at higher pressures [following *Equation (21)* while the Q factor approaches to a constant value written in *Equation (26)*] or to a slightly increasing one *[Equation (26)]*.

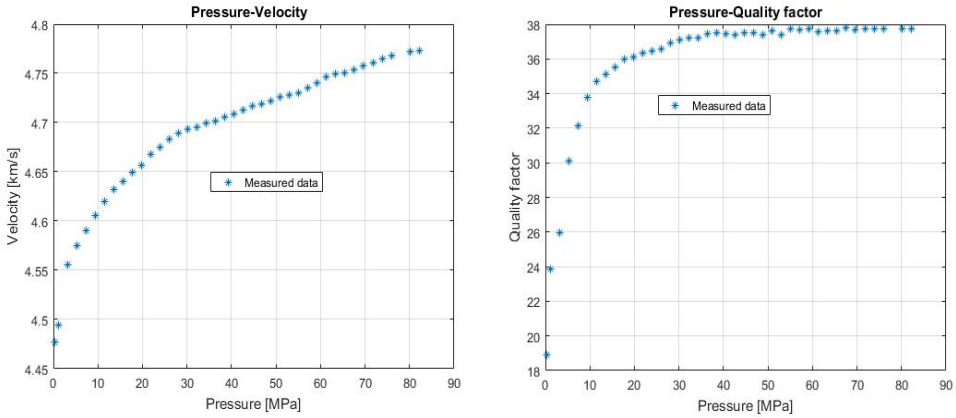

(a) (b)

Figure 2

The measurement data: a.) P-wave velocity, b.) P-wave Q factor

To prove the validity and applicability of the models introduced above, we use the measured datasets in an inversion procedure. The parameters appearing in the model equations will be determined by processing measurement data in both independent and joint inversion procedure (using the Damped Least Squares Method). In forward modeling it is obvious to choose the simplified combined model in the case of the velocity data. Because of the moderate increase of the Q factor at high pressures both the simplified combined and the one-mechanism model can be applied. For joint inversion purposes, it is useful to modify slightly the forward problem formulae and write *Equation (21)* in the form

$$v = A - Bexp(-\lambda\sigma)) + D\sigma \tag{27}$$

where $A = v_0 + \Delta v$, $B = \Delta v$. Similarly, *Equation (25)* is written in the form

$$Q = A - Bexp(-\lambda\sigma)) + E\sigma \tag{28}$$

where $A = Q_0 + \Delta Q$, $B = \Delta Q$. In the case of the one-mechanism model, *Equation (26)* is written as

$$Q = A - Bexp(-\lambda\sigma)) \tag{29}$$

For measuring the accuracy of inversion estimation, the relative estimation error is used (Menke, 1984; Gyulai et al., 2013). To characterize the fit between the measured and calculated data the relative data distance

$$d = \sqrt{\frac{1}{N}\sum_{k=1}^{N}\left(\frac{d_k^{(\mathrm{meas})}-d_k^{(\mathrm{calc})}}{d_k^{(\mathrm{calc})}}\right)^2} \cdot 100\ [\%] \tag{30}$$

is utilized. The result of the independent LSQ inversion of the P-wave velocity data is shown in *Figure 3*.

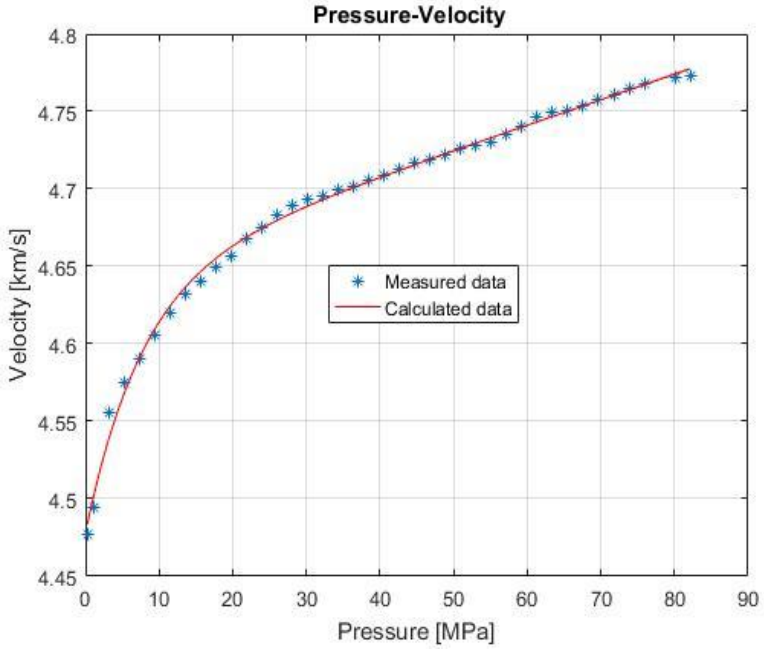

Figure 3
Inversion of P-wave velocity data using the simplified combined model [Equation (27)] in forward modeling

The estimated model parameters and the relative data distance are given in the first column of *Table 1*. In the inversion of Q factor data, we investigated two cases in selecting forward modeling. The results of the LSQ inversion with *Equation (28)* as a forward modeling formula are shown in *Figure 4*. The estimated model parameters are in the second column of *Table 1*. We can see that the value of the data distance is much larger for the Q factor than for the velocity, the reason is that the measured Q factor data are much less accurate than the velocity data, i.e., the *Q* dataset is much noisier than the *v* dataset.

Table 1

Model parameters estimated by independent LSQ inversion

Velocity inversion	Quality factor inversion I. using the combined model	Quality factor inversion II. using the one mechanism model
A = 4.642 +/– 0.071%	A = 36.582 +/– 0.609%	A = 37.473 +/– 0.231%
B = 0.165 +/– 2.447%	B = 17.382 +/– 2.038%	B = 17.941 +/– 2.030%
lambda = 0.129 +/– 5.72%	lambda = 0.181 +/– 4.74%	lambda = 0.158 +/– 3.99%
D = 0.0016 +/– 3.452%	E = 0.0168 +/– 24.33%	
d = 0.094%	d = 1.604%	d = 1.797%

In the other case, when *Equation (28)* serves as a forward modeling formula the results shown in *Figure 5* can be found. The estimated model parameters are in the third column of *Table 1*. As can be seen, the fit between the measured data is better in *Figure 4*.

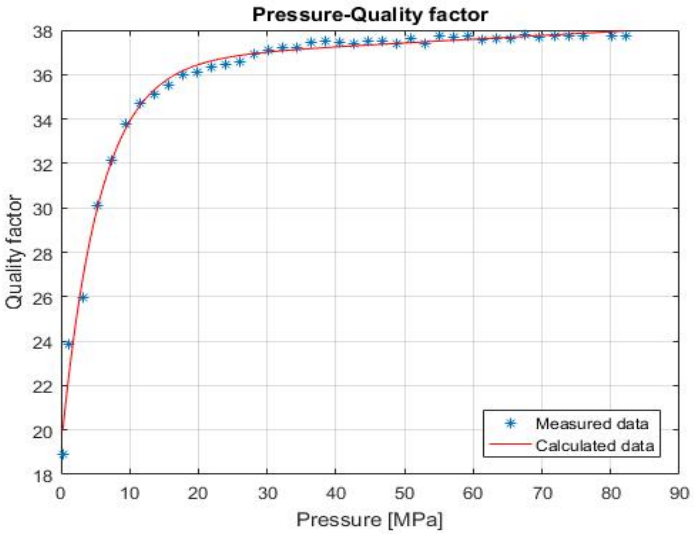

Figure 4

Inversion of P-wave Q factor data using the simplified combined model [Equation (28)] in forward modeling

The above results of independent inversion gave three different values for the lambda parameter. On the other hand, all three rock physical models in the above inversion tests were based on *Equation (1)*, which implies the same value for the lambda parameter. Because of this reason, we integrate the velocity- and Q factor datasets in a joint inversion procedure in which the connection of the two physically different kinds of measurement data set is based on the common lambda parameter.

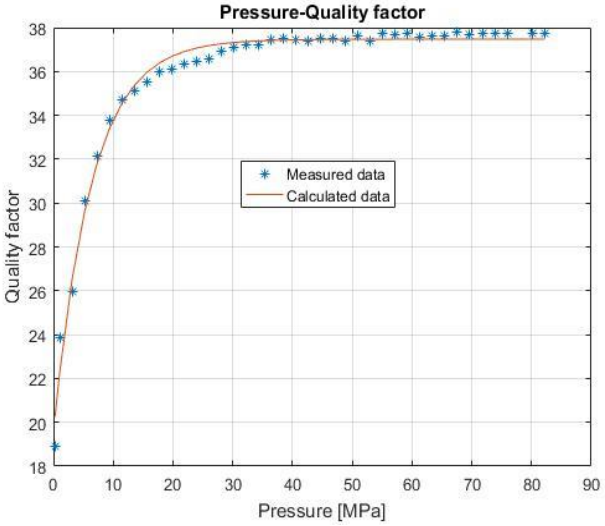

Figure 5
Inversion of P-wave Q factor data using the one mechanism model [Equation (29)] in forward modeling

In the joint inversion procedure, *Equation (27)* and *(28)* were selected as forward modeling formulae. The results are shown in *Figures 6* and *7*, the estimated parameters are given in *Table 2*.

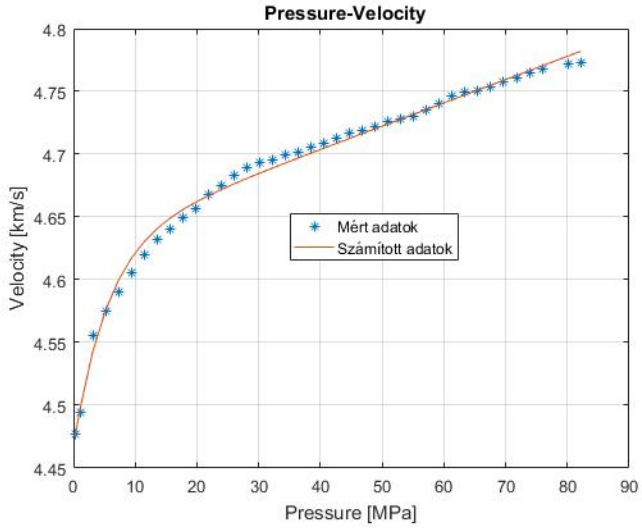

Figure 6
P-wave velocity as a function of pressure estimated by joint inversion using the simplified combined models [Equations (27) and (28)] in forward modeling

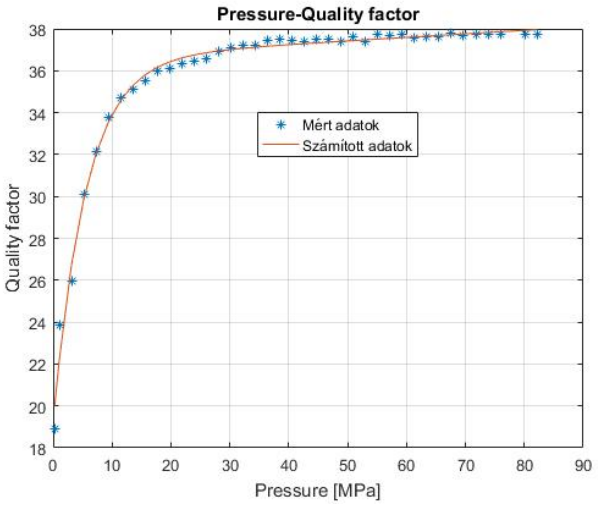

Figure 7

P-wave Q factor as a function of pressure found in joint inversion, using the simplified combined models [Equations (27) and (28)] in forward modeling

Table 2

Model parameters estimated by LSQ joint inversion

velocity parameters	Q factor parameters	Common parameter
Av = 4.629	Aq = 36.582	lambda = 0.180
Bv = 0.163	Bq = 17.382	
Dv = 0.0019	Eq = 0.0168	data distance: d = 1.137%

With the above model parameters, the pressure-dependent acoustic P-wave velocity and Q factor can be calculated for the whole pressure range by *Equations (27)* and *(28)*. The distance between the measured and calculated data is smaller, then that found in independent Q factor inversion and grater then that given by independent velocity inversion. The inversion results prove that the petrophysical model describing the pressure dependence of acoustic P-wave velocity and Q factor applies well in practice.

4. CONCLUSIONS

A fine-grained compact sandstone sample was used to measure the acoustic laboratory data of P-waves at 40 different discrete pressures in the [0.26, 82.15] (MPa) range, from which velocity-pressure and quality factor-pressure relationships were described. The spectral ratio method was used to determine the quality factor. To describe the velocity-pressure and quality factor-pressure relationships of the sandstone sample, a rock physics model is given that assumes the simultaneous presence of two mechanisms (closing of microcracks and change in the pore volume). The

measured data were processed by inversion procedures and then integrated into a joint inversion procedure in order to combine the two physically different types of measurement data sets using the lambda unknown as common parameter, assuming that the pressure dependence of the quality factor is affected by the same intrinsic mechanisms as the pressure dependence of the P-wave velocity. Using the model parameters estimated by joint inversion, the pressure-dependent acoustic P-wave velocity and the quality factor can be calculated for the full pressure range, based on the forward equations. The inversion results demonstrate that the petrophysical model explaining the pressure dependence of the acoustic P-wave velocity and the quality factor is well applicable. Based on the results of the inversion calculation, it can be stated that joint inversion significantly reduces the data distance for Q factor inversions.

ACKNOWLEDGEMENTS

The research was carried out in project No. K-135323 supported by the National Research, Development and Innovation Office (NKFIH).

APPENDIX

For the laboratory determination of the quality factor (Q), Toksöz et al. (1979) developed the method of spectral ratios, which was used to evaluate our acoustic P-wave measurements. During the method of spectral ratios, we also perform a reference measurement on an aluminum sample with the same geometry as the rock sample, since the Q factor of aluminum is very high, and we can use this property well in our calculations. The amplitude spectra of the acoustic waves that can be measured on the samples can be written with the following relations

$$\boldsymbol{A_{alu}(f) = G_{alu}(x) e^{-\alpha_{alu}(f)x} e^{j(2\pi f t - k_{alu}x)}} \tag{31}$$

$$\boldsymbol{A_{rock}(f) = G_{rock}(x) e^{-\alpha_{rock}(f)x} e^{j(2\pi f t - k_{rock}x)}} \tag{32}$$

where $A_{alu}(f)$ – amplitude spectrum of the aluminum sample,
$A_{rock}(f)$ – amplitude spectrum of the sandstone sample,
$G_{alu}(x)$ – geometric factor of the aluminum sample,
$G_{rock}(x)$ – geometric factor of the sandstone sample,
x – length of the sample,
$\alpha_{alu}(f)$ – frequency-dependent attenuation factor of the aluminum sample,
$\alpha_{rock}(f)$ – frequency-dependent attenuation factor of the sandstone sample,
k_{alu} – wavenumber of the aluminum sample,
k_{rock} – wavenumber of the sandstone sample.

McDonal et al. (1958), Jackson and Anderson (1970) previously showed that in the frequency range 0.1–1 MHz the attenuation factor $\boldsymbol{\alpha}$ is a linear function of frequency which can be written as follows

$$\boldsymbol{\alpha(f) = \gamma f} \tag{33}$$

where γ is a proportionality factor. If the geometry of the aluminum sample and the rock sample are the same, the spectral ratio will be as follows

$$\frac{\boldsymbol{A_{alu}(f)}}{\boldsymbol{A_{rock}(f)}} = \boldsymbol{e^{-(\gamma_{alu}-\gamma_{rock})fx}} \tag{34}$$

Compared to rocks, aluminum is an almost attenuation-free medium ($\gamma_{alu} \approx 0$), therefore

$$\frac{\boldsymbol{A_{alu}(f)}}{\boldsymbol{A_{rock}(f)}} = \boldsymbol{e^{\gamma_{rock}fx}} \tag{35}$$

Thus, by taking the natural logarithm of Equation (35), we can obtain the proportionality factor γ_{rock} of the rock

$$\boldsymbol{\gamma_{rock}} = \frac{\boldsymbol{ln\left(\frac{A_{alu}(f)}{A_{rock}(f)}\right)}}{\boldsymbol{x\,f}} \tag{36}$$

Knowing the γ_{rock} quantity, the Q factor can be determined (Toksöz et al., 1979)

$$\boldsymbol{Q} = \frac{\boldsymbol{\pi}}{\boldsymbol{v\,\gamma_{rock}}} \tag{37}$$

where v is the velocity of the acoustic wave. Neglecting the phase shift and the measurement errors, the logarithm of the spectral ratio calculated as a function of frequency is scattered around the following equalization line

$$\boldsymbol{ln\left(\frac{A_{alu}(f)}{A_{rock}(f)}\right)_{str} = \beta f + \delta} \tag{38}$$

where β – inclination angle of the equalization line,
δ – vertical axis section of the equalization line.

Based on relations (36) and (37), the value of the Q factor is given as

$$\boldsymbol{Q} = \frac{\boldsymbol{\pi x f}}{\boldsymbol{v\,ln\left(\frac{A_{alu}(f)}{A_{rock}(f)}\right)_{str}}} \tag{39}$$

REFERENCES

Birch, F. (1960). The velocity of compression waves in rocks to 10 kilobars. Part 1. *Journal of Geophysics Research,* 65, pp. 1083–1102.

Brace, W. F. and Walsh, J. B. (1964). A fracture criterion for brittle anisotropic rock. *Journal of Geophysics Research,* 69, pp. 3449–3456. https://doi.org/10.1029/JZ069i016p03449

Dobróka, M. and Somogyi-Molnár, J. (2012). The pressure dependence of acoustic velocity and quality factor: new petrophysical models. *Acta Geodaetica et Geophysica Hungarica*, 47, pp. 149–160. https://doi.org/10.1556/AGeod.47.2012.2.4

Dócs, R. and Baracza, M. K., (2022). A new method of pressure drop modelling in sandstone rocks. *Multidisciplinary Studies*, 12, 3, pp. 264–273.

Gyulai, Á., Baracza, M. K. and Tolnai, É. E. (2013): The application of joint inversion in geophysical exploration. *International Journal of Geoscience*, 4, pp. 283–299

Jackson, D. D. and Anderson, D. L. (1970). Physical mechanisms of seismic wave attenuation. *Rev. Geophys. Space Phys*., 8, pp. 1–63.

Ji, S., Wang, Q., Marcotte, D., Salisbury, M.H. and Xu, Z. (2007). P wave velocities, anisotropy and hysteresis in ultrahigh-pressure metamorphic rocks as a function of confining pressure. *Journal of Geophysics Research*, 112, B09204. https://doi.org/10.1029/2006JB004867

McDonal, F. J., Angona, F. A., Mills, R. L., Sengbush, R. L., Van Nostrand, R. G. and White, J. E. (1958). Attenuation of shear and compressional waves in Pierre shale. *Geophysics*, 23, pp. 421–439.

Menke, W. (1984), *Geophysical Data Analysis – Discrete Inverse Theory*, London, Academic Press.

Nagy, Zs., Baracza, M. K. and Szabó, N. P., (2019a). Integrated Pore Pressure Prediction with 3D Basin Modeling. *Second EAGE Workshop on Pore Pressure Prediction*, pp. 1–5., 19–21 May 2019, Amsterdam, Netherlands.

Nagy, Zs., Baracza, M. K. and Szabó, N. P., (2019b). Pore Pressure Prediction In: Pannonian Hydrocarbon Reservoir Systems Using An Integrated Interpretation Approach. *Geosciences and Engineering*, 7, 12, pp. 105–115.

Somogyi Molnár, J., Kiss, A. and Dobróka, M. (2015). Petrophysical models to describe the pressure dependence of acoustic wave propagation characteristics. *Acta Geodaetica et Geophysica*, https://doi.org/10.1007/s40328-014-0074-4.

Stierman, D. J., Healy, J. H. and Kovach, R. L. (1979), Pressure-induced velocity gradient: An alternative to a Pg refractor in the Gabilan Range, central California, *Bulletin of the Seismological Society of America*, 69, pp. 397–415. https://doi.org/10.1785/BSSA0690020397

Toksöz, M. N., Johnston, D. H. and Timur, A. (1979). Attenuation of seismic waves in dry and saturated rocks. *Geophysics*, 44 (4), pp. 681–690.

Wang, Q., Ji, S.C., Salisbury, M.H., Pan, M.B., Xia, B. and Xu, Z.Q. (2005). Pressure dependence and anisotropy of Pwave velocities in ultrahigh-pressure metamorphic rocks from the Dabie-Sulu orogenic belt (China): Implications for seismic properties of subducted slabs and origin of mantle reflections. *Tectonophys*, 398, pp. 67–99. https://doi.org/10.1016/j.tecto.2004.12.001

Wepfer, W.W. and Christensen, N.I. (1991). A seismic velocity-confining pressure relation, with applications. *International Journal of Rock Mechanics and Mining Sciences & Geomechanics*, 28, pp. 451–456. https://doi.org/10.1016/0148-9062(91)90083-X

Yu, G., Vozoff, K., and Durney, D. W. (1993). The influence of confining pressure and water saturation on dynamic elastic properties of some Permian coals. *Geophysics*, 58 (1), pp. 30–38.

Geosciences and Engineering, Vol. 12, No.1 (2024), pp. 20–29.
https://doi.org/10.33030/geosciences.2024.01.002

INVESTIGATION OF HEAVY METALS DESORPTION ENHANCEMENT PROCEDURES IN LOW-PERMEABILITY CONTAMINATED SOILS

TAMÁS BACSÓ[1]*, MÁRTON TÓTH[2]
[1]**Institute of Environmental Management, University of Miskolc;*
tamas.bacso@outlook.com
[2]*Institute of Environmental Management, University of Miskolc;*
hgtoth@uni-miskolc.hu
[1]*https://orcid.org/0000-0003-1120-443*
[2]*https://orcid.org/0000-0002-8262-2748*

Abstract: A significant amount of hydrocarbon contaminants (therefore heavy metal components) has remained in the soil due to careless industrial activities. Effective remediation is difficult, especially in low-permeability soils because it is extremely difficult to get desorption. A lot of research has been conducted on extreme soil acidification, batching of oxidants, air-fluid injection and electrokinetic treatment, there were successful but due to the risk from extreme loads, these methods can only be used solely in controlled ex-situ environments. This paper investigates an eco-friendly in situ treatment with carbamide peroxide in low-permeability silty clay. After several repetitions, the result of tests proved Cu component was fully adsorbed on clayey-silt among applied concentration and circumstances which applied, while two other components were partially adsorbed. Moreover, the experiments carried out to enhancement of desorption proved to be successful for Cu, Zn and Mn with carbamide peroxide.

Keywords: *low-permeability, adsorption, enhancement of desorption, remediation*

1. INTRODUCTION

Based on evidence from the past years, it can be concluded that environmental remediation of hydrocarbon and heavy metal contamination in low-permeability soils is not effective. One of the reasons is adsorption, in which continuous contaminant supply is ensured through rediffusion to groundwater. The purpose of our research is to determine that adsorbed contaminants can be get solution with this increase the degree of desorption. Soil contaminants can fall into the environment from different anthropogenic activities (oil industry, chemical industry, heavy industry). Moreover, near hydrocarbon compounds, heavy metals can be considered the other main contaminant group, which is one of today's remediation problems.

2. MATERIALS AND METHODS

2.1. Studied heavy metals

Some refined petroleum derivatives like fuels contain potentially toxic elements and heavy metals *(Table 1)*. Akpoveta and Osakwe (2014) demonstrated that fuels

contained several heavy metals as detailed below. This paper investigates the process of Zn, Mn, and Cu heavy metal adsorption in low-permeability clay then introduces measured results aimed at the enhancement of desorption.

Table 1

Heavy metals content of fuel

Fuel type	Zn (mg/l)	Cu (mg/l)	Cr (mg/l)	Pb (mg/l)	Cd (mg/l)
benzene	1.43	1.74	0.54	0.24	1.68
kerosene	2.63	1.98	0.33	0.41	1.33
diesel oil	2.87	1.77	0.86	1.01	1.50

2.2. Adsorption

The reversible sorption of contaminants on the surface of soil is called adsorption. During adsorption, several interfacial equilibrium processes take place simultaneously at the phase boundary resulting in material accumulation. Atoms and molecules that are located on the surface of the soil just meet their particles on one side, while on the opposite side, they encounter contaminant phase particles. The balance of adsorbed and desorbed material quantities is described by the following equation

$$dV\frac{\partial C}{\partial t} * \Theta = -\rho_b * dV\frac{\partial C_c}{\partial t} \tag{1}$$

where C is pore fluid concentration (mg/l), C_c is contaminant concentration in soil, ρ_b is soil density, Θ is water content, V is full volume. If chemical equilibrium has been established the concentration of the adsorbed component can be calculated using the following relationship

$$C_C = K_d * C \tag{2}$$

where K_d is the distribution coefficient (L/g).

Equation (2) shows the relationship between the concentration of pore fluid and the contaminant, which is determined by a sorption isotherm. In addition, *Equation (2)* also depends significantly on temperature, thus to rule out temperature dependence, the relationship between the concentration of the pore fluid and the adsorbent is taken at a constant temperature.

Adsorption from the solution is influenced by the quantitative ratio of the adsorbent and adsorbate. According to Kroeker's equation (Kroeker, 1892), in a solution of known volume and concentration, the specific adsorbed amount decreases as the mass of the adsorbent increases. In case of contact between the solution and solid adsorbent, after a sufficiently long time, the adsorption equilibrium is established. The time required to reach equilibrium depends on the quality of the adsorbent and the adsorbate as well as the structure of the adsorbent. After equilibrium has been established, the adsorbent can be separated from the solution then equilibrium concentration can be measured using a carefully selected

method. At constant temperature, this equilibrium can be described by adsorption isotherms. The obtained results determine the points of the sorption isotherm whose points we can fit into curves to get the Freundlich and Langmuir isotherms, which are most often used.

2.3. Parameters affecting adsorption

Adsorption is controlled by several influencing factors. The effect of ionic strength for cation adsorbing is multifaceted. According to the research of Weng and Huang (2004), the cation binding on a negatively charged surface decreases with the increase in the ionic strength of the solution, which reduces the cation activity of the adsorbent. A higher temperature range increases the proportion of particles that have sufficient energy to overcome the activation energy barrier necessary for sorption processes; furthermore, the mobility of ions also increases with increasing temperature. According to Fick's first law, diffusion is proportional to the concentration gradient of the sorption system which is an extremely important factor, since adsorption is in most cases a diffusion-controlled process. It follows from the above that the number of cations fixed by the soil increases at higher temperatures.

The solubility of pollutant components can be influenced by the redox potential significantly. In highly reductive (–100 mV>) conditions, the mobility of individual cations can be decreased. Furthermore, time as an adsorption factor also affects the amount of bound adsorbent significantly.

The chemical reaction is significantly influenced by soil pH. In an acidic environment, the degree of cation adsorption decreases while the solute concentration of toxic heavy metals and/or organic hydrocarbon contaminants can increase. Furthermore, there are some other parameters (e.g., CEC, SOM) affecting the sorption processes, but these are not detailed in this article.

2.4. Analytical solution for 1D column model

The spread of water-soluble contaminants is determined by two main processes; advection which is physically or chemically dissolved substances mass flow in pores. The other one is dispersion, which is the pollutant means its spatial dispersion. Ogata and Banks solve the ADE (advection-dispersion, diffusion) equation given below

$$D * \frac{\partial^2 \mathrm{C}}{\partial \mathrm{x}^2} - v \frac{\partial \mathrm{C}}{\partial \mathrm{x}} = R * \frac{\partial \mathrm{C}}{\partial \mathrm{t}} \tag{3}$$

with the following boundary and initial conditions: t = 0–150 minutes and C = C_0 (x = 0) then t > 150 minutes, x = 0, C = 0. Here *C* is the concentration (ML^{-3}), *x* is the distance (L), *R* is the retardation factor, *D* is the effective dispersion/diffusion (L^2T^{-1}), *v* is the flow velocity (LT^{-1}) and C_0 is the initial concentration (ML^{-3}). For ADE equation the Ogata-Banks' analytical solution is

$$C = C_0 * \frac{1}{2} erfc\left(\frac{R*x-v*t}{2\sqrt{D*R*t}}\right) + \frac{1}{2} e^{\frac{v*x}{D}} * erfc\left(\frac{R*x+v*t}{2\sqrt{D*R*t}}\right) \quad (4)$$

2.4.1. Advection

The advective contaminant-flux equation is the product of the average flow velocity and the concentration given in *Equations (5)–(7)*

$$F_x = \frac{dM_x}{dy\,dz\,dt} = v_x * C \quad (5)$$

$$F_y = \frac{dM_y}{dx\,dz\,dt} = v_y * C \quad (6)$$

$$F_z = \frac{dM_z}{dy\,dx\,dt} = v_z * C \quad (7)$$

where M is the chemical amount of the contaminant, n_e is effective porosity and velocity *v* is

$$v = -\frac{K}{n_e}\frac{dh}{dx} \quad (8)$$

2.4.2. Diffusion

The mass flow resulting from spatial chemical potential differences is called diffusion (Fick's first law). Diffusion resulting from concentration differences is called ordinary diffusion. Diffusion describes the spread of particles through random motion from regions of higher concentration to regions of lower concentration. As Fick's I. law gives the diffusive flux

$$F_D = D_{eff} * \frac{dC}{dx} \quad (9)$$

The diffusion coefficient depends on the materials, temperature, electrical fields.

2.4.3. Hydrodynamic (or mechanical) dispersion

Hydrodynamic (or mechanical) dispersion is caused by local micro-changes in the size and direction of the flow velocity within the porous medium. Dispersion causes transport (or spreading) of the solute plume ($D = D_{eff} + D_{mech}$). Dispersion reflects the fact that not everything in the porous medium travels at the average water flow speed. Some path is faster, some slower, some longer, some shorter. This results in

a net spreading of the solute plume that looks very much like a diffusive behavior. From Ogata–Banks equation one can obtain

$$D * \frac{\partial^2 C}{\partial x^2} \tag{10}$$

2.4.4. Retardation

When solutes flow through a porous medium they can interact with the solid phase. They can sorb and desorb. The net result is a process called retardation that effective slows the transport of a solute through a porous medium. The value of *R* depends on the solute, water chemistry and geochemical make-up of the porous medium. From a mathematical perspective it can be thought of as a rescaling in time.

2.5. Sorption tests

Adequate model material was acquired from the settlement of Aszód, Hungary. These soil samples were investigated by soil-mechanics tests and laser scattering particle size analysis, as pale-brown clayey-silt.

2.5.1. Dynamic sorption – Column test

The experiment was performed with Cu, Zn and Mn ions that can simulate competitive sorption and to evaluate and investigate these heavy metals retention and transport under saturated flow conditions. The pH value is contaminant solution was set to 7.7 an experiment was made on 20 ^{o}C temperature. The steady-state flow was assured by an HPLC pump. The cylindrical column was made of steel, 250 mm in length and 10 mm in inner diameter and was closed by two steel caps. The column was filled with a mixture of clayey-silt (10%) and quartz sand (90%). The mixing was needed because permeability of clayey silt is too low, thus that would have resulted that the fluxation (through column) would have taken too much time. The stock-solution was made of 1000 ml distilled water wherein dissolved 0.616 g of Mn, 0.786 gr of Cu and 0.879 gr of Zn. Immediately the system was compiled, a solution of heavy metals was inject-ed upwards into the system at a constant flow rate (1 cm^3/s) until 150 minutes. Samples of 5 ml were collected from the effluent with an auto-sampler at every 5 minutes time interval, its resulted 30 pieces of samples at the first section of test. Second interval was holding 50 minutes which resulted 10 samples. In interval the column-system was leached with distilled water to can be isolated the effect of treatment which is on third interval. At the third interval applied carbamide-peroxide (0.186 g/250 ml distilled water) as an oxidizer can observe its desorption affect. The outlet samples Zn, Mn and Cu concentrations were measured using Agilent Spectroscopy (MP-AES).

3. RESULTS AND DISCUSSION

Several quantitative methods are suggested to be used to analyze adsorbates. During this research the Agilent MP-AES Spectrometer was used to determine the concentration of Zn, Mn and Cu components used in column experiment. The Agilent Spectroscopy (MP-AES) is an analytical technique designed with a higher sensitivity that detects sub ppb levels and runs on air instead of combustible gases. The Agilent MP Expert software is used to automatically optimize the viewing position and the nebulization pressure for each wavelength selected to maximize sensitivity. We performed a total of three series of measurements with the same parameters, so that we can adequately support the obtained results. Unfortunately, the 2nd measurement was not successful due to other reasons, thus this measurement is not presented in this paper, we only deal with the results of the 1st and 3rd measurements.

The breakthrough curves are presented in *Figures 1–2*, where the performance of the column system can be estimated. On the score of results, one can see the saturation concentrations. Moreover, the analytical solution suggested by Ogata and Banks was used to solve the advection-dispersion equation for Zn-Mn-Cu competitive adsorption. By applying the inverse modelling we can determine the retardation factor R and diffusion value.

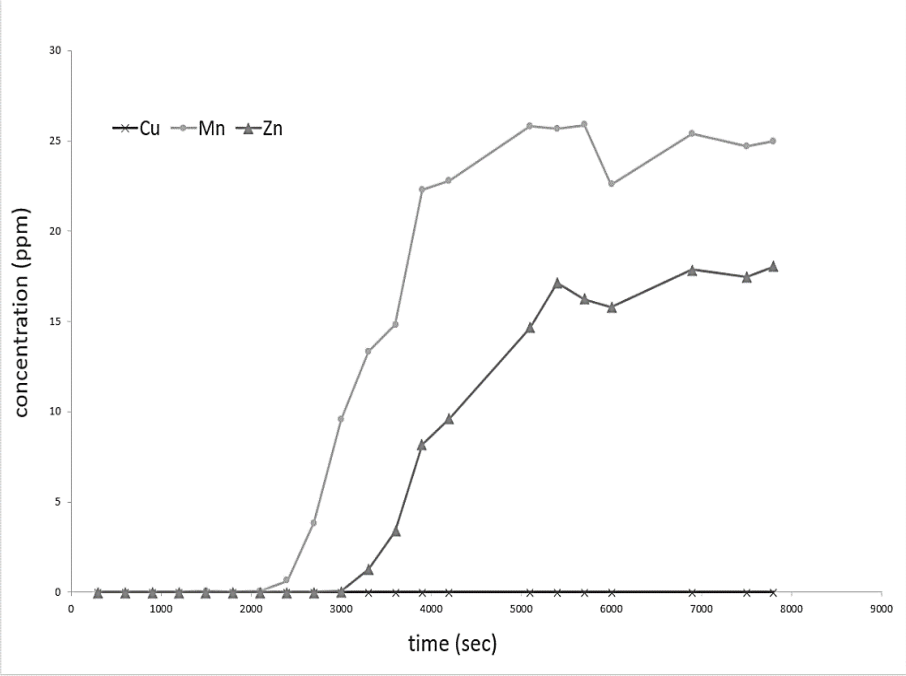

Figure 1
Breakthrough curve of the 1st competitive adsorption-test

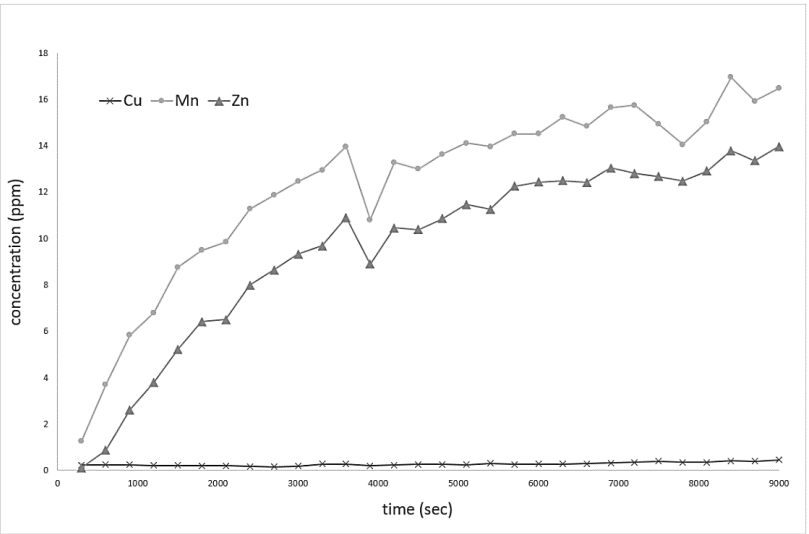

Figure 2
Breakthrough curve of the 3rd competitive adsorption-test

Finally, we can see the curves had a similar breakthrough time, but the third measurement series has a longer breakthrough and saturation time. The input data of the model are shown in *Table 2*.

Table 2
Initial values of the input parameters

Model input data	Value
v (cm/s)	0,019
x (cm)	25,0
A (cm²)	0,786

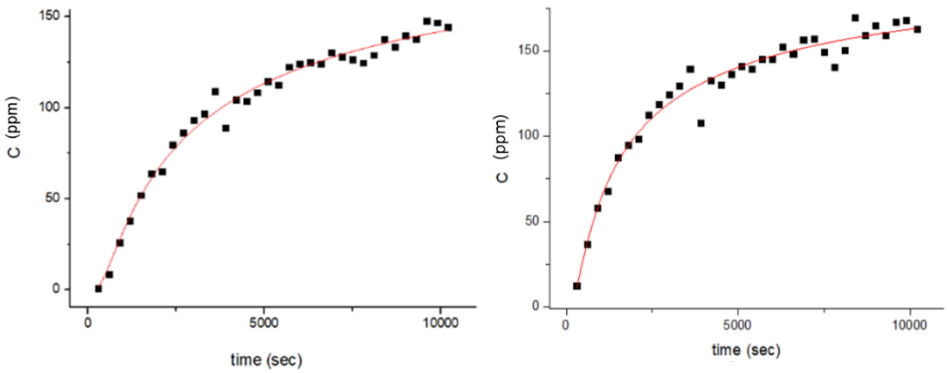

Figure 3
Zn (upper) and Mn components Ogata–Banks fitting curves

The plots given in *Figure 3* show a good agreement with the column experimental data in the case of Cu and Zn components ($R^2 > 0.97$). In virtue of results Mn has the biggest adsorption factor on clayey silt. Furthermore, uninterpretable result was got for Cu, which means that it was fully adsorbed by clayey silt. Finally gotten dispersity values are suitable.

Table 3

Obtained results from 3rd column test

Metal	Estimated			Measured		
	D (cm^2/s)	**R (–)**	**R^2 (–)**	**v (cm/s)**	**x (cm)**	**C_0 (ppm)**
Zn – 3rd	2.24091	15.38587	0.98595	0.019	25	200
Mn – 3rd	2.0261	7.53195	0.97024	0.019	25	200
Cu – 3rd	–	–	–	0.019	25	200

During column tests we can observe that the adsorption of the manganese and zinc components already separated each other at first, moreover we can see that the retardation factor of Manganese is twice of Zinc. Finally, we increased desorption by using oxidizer aggregate, is carbamide peroxide. It is a soft-oxidizing agent of which 10 gr was dissolved in 200 ml distilled water as "treatment solution". During the desorption test, we can observe when the treatment solution washed all column the effluent concentration was being increased in a little period (20 minutes) then rising stopped then followed by a slight decreasing phase (treatment session) *(Figures 4–5)*.

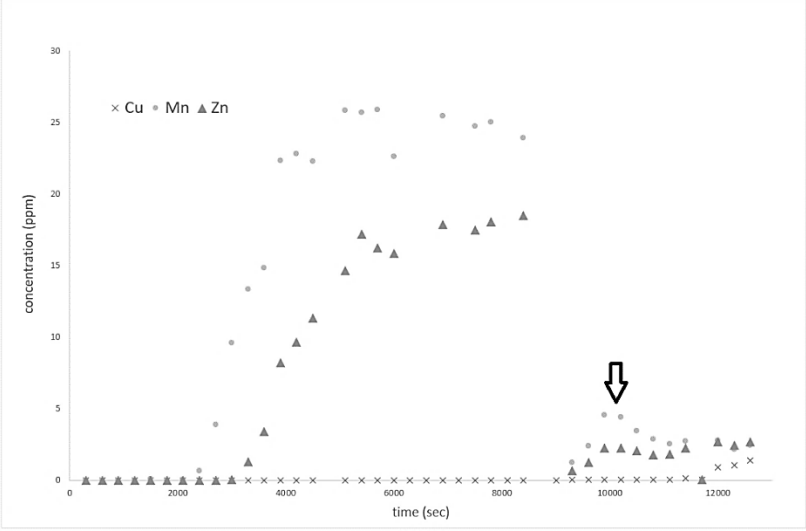

Figure 4

Concentration changes as a result of carbamide-peroxid treatment (1th)

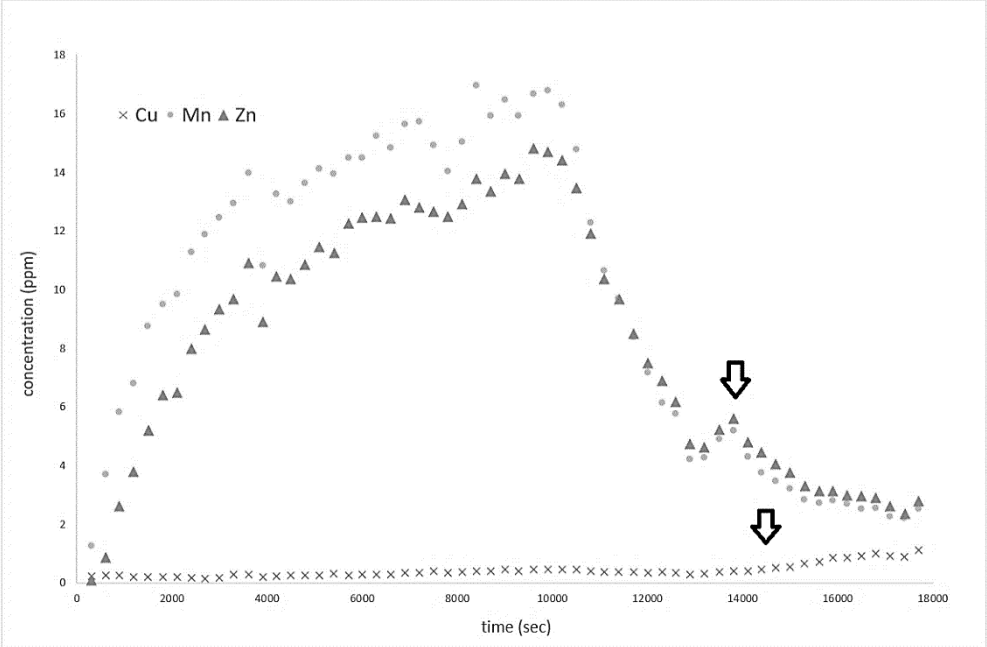

Figure 5
Concentration changes as a result of carbamide-peroxid treatment (3rd)

4. CONCLUSIONS

In virtue of investigations Cu component was fully adsorbed on clayey silt among applied concentration and circumstances which applied. The experiments carried out to enhancement of desorption proved to be successful for Cu, Zn and Mn, which have not yet been proven with the present results, but it seemed to be encouraging. We believe that the treatment with carbamide-peroxid has a measurable effect, which can be effective in increasing desorption at a higher concentration and by changing other conditions. We are continuing our research using other possible oxidizing agents and using another potential treatment (e.g., temperature, aggregates, pH, electricity).

REFERENCES

Akpoveta, Osakwe (2014). Determination of Heavy Metal contents in refined petroleum products. *IOSR Journal of Applied Chemistry*, Vol. 7, Issue 6, Ver. I. (Jun. 2014), pp. 1–2.

Borjini, M. (2021). *Investigation of zinc adsorption by red mud under static and dynamic conditions.* Thesis. University of Miskolc, Faculty of Earth Science and Engineering, Institute of Environmental Management.

Filep Gy., Kovács B., Lakatos J., Madarász T., Szabó I. (2002). *Szennyezett területek kármentesítése.* Miskolci Egyetem.

Giles, Macewans, Nakhwaa, Smith (1960). Studies in Adsorption – part XI. A System of Classification of Solution Adsorption Isotherms, and its Use in Diagnosis of Adsorption Mechanisms and in Measurement of Specific Surface Areas of Solids. *Journal of the Chemical Society*, pp. 3973–3993. https://doi.org/10.1039/JR9600003973

Gruiz K. (2009). *Talajremediáció. A természetes szennyezőanyag-csökkenési folyamatok felhasználására és intenzifikálására alkalmas technológiák áttekintése.* Szakirodalmi jegyzet. https://enfo.hu/

Kovács B., Szanyi J. (2004). *Hidrodinamikai és transzportmodellezés I.* Első kiadás. Miskolc, Miskolci Egyetem.

Könignné P. A. (2014). *Nehézfém adszorpció jellemzése különböző bioszorbenseken*. Doktori (PhD-) értekezés. Pécs, Pécsi Tudományegyetem, Kémia Doktori Iskola.

Lengyel Zs. (2020). *Klór-acetanilid típusú herbicidek adszorpciójának vizsgálata talajokon és talajalkotókon*. PhD-értekezés. Veszprém, Veszprémi Egyetem, Környezetmérnöki és Kémiai Technológia Tanszék.

Ogata, A., Banks, R. B. (1961). *A solution of the differential equation of longitudinal dispersion in porous media.* Geological Survey professional paper 411, Washington, United States Government Printing Office.

Geosciences and Engineering, Vol. 12, No. 1 (2024), pp. 30–56.
https://doi.org/10.33030/geosciences.2024.01.003

INVESTIGATION OF GROUNDWATER POTENTIAL UTILIZING GEOSPATIAL TECHNIQUES IN OWERRI, NIGERIA

OKOLI EMEKA AUSTIN[1], AGBASI OKECHUKWU EBUKA[*2], AKAOLISA CASMIR CHUKWUEMEKA ZANDERS[1], IKORO DIUGO OKEREKE[1], UBECHU BRIDGET ODOCHI[1], IFEANYICHUKWU KENECHUKWU AGBONMA[3], ONYEAWUNA UZOCHI BRIGHT[1]

[1]*Department of Geology, Federal University of Technology, Owerri, Nigeria.*
[2*]*Okan Geoservices Nigeria Limited, Nigeria.*
[3]*Department of Geological Sciences, Nnamdi Azikiwe University Awka, Nigeria*
[1]*https://orcid.org/0000-0003-4777-1980 (emeka.okoli@futo.edu.ng)*
[2]*https://orcid.org/0000-0001-5649-0107 (agbasi.okechukwu@gmail.com)*
[3]*https://orcid.org/0000-0001-8441-948X (casakaolisa@futo.edu.ng)*
[4]*https://orcid.org/0000-0003-3389-447X (diugo.ikoro@futo.edu.ng)*
[5]*https://orcid.org/0000-0002-4358-5163 (bridgetubechu@gmail.com)*
[6]*https://orcid.org/0000-0001-9593-6028 (ifeanyichukwu@unizik.edu.ng)*
[7]*https://orcid.org/0000-0003-0462-7698 (uzochibright@yahoo.com)*

Abstract: This study used geospatial approaches to examine the potential of groundwater within the study area. Analytic Hierarchy Process (AHP) method was used combining various parameters including Rainfall (39.5%), Geology (23.5%), Slope (12.5%), Drainage Density (8.0%), LULC (6.1%), Lineament Density (5.4%), and Soil Type (5.0%) for an integrated geospatial analysis to assess the potential for groundwater in the study area. Pairwise comparisons were used to assess the relative importance of each parameter. AHP determined these weights after the pairwise matrices were completed. These weights show the relative importance of the themes when assessing the study area's potential for applications such as land-use planning or natural resource management. The AHP technique allows for the systematic evaluation and ranking of alternatives based on a variety of criteria. A groundwater potential index (GPI) map was created by combining all of these thematic maps and classifying the research area into three zones: poor (0.001%), fair (41.092%) good (58.686%), and excellent (0.261%) groundwater potential areas. The findings showed significant groundwater potential in regions with higher lineament density, low to average slope, and suitable land use and land cover. The weighted overlay strategy was reliable, according to the consistency ratio (CR) analysis of 0.043884. This work shows the importance of an integrated RS and GIS analysis for determining groundwater potential. The results help identify locations with higher groundwater potential and enable sustainable use of groundwater resources.

Keywords: *Geospatial Modeling, Groundwater Exploration, Hydrogeology, Spatial Analysis, Water Resources Management*

1. INTRODUCTION

It is impossible to exaggerate the significance of water as a resource for life on Earth. Yisa and Jimoh's (2010) research indicates that the world's population increases and

industrialization are to blame for the rising demand for freshwater. Nigeria, which has recently witnessed a tremendous pace of industrialization and population increase, is no exception to this trend. As a result, groundwater has gained popularity as a source of water due to its broad occurrence and availability as well as the fact that it possesses high-quality components that make it suitable for drinking (Agbasi et al., 2019). According to Sander (2007), many Nigerians are now obliged to drink well water due to a lack of freshwater supplies. Over half of the world's population relies on groundwater for sustenance, hence this tendency is not specific to Nigeria. Since groundwater is one of the cleanest types of water found in nature, it is a perfect source for supplying the total water requirement in rural and semi-rural areas (Abdulrazzaq et al., 2020). Particularly in rural areas, it is regarded as the main supply of water for human activities, including drinking (Fasunwon, 2008).

Exploring and using alternative water sources, such as groundwater, is crucial given the rising demand for freshwater (Agbasi et al., 2019). Communities lacking access to sufficient quantities of fresh water can benefit from the stable and safe drinking water that can be obtained from groundwater (Aboyeji, 2013). Groundwater is an important component of the earth's water cycle, which refers to the natural circulation of water in the ecosystem (Opara et al., 2020; Akaolisa et al., 2022a). Given that it accounts for around 30% of the world's freshwater supplies, groundwater is regarded as one of the most important sources of freshwater on Earth (Akaolisa et al., 2022b). It supports agriculture, manufacturing, and a variety of other human endeavours and is a very important resource for economic growth and human well-being.

Despite its significance, groundwater is in danger because of several human activities that can contaminate it. Some of these activities include the excessive use of fertilizers and pesticides in agriculture, the disposal of chemical waste in water bodies from industrial activities, and other forms of pollution (Akaolisa et al., 2022c) Groundwater quality is deteriorating rapidly, posing a significant risk to human health and the environment. Accurately assessing the groundwater resources and the characteristics of the aquifers is critical for addressing various hydrogeological and hydrological problems in the study area (Mogaji, 2016; Mogaji et al., 2021). This geospatial approach provides a comprehensive assessment of the aquifer's vulnerability to contamination and enables the implementation of appropriate management strategies to ensure its long-term sustainability. Groundwater Potential (GWP) mapping assesses aquifer vulnerability by identifying places with significant water reserves, understanding hydrogeological conditions, mapping recharge zones, and monitoring land use consequences.

Contamination of groundwater occurs when there is an adverse change in its quality, rendering it unsuitable for human consumption and other environmental needs (Kumar et al., 2015; Akinlalu et al., 2021). Although groundwater is naturally attenuated, it is nevertheless susceptible to contamination, especially in regions where pollution-producing human activity is prevalent (Akinlalu et al., 2021). Unfortunately, this vital resource has not gotten enough care and protection, which has resulted in numerous instances of quality degradation. Therefore, it is crucial to put policies into place that aim to avoid groundwater contamination, such as limiting the use of pesticides in agriculture and reining in industrial activities that produce pollutants.

Groundwater found in holes and fractures of geological formations is protected from evaporation and contamination, making it appropriate for a variety of uses (Agidi et al., 2022). Hydro-geophysical methods like electrical resistivity, magnetics, gravity, electromagnetics, seismic, and remote sensing are used to determine groundwater depth. Gravity and magnetics are good for mapping large-scale features, while seismic methods are more accurate for locating subterranean aquifers and fractured rock structures (Agbasi and Etuk, 2016). In this study, groundwater potential in several areas of Owerri, Southeast Nigeria, was examined using geospatial approaches.

Owerri, a city in the southeast of Nigeria, is one such region that needs in-depth examination. Imo State's capital, Owerri, is a rapidly expanding urban area with a population of more than a million. Due to the city's expanding population and burgeoning economic activity, groundwater resources are essential to supplying the city with the water it requires. The purpose of this study is to use geospatial approaches to examine the potential for groundwater in specific areas in Owerri, Southeast Nigeria.

2. STUDY AREA

The Owerri study area is situated in Imo State, one of the states in Nigeria. Imo State is headquartered in Owerri, a city in the southeast of the nation. According to *Figure 1*, the city is located between latitudes 5°28'N and 5°33'N and longitudes 7°00'E and 7°07'E. Two important rivers border Owerri on either side. The Otamiri River forms its eastern border, and the Nworie River forms its western border. These rivers influence the local hydrology by serving as a supply of water for diverse uses and sculpting the terrain (Ibe and Sowa, 2002).

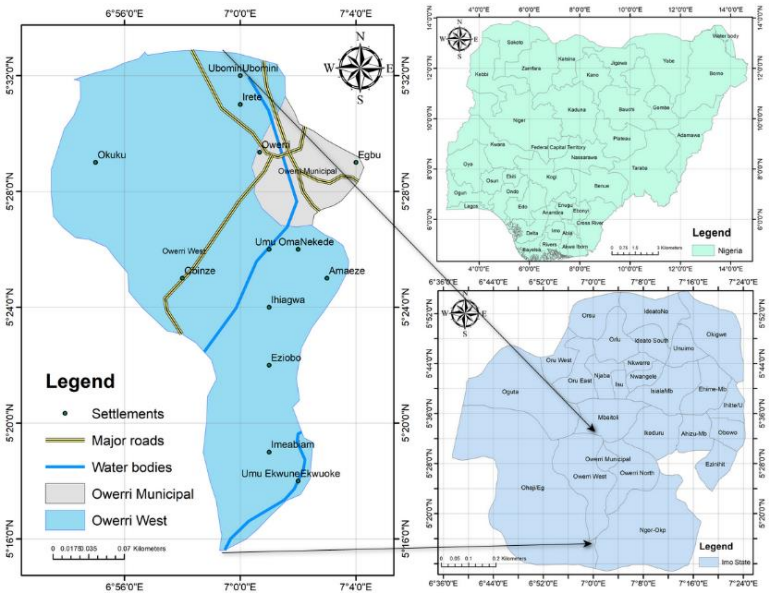

Figure 1

Map of the study area and Imo State, Nigeria

The sedimentary rocks of the Benue Trough, which have a considerable impact on the geology and geography of the area, are intricately linked to the geology of Owerri, Imo State as shown in *Figure 2*. A significant geological feature in Nigeria is the Benue Trough, which is a component of the wider West African Rift System, a tectonic structure that extends through numerous West African nations (Ibe and Sowa, 2002).

A linear depression with a length of about 1,000 kilometres and a maximum width of 150 kilometres, the Benue Trough. It crosses several Nigerian states, notably Imo State, where Owerri is situated. This geological formation resulted from tectonic activities connected to continental rifting during the Early Cretaceous period, from 130 to 100 million years ago (Ibe and Sowa, 2002). Sedimentary rocks predominate in the geological composition of the Benue Trough. The ecosystems in which these rocks were deposited throughout millions of years included marine, lacustrine (lake), and fluvial (river) settings.

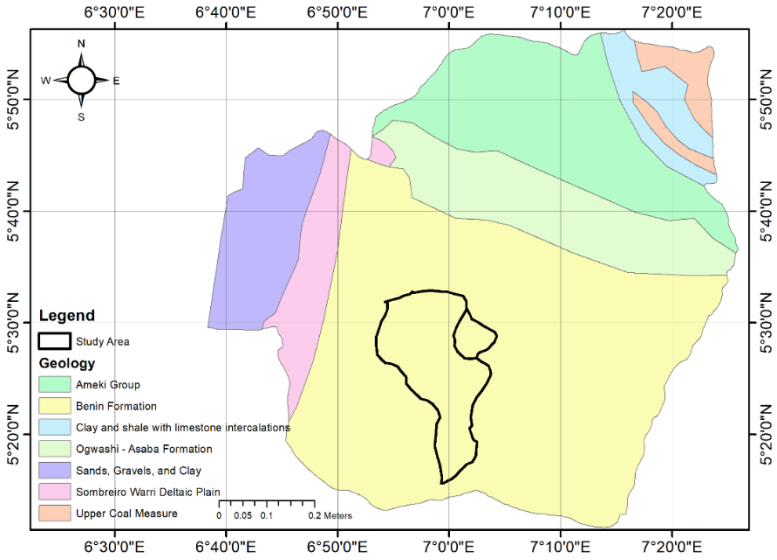

Figure 2

Geology map of the study area and Imo State

The tectonic forces affecting the area are what led to the development of these structures. While folds are curved or bending rock layers brought about by compression, faults are cracks in the rocks along which movement has taken place. The topography and the distribution of rock units in the region have been impacted by these structural elements, resulting in elevational variations and the production of geological features like hills and valleys (Ibe and Sowa, 2002). Understanding the geology of Owerri offers important insights into the region's geological past and natural resources. It provides hints about the potential for mineral deposits and other valuable resources as well as aids geologists in their understanding of the processes that produced the landscape over millions of years (Ibe and Sowa, 2002).

3. METHODOLOGY

3.1. Data Sources in Groundwater Potential Assessment

The geospatial analysis in this study made use of the Digital Elevation Model (DEM) and Satellite Shuttle Radar Topography Mission (SRTM) data. The global reference system-2 served as the reference framework as the satellite took photographs of the Earth over a 16-day repetition cycle (Aladeboyeje et al., 2021). The scene's covering area was roughly 170 km in the North-South direction and 183 km in the East-West direction. ArcGIS 10.8 software was used to build and integrate numerous thematic layers required for finding pertinent groundwater potential areas and carrying out groundwater research.

3.2. Materials

Different remote sensing platforms can give DEM data, depending on the subject. This study used aerial LiDAR to acquire DEM data. LiDAR laser pulses return to the sensor after hitting the ground. Using the laser pulse's return time, ground distance is calculated millions of times to create a dense topographical point cloud (Sharma et al., 2010).

Table 1

Data Sources and Resolutions for Environmental Parameters in the Study Area

Parameter	Data Source	Resolution
Digital Elevation Model (DEM)	Aerial LiDAR	Vertical: 5 cm, Horizontal: 1 m
Lineament Maps	ALOSPALSAR	Automated feature extraction
Drainage Maps	ALOSPALSAR	Automated water flow tracking
Slope Maps	ALOSPALSAR	Calculated gradient
Land Use/Land Cover	European Space Agency's Sentinel-2A Imagery	10 meters
Soil Type Maps	World Soil Type Maps (FAO)	Global coverage
Rainfall Data	Nigerian Meteorological Records	Nationwide network
Geological Data	Nigerian Geological Survey Agency	Variable

DEM data collecting requires topography-accurate sensors (Bangen et al., 2014; Gillan et al., 2017). This study LiDAR sensor records elevation data with 5 cm vertical and 1 m horizontal resolution. DEM data authenticity is essential for remote sensing and GIS map and analysis accuracy (Gillan et al., 2017; Kessar et al., 2021). DEM data is collected for remote sensing and GIS utilizing contemporary sensors and software algorithms to accurately assess topographic data. The custom program reduces noise and

artefacts in raw LiDAR data to reconstruct ground surface elevation. Raster DEMs display landscape elevation as a grid from point clouds (George et al. 2022).

The lineament, drainage, and slope maps in this study were produced using the DEM data (Aladeboyee et al., 2021; George et al., 2022; Adewumi et al., 2023). By identifying linear features based on details like their length and orientation, automated feature extraction methods were used to extract the lineament and lineament density data from the DEM data. Using algorithms that track water flow throughout the landscape and determine the length and density of the stream network, the drainage and drainage density maps were created using the DEM data (Dinagarapandi et al., 2020; George et al., 2022). By figuring out the gradient of the landscape at each site, the slope maps were created using the DEM data. In this study, the lineament, drainage, and slope maps were created using the DEM data that was obtained by aerial LiDAR.

Maps of land use and land cover provide details on the location and extent of various land use and land cover types in a certain area. The European Space Agency's (ESA) Sentinel-2A imagery was used in this study to create the land use/land cover map. With a spatial resolution of 10 meters, Sentinel-2A is a satellite mission that provides high-resolution optical pictures of the Earth's surface (Adewumi et al., 2023). The satellite is equipped with a multispectral imaging sensor that can take pictures in 13 different spectral bands, from the visible to the infrared spectrum (Adewumi et al., 2023).

The physical and chemical characteristics of the soils in a specific location, such as their texture, pH, level of organic matter, and availability of nutrients, are described by soil type maps. The data for the soil type map in this study was taken from a map of soil types around the world (Adewumi et al., 2023). Global coverage of soil types is provided through world soil type maps created by international organizations like the Food and Agriculture Organization (FAO) of the United Nations, which combine field data, remote sensing, and modelling.

Rainfall is a significant environmental component that has an impact on the climate, hydrology, and many other parts of the Earth's system. Data on rainfall were gathered for this study from Nigerian meteorological records. The data on rainfall was gathered from a nationwide network of meteorological stations that track weather-related variables like precipitation, temperature, humidity, and wind speed (Adewumi et al., 2023). The regional and temporal variability of rainfall was evaluated using the rainfall data.

The distribution and properties of rocks, minerals, and geological structures in the research region are described by the geological data collected from the Nigerian Geological Survey Agency. The data includes geological maps, reports, and databases that contain information about the lithology, stratigraphy, and tectonic history of the area. The data also provides information about mineral resources and potential hazards such as landslides, earthquakes, and volcanic eruptions.

3.3. GIS/RS Data Preprocessing and Preparation of Thematic Layers for Groundwater Potential Assessment

Based on the data that was available at the research location, a number of thematic layers were developed to estimate groundwater potential zones. For this, seven effective parameters—geology, rainfall, slope, land use/cover, soil type, drainage, and lineament density—were chosen and used.

Groundwater occurrence was also found to be influenced by land use and cover (Roy et al., 2022). Different forms of land cover can either help retain water by reducing runoff or increase evapotranspiration, which can lower groundwater levels. The study region included several forms of land cover, such as vegetation, built-up areas, arid land, agricultural areas, and water bodies. The early creation of a summary of land use and land cover relied on visual interpretation. Then, utilizing the proper band combinations, supervised classification using the maximum likelihood classifier was carried out (George et al., 2022). The generated land-use map was then divided into categories to identify possible groundwater regions.

Groundwater presence, as well as the size and distribution of aquifers and aquitards in a certain location, are greatly influenced by the composition and properties of geological strata, including lithology, stratigraphy, and structure (Ibuot et al., 2022). Soil type has a direct impact on the aquifer rocks' porosity and permeability. The soil type map for the study area was digitally created from an Imo state geology map. Given the importance of soil type in determining groundwater potential, the map was further categorized to prepare for groundwater mapping.

RS data can show drainage patterns, which are crucial indicators of the groundwater potential. The drainage pattern, texture, and density of a region are significantly influenced by the underlying lithology (George et al., 2022). While moderate drainage density denotes intermediate groundwater potential, high drainage density indicates an area that is averse to the occurrence of groundwater. On the other hand, locations with little or no drainage density suggest ideal circumstances for groundwater presence. A drainage density map can be produced by the drainage pattern, which can be deduced from the DEM (Adewumi et al., 2023). The generated map can then be categorized to identify regions with potential for groundwater for future examination. The drainage density Dd per kilometre used in geospatially estimating the map in the study is given by *Equation 1*:

$$Dd = \frac{L}{A} \tag{1}$$

where L is the total length of the channel in kilometres and A is the areal expanse of the study in square kilometres. Lineaments, which are made up of intersecting linear features, provide important information about the occurrence, flow, and storage of groundwater. They act as helpful checklists for locating prospective groundwater resources (Adewumi et al., 2023; Arshad et al., 2020). Lineament density maps were produced for this investigation using the spatial analyzer tool. To identify areas of

varied lineament density, these maps were further categorized, providing essential data for determining groundwater potential.

3.4. Weighting of Thematic Maps using the Analytic Hierarchy Process (AHP)

AHP uses matrices to estimate the relative importance of factors for mathematical decision-making (Ejepu, 2020; Mogaji et al., 2021). Considering one aspect at a time simplifies decision-making and improves transparency and organization (Ifediegwu, 2022; Ghosh et al., 2022). AHP helps decision-makers prioritize goals by placing them at the top of a hierarchy. Its advantage over prior multi-attribute value systems is systematic assessment consistency (Ejepu et al., 2017; Ghosh et al., 2022; Thapa et al., 2022). Change priorities to establish consistency, which can fix inconsistent judgements. Reevaluation is usually needed when the consistency ratio (CR) exceeds 0.1.

The study's topics were assessed using a pairwise comparison matrix indicating groundwater occurrence, transportation, and storage criteria' relative preferences *(Table 2)*. Two themes or classes were explored during weight normalization using AHP (Wind and Saaty, 1980) and Saaty's scale to identify groundwater potential and recharge zones. Pairwise comparison matrices with specified weights were created for each thematic layer and class, and the eigenvector technique normalised them. The consistency ratio (CR) was used to evaluate the thematic layer and class normalised weights (Wind and Saaty, 1980). The CR computation allowed weight accuracy evaluation, guaranteeing a rigorous and open technique for groundwater potential and recharging zone location (Mogaji et al., 2021).

Square matrix: A = a_{ij} *(Equation 2)*, the element of row *i* column j was produced and the lower triangular matrix $L_{ij}$was completed by taking the reciprocal values of entries of the upper diagonal using the expression $\left(L_{ij} = \frac{1}{a_{ij}}\right)$.

$$A = \begin{bmatrix} \frac{p_1}{p_1} & \frac{p_1}{p_j} & \frac{p_1}{p_m} \\ \frac{p_i}{p_1} & 1 & \frac{p_i}{p_m} \\ \frac{p_n}{p_1} & \frac{p_n}{p_j} & \frac{p_n}{p_n} \end{bmatrix} \quad (2)$$

The given *Equation (2)* defines a square matrix A with elements denoted as a_{ij}, where i and j represent the row and column indices, respectively. The elements of this matrix are obtained by dividing the value of p_i by the value of p_j, where p_i and p_j are entries from a given set of numbers p_1, p_2, ..., p_n.

The resulting matrix A will have the form of a lower triangular matrix, where all the elements above the diagonal are zero. This is because the matrix is constructed by dividing values of p_i by values of p_j, where i and j satisfy i ≤ j. Therefore, any

element of A above the diagonal (i.e., $a_{ij}$where i > j) will be of the form p_j /p_i, which is not included in the matrix A.

We use the reciprocal values of the entries in the top diagonal to finish the lower triangular matrix A. We specifically substitute the reciprocal value, 1/a_{ij}, for each element a_{ij} when i > j. Due to the fact that a_{ij}= p_i/p_i = 1, this results in a lower triangular matrix where all the diagonal entries are 1 and all the elements above the diagonal have been swapped out for their reciprocals. The resulting matrix A is a lower triangular matrix that has been finished by using the specified expression to find the reciprocal values of entries on the upper diagonal.

To get normalized relative weight, we divide each element of matrix $a_{ij} = \frac{p_i}{p_j}$ by *Equation 2* to obtain *Equation 3*.

$$\frac{\frac{p_i}{p_j}}{\frac{\sum_{i=1}^{n} p_i}{p_i}} = \frac{p_i}{p_j} \times \frac{p_j}{\sum_{i=1}^{n} p_i} = \frac{p_i}{\sum_{i=1}^{n} p_i} \tag{3}$$

In *Equation (3)*, the fraction ($\frac{p_i}{p_j}$) in the numerator is manipulated by expressing it in terms of the sum of all the values in the set p_1, p_2, ..., p_n, which appears in the denominator. The first step is to divide both the numerator and denominator by p_j, then express ($\frac{p_i}{p_j}$) as the product of p_i and the reciprocal of p_j (Arefin, 2020). The expression is simplified by multiplying both the numerator and denominator by p_j, resulting in the product of p_i and p_j, divided by the square of the sum of all the values in the set p_1, p_2, ..., p_n.

Averaging across the rows to get the normalized Principal Eigenvector (priority vector) i.e., Rate (R_i) or weight of row *i* (W_i) *Equation 4* resulted. Since it is normalized, the sum of all elements in the priority vector should be one.

$$\frac{W_i}{R_i} = \left[\frac{P_i}{\sum_{i=1}^{n} P_i} \ldots\ldots + \cdots \frac{P_i}{\sum_{i=1}^{n} P_1}\right] \times {}^{1}/_{n} \tag{4}$$

To compute λ_{max}, first multiply the normalized value by the respective weight and then, the values of the product are added together to get

$$\lambda_{max} = \frac{C_1 + C_2 + C_3 \ldots C_n}{n} \tag{5}$$

where C_1 to C_n is the λ value and n is the number of criteria. In this research, a λ_{max} value of 5.1966 was obtained.

Eigenvalues are scalar values that are associated with a square matrix and are important in linear algebra and related subjects (Aykut, 2021). Solving the

characteristic equation, which includes determining the roots of a polynomial, yields the eigenvalues of a matrix.

The maximum eigenvalue, or λ_{max}, is the greatest of a matrix's eigenvalues. It may be used to calculate matrix attributes such as stability, convergence rate, and spectral radius. In some applications, obtaining the greatest eigenvalue is desired, and numerical methods can be employed to determine its value. A λ_{max}value of 5.1966 was achieved in this study, suggesting that the matrix under examination has the highest eigenvalue of 5.1966.

A measure of the consistency or degree of consistency of the judgment is called the consistency index, which is calculated using

$$C_i = \frac{(\lambda_{max} - n)}{n-1} \tag{6}$$

where n is the number of criteria taken into account. AHP breaks down complex issues into a hierarchy of criteria, sub-criteria, and alternatives for decision-making (Albayrak and Erensal, 2004; Gillan et al., 2017). Then, each pair of factors is compared for importance or preference. The AHP analysis calculates a $C_i$value by calculating the matrix of pairwise comparisons, which includes the decision maker's subjective opinions. After normalisation, the matrix's eigenvector shows the decision's criterion or alternatives' weights (Gillan et al., 2017).

This study produced a CI value of 0.04915, indicating a consistent pairwise comparison matrix. This number is often compared to a random index or C_i's anticipated value to determine consistency. If the $C_i$value is higher than predicted, the judgements may be wrong and require further investigation or matrix revision. Pairwise comparisons were examined using the Consistency Ratio (CR) within each thematic layer (Wind and Saaty, 1980). CR was calculated using *Equation 7*:

$$CR = \frac{C_i}{RCI} \tag{7}$$

C_i stands for consistency index.

The pairwise comparison matrix's consistency is measured by Saaty's RCI. This formula was established by Saaty (1987), and the outcomes depend on how many variables are compared. If the C_i value is greater than the RCI, the results may be wrong or the pairwise comparison matrix has to be changed or examined. A 5-variable pairwise comparison matrix for the study's RCI is 1.12. This value can be compared to the pairwise comparison matrix $C_i$value. CI values below 1.12 indicate matrix consistency. If the $C_i$value is more than 1.12, the pairwise comparison matrix is inconsistent and may need further investigation or change.

The computed CR achieved in this investigation is 0.04915, which is less than the threshold value of 0.10 (Mogaji et al., 2021; Wind and Saaty, 1980), indicating an acceptable level of inconsistency. If the CR is greater than 0.10, judgments

should be reevaluated to ensure consistency in the decision-making process. After allocating rates for classes within each layer and weights for the thematic layers, a weighted overlay method was used to create the final map (Tamiru and Wagari, 2021; Girma, 2022). *Equation 8* was applied to the spatial analysis tool in ArcGIS 10.8 to calculate the groundwater potential index (GWPI).

$$GWPI = \sum_{i=1}^{n} W_i \times R_i \quad (8)$$

where W_i is the weight for each thematic layer and R_i is rates for the classes within a thematic layer derived from AHP.

Table 2

Measurement scale of AHP (Wind and Saaty, 1980)

Scale	Definition	Explanation
1	Equal importance	Two elements contribute equally to the objective.
3	Moderate importance	Experience and judgment slightly favour one element over another.
5	Strong importance	Experience and judgment strongly favour one element over another.
7	Very strong importance	One element is favoured very strongly over others. Its dominance is demonstrated in practice.
9	Extreme importance	The evidence favouring one element over another is of the highest possible order of affirmation.
2, 4, 6, 8	Intermediate value between the two adjacent judgments	It can be used to express intermediate values.

The weights assigned to each thematic layer were determined using the Analytical Hierarchy Process (AHP) method. AHP is a decision-making technique that allows for the systematic comparison and ranking of alternatives based on multiple criteria.

The criteria were the different thematics (Rainfall, Geology, Slope, Drainage Density, LULC, Lineament Density, and Soil Type) and the alternatives were the different areas in the study region. The pairwise comparison matrix was filled out using a scale of 1 to 9, with 1 indicating equal importance and 9 indicating extreme importance. Comparing Rainfall and Geology, a value of 9 might indicate that Rainfall is much more important than Geology, while a value of 1 might indicate that they are equally important.

Table 3

Matrix of Environmental Factors and Normalized Principal Eigenvector Percentages for Groundwater Potential

Matrix		Rainfall	Geology	Slope	Drainage Density	LULC	Lineament Density	Soil Type	Normalized principal Eigenvector (%)
		1	2	3	4	5	6	7	
Rainfall	1	1	3	3	5	5	5	7	39.5
Geology	2	1/3	1	3	3	5	5	5	23.5
Slope	3	1/3	1/3	1	1	3	3	5	12.5
Drainage Density	4	1/5	1/3	1	1	1	2	3	8.0
LULC	5	1/5	1/5	1/3	1	1	1	3	6.1
Lineament Density	6	1/5	1/5	1/3	½	1	1	1	5.4
Soil Type	7	1/7	1/5	1/5	1/3	1/3	1	1	5.0

The AHP approach was used to calculate the weights for each theme after the pairwise comparison matrices for each thematic layer were finished. Based on the pairwise comparison matrix, the AHP technique applies a mathematical formula to determine the relative weights of the criterion. The proportionate weights given to each theme were based on how important they were in assessing the research area's overall suitability for a certain application. Rainfall (39.5%), Geology (23.5%), Slope (12.5%), Drainage Density (8.0%), LULC (6.1%), Lineament Density (5.4%), and Soil Type (5.0%) were given the following weights in this scenario as shown in *Table 3*. These weights represent how significant each theme is in assessing the study area's overall suitability for various applications, such as land-use planning or natural resource management. By assigning weights to each thematic based on their relative importance, the AHP method can provide a more objective and systematic approach to decision-making in GIS analysis.

4. RS AND GIS ANALYSIS

4.1. Lineament and Lineament Density

Lineaments are linear characteristics seen on the surface that act as markers for fissures and cracks connected to the presence of groundwater (Suganthi et al., 2013; Sahu et al., 2022). According to Mabee et al. (1994), Magowe and Carr (1999), and Solomon and Ghebreab (2006), these lineaments can be cracks, faults, fractures, and

other geological formations that have linear properties or behave as groundwater flow channels. Given the importance of lineaments in the transport and storage of groundwater, the study imported lineament data into the ArcGIS environment and used the spatial analyst tool to produce a map of the density of lineaments in the studied area. A visual representation of the developed lineament density map is shown in *Figure 3*. The lineament density map measures the length of linear features per unit area and, by highlighting locations with higher lineament density—which often correlate to permeable layers or units—indirectly indicates groundwater potential. According to Solomon and Ghebreab (2006), lineament density polygons with higher density values indicate greater groundwater recharge and, therefore, improved groundwater prospects. The places with the highest lineament density are given the highest rating value to emphasize their importance for groundwater storage. Additionally, lineament crossings are prospective sites for groundwater storage, suggesting that regions with a lot of lineaments may have a lot of groundwater potential.

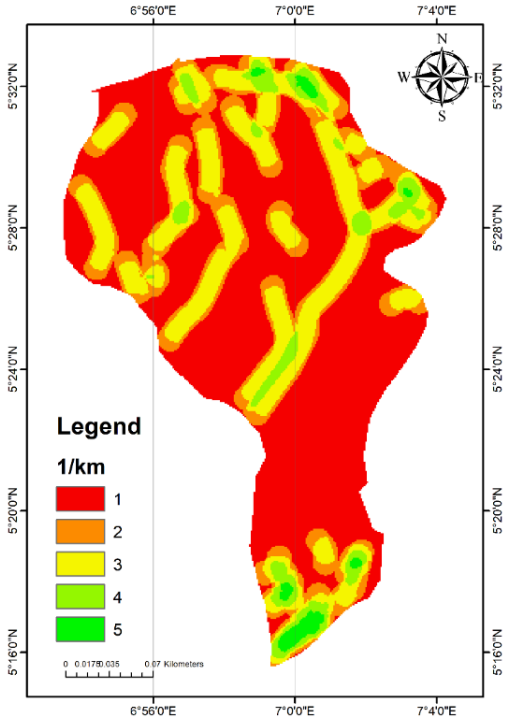

Figure 3

Reclassified lineament density of the study area

4.2. Land use/Land cover Map

The land use and cover of the research region affect the presence of groundwater. The results of the supervised classification of the land use and land cover maps are shown in *Figure 4*. The investigation showed that forests, built areas, and

rangelands—three forms of land cover—dominate the research region. Groundwater is significantly impacted by land use and cover because it influences runoff by reducing or encouraging runoff and because it can also help plants retain water on their surfaces (Fan et al., 2022). The water droplets that are caught during this procedure eventually fall to the ground and help replenish the groundwater table. However, it is crucial to remember that, assuming a continual interception process occurs, land use and land cover can also negatively impact groundwater through evapotranspiration.

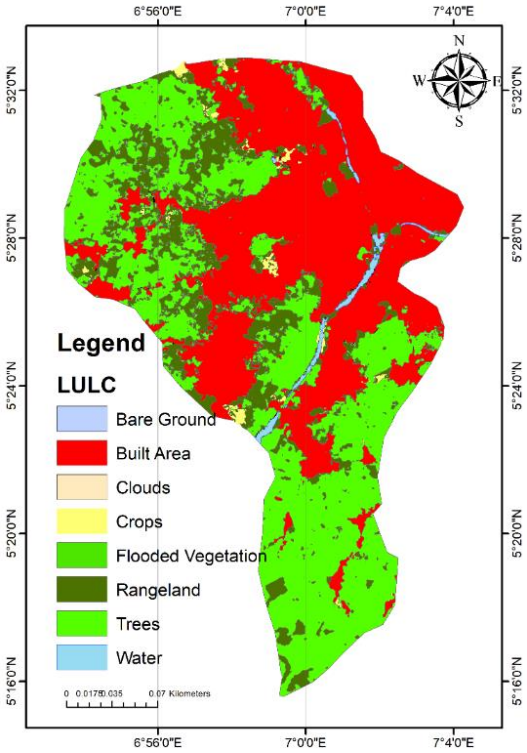

Figure 4

Land Use / Cover map of the study area

4.3. Drainage and Drainage Density Maps

Figure 5, which was directly derived from the DEM data, shows the drainage system of the study region. The type of vegetation, the soil's ability to absorb precipitation, infiltration, and the slope's gradient all have an impact on the drainage pattern. It performs as an essential hydrogeological characteristic indicator. The ratio of the total stream lengths to the region under consideration is represented by the surface drainage density, which is expressed in kilometres per square kilometre. Low drainage density areas encourage infiltration and lessen surface runoff, which is advantageous for the development of groundwater (Cotton, 1964; Luijendijk, 2022). According to *Figure 5*, the research region has a range of drainage densities between 1

and 5 km^{-1}, with a sizeable percentage being made up of low-density zones between 1 and 2 km^{-1}. This suggests that the study area has significant groundwater potential (Ekanem et al., 2022).

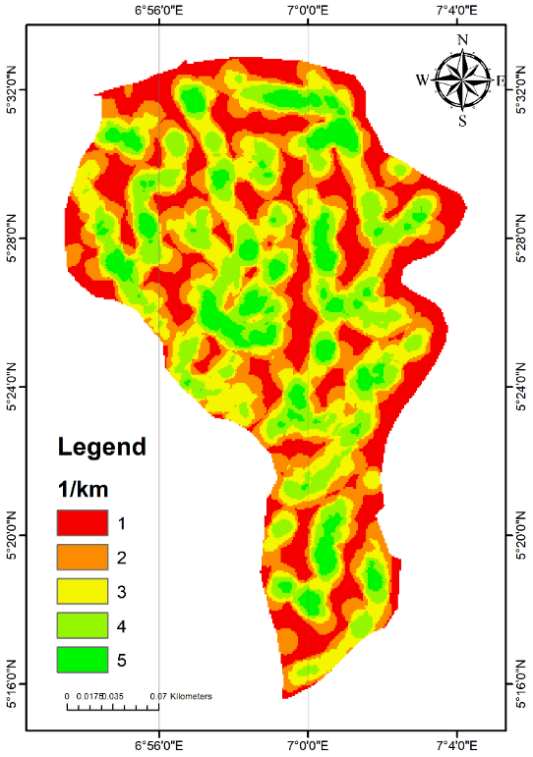

Figure 5
Drainage Density of the study area

4.4. Slope Maps

Groundwater infiltration and recharge are significantly influenced by the slope of the surface. It can shed light on the potential for groundwater in a particular area when used in conjunction with other geomorphic characteristics. Rainwater has more time to soak into the earth and replenish the groundwater system in low-slope locations since there is less surface runoff in these areas. High-slope locations, on the other hand, often have quick surface runoff, which reduces the amount of time that an area can be occupied by infiltration and recharging. In this study, DEM data and the spatial analyst tool in ArcGIS were used to create the slope map *(Figure 6)* of the research area. A slope of 1 degree is typically shown on the slope map in *Figure 6*, which indicates a strong potential for infiltration and recharge. This may indicate that the area has greater water potential (Magesh et al., 2012).

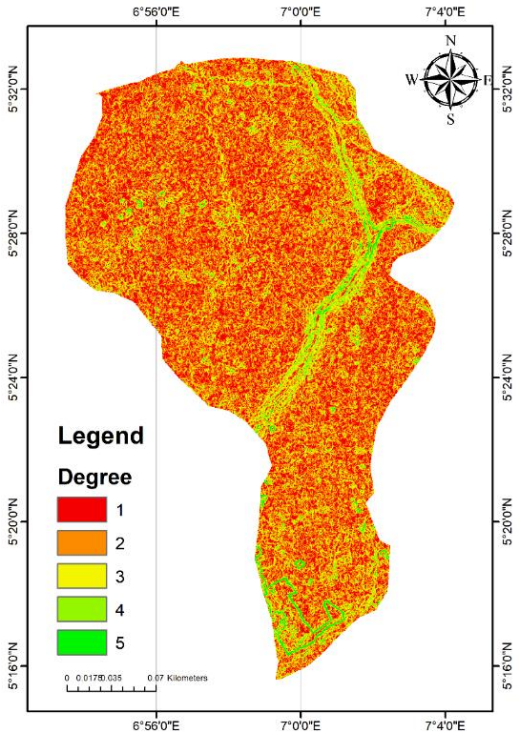

Figure 6
The slope of the study area

4.5. Soil Type Map

To develop the lithology layer for this investigation, the existing soil type map was digitalized. As illustrated in *Figure 7*, the examination of the remote sensing data revealed that sandy soils predominate in the region, with little sandy clay. According to Ekanem et al. (2022), this shows that the area is distinguished by porous and permeable soil, indicating a significant potential for groundwater.

Xantric Ferralsols are permeable, well-drained soils that are typical in tropical climates. They include a lot of iron and aluminium, which makes it simple for water to infiltrate and lessens surface runoff. Their moderate to high fertility and ability to serve as natural filters reduce the amount of toxins that seep into the groundwater. Dystric Nitosols, on the other hand, have low fertility and a high clay content. They frequently inhabit chilly regions with average to high rainfall. Their low permeability prevents groundwater recharging by encouraging surface runoff and preventing water infiltration. Because of the poor natural fertility, there may be a tendency to use more fertilizer, which, if used improperly, might contaminate groundwater (Adewumi et al., 2023).

However, the low permeability and low fertility of dystric nitosols may prevent groundwater recharge and increase the usage of fertilizers, both of which increase

the danger of groundwater contamination. These soil features should be taken into account for managing groundwater supplies and maintaining water quality (George et al., 2022).

Another important factor to consider is the type of soil in the area. Soils with high water-holding capacity, such as clay-rich soils, can retain water for longer periods, allowing it to percolate down into the ground and recharge the aquifers. Sandier soils, on the other hand, may not be able to hold onto as much water, resulting in a lesser potential for groundwater. Groundwater potential is significantly influenced by rainfall. The potential for groundwater in a region is greatly influenced by factors such as soil type, rainfall intensity, volume, and distribution.

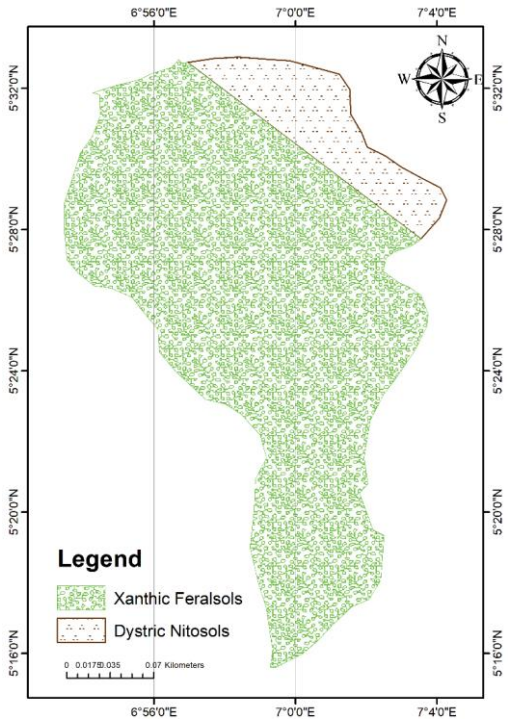

Figure 7
Soil Type of the study area

4.6. Rainfall

Rainfall data is critical in geomorphology studies because it helps identify places with varied levels of groundwater potential. *Figure 8* shows the various rainfall within the study area. Groundwater potential is higher in areas with high yearly rainfall because there is more water available to filter into the ground and recharge aquifers. Regions with little annual rainfall, on the other hand, have reduced groundwater potential since there is less water available for recharge.

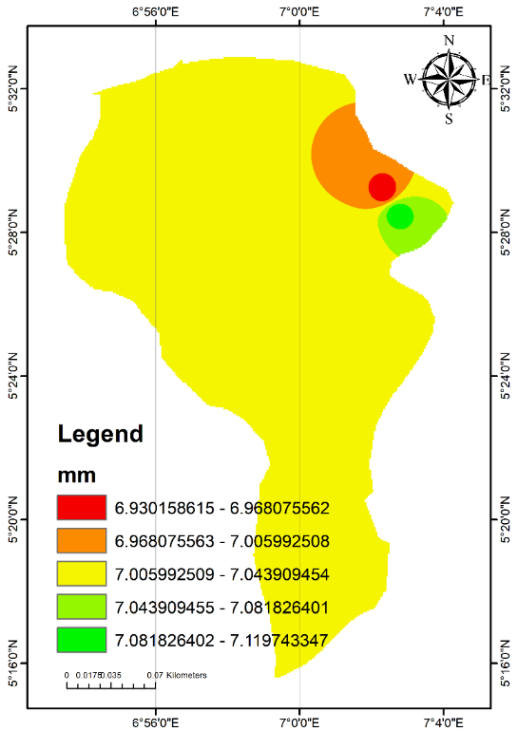

Figure 8
Rainfall of the study area

However, it is important to note that rainfall timing and distribution are also important factors in affecting groundwater potential. If a location receives a large amount of rainfall in a short period of time, the water may not have enough time to soak into the earth and effectively recharge the aquifers. Similarly, irregular rainfall distribution throughout the year may not be enough to keep groundwater levels stable during dry months. As a result, rainfall data is a core sort of geomorphology data utilized in hydrological studies, which are critical in assessing a region's water resources (Adewumi et al., 2023).

4.7. Geology

Aquifer units, particularly sandstone layers, are present in the Benin Formation *(Figure 9)* and play a crucial role in the storage and transport of groundwater (George et al., 2022). The sandstones have increased porosity and permeability, which allows water to pass through and makes it easier to extract groundwater. Rainfall infiltration is the primary mechanism by which groundwater is recharged, and regions with sufficient precipitation and infiltration conditions have a high potential for recharging. The thickness, extent, porosity, and saturation levels of the sandstone aquifers within the Benin Formation can affect how much groundwater

they can hold. To ensure groundwater quality within the formation, potential sources of contamination, such as agriculture, industry, and natural mineral deposits, should be taken into account. Groundwater quality varies depending on local geology and hydrogeological conditions (George et al., 2022).

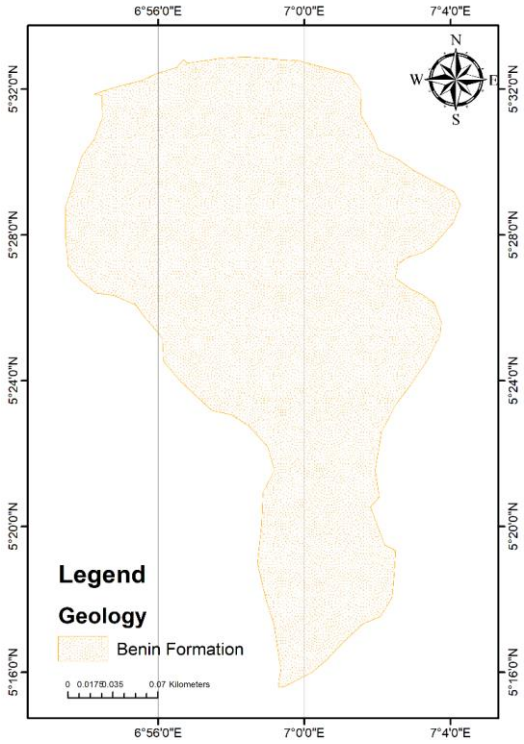

Figure 9
Geology of the study area

4.8. Groundwater Potential Map

The groundwater potential index map, as shown in *Figure 10*, is the result of the combination of numerous thematic maps. The groundwater potential index (GPI) map for the research area was created by allocating weights and combining the thematic maps pertaining to groundwater occurrence, transit, storage, and recharge. Three distinct zones—poor, fair, good, and excellent—are shown on the map. After thorough consideration, it becomes clear that the lineament density, slope, land use, and soil type are the main determinants of the groundwater potential in the research region. Particularly, there is enormous groundwater potential in the southern areas of the region, which are distinguished by a high lineament density and various slope conditions. The study's overall finding is that the area's groundwater potential index ranges from poor to excellent. These results are consistent with those of Ikpe et al. (2022) and Ejepu et al. (2022) studies.

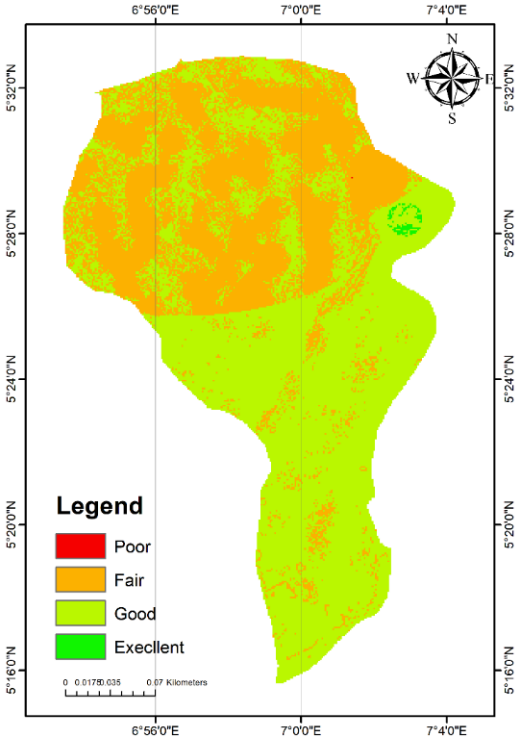

Figure 10

Groundwater Potential area of the study area

According to the analysis, the most important elements affecting groundwater potential were rainfall (39.5%), geology (23.5%), slope (12.5%), drainage density (8.0%), land use/land cover (6.1%), lineament density (5.4%), and soil type (5.0%). A high degree of consistency in the conclusions reached was shown by the computed consistency ratio (CR) for this study, which was found to be 0.04915, much below the criterion of 0.10. Rainfall, geology, soil type, lineament density, slope, drainage density, and land use or cover affected groundwater potential in the study region. The AHP method made ranking these components by importance in determining groundwater potential easier. Combining the maps produced a complete groundwater potential map of the research region. The study found modest groundwater potential with patches of excellent potential within its limitations. Southern portions of the research area had fair to good groundwater potential.

This study reveals how important multiple elements are when measuring groundwater potential. For successful water resource management and planning, geology, rainfall, slope, drainage density, lineament density, and land use and cover must be considered to identify high groundwater potential. The study found that modest slopes and lineament densities from 1 to 5 km^{-1} were common in the area. The study found considerable regional variations in the study area's groundwater potential, which were highly connected with other factors. High rainfall, good geology, low to

average slopes, high drainage density, high lineament density, and optimal land use and cover have been shown to have great groundwater potential. Zones with low to moderate slopes and high lineament density have the most groundwater potential.

5. CONCLUSION

The analysis conducted for this study provides crucial insights into the potential for groundwater in the studied area. Lineament density, an indicator of permeable units, is important for groundwater potential estimation. Higher lineament densities improved groundwater outlooks and recharge potential. Groundwater storage was also considered at line intersections. This information can influence future groundwater investigations. According to the land use and land cover map, the research region had many trees, population areas, and rangeland. Vegetation aids the groundwater cycle by reducing runoff and encouraging infiltration. Land cover's water-holding capacity helps recharge groundwater. Careful management of land use and land cover on groundwater potential reduces contamination risk.

The drainage and drainage density maps illustrate that the drainage system is important for hydrogeological evaluation. Groundwater growth was best in low drainage density areas because they increased infiltration and reduced surface runoff. The analysis showed that the studied region had several low drainage densities, indicating a large groundwater potential. Groundwater infiltration and recharging were controlled by slope in the studied region. Low slope readings suggested enhanced infiltration and groundwater residence time, increasing groundwater potential.

The soil type map showed the research area's aquifer rocks' porosity and permeability. Permeable and filtering xantric ferralsols were found to recharge groundwater and filter pollution. However, dystric nitosols' low permeability and fertility made groundwater recharge difficult and polluting. Groundwater potential depended heavily on rainfall data. High annual rainfall locations have higher groundwater potential because more water is available for infiltration and aquifer recharge. The timing and distribution of rainfall must be considered to ensure efficient recharge and groundwater stability year-round.

An index map of groundwater potential was created when all theme maps were integrated. Zones of low, moderate, and extraordinary groundwater potential were delineated in the research area. The correctness of the groundwater potential map was guaranteed by the regular and precise weighing of components according to relevance. This work emphasises a comprehensive approach that combines remote sensing, GIS analysis, and the AHP. Groundwater potential and occurrence can be comprehended with the use of advanced instruments and a variety of variables. Planning, groundwater sustainability, and the management of water resources are all dependent on this knowledge in the research region.

By considering variables including lineament density, land use and cover, drainage density, slope, soil type, geology, and rainfall, a full understanding of groundwater occurrence, storage, and recharge patterns has been gained. In order to ensure that the groundwater resources of the area are utilized sustainably, the findings might

serve as a starting point for upcoming groundwater exploration, management, and planning projects.

ACKNOWLEDGEMENTS

We express our gratitude to the Department of Geology at the Federal University of Technology, Owerri, Nigeria, Okan Geoservices Nigeria Limited, Nigeria, and the Department of Geological Sciences at Nnamdi Azikiwe University, Awka, Nigeria for providing valuable resources essential to the completion of this research. Our sincere appreciation also extends to the Editor and reviewers for their insightful contributions and guidance.

REFERENCES

Abdulrazzaq, Z. T., Agbasi, O. E., Aziz, N. A., Etuk, S. E. (2020). Identification of potential groundwater locations using geophysical data and fuzzy gamma operator model in Imo, Southeastern Nigeria. *Applied Water Science*, 10 (8), p. 188.

Aboyeji, O. O. (2013). Freshwater Pollution in Some Nigerian Local Communities, Causes, Consequences and Probable Solutions. *Academic Journal of Interdisciplinary Studies*. http://dx.doi.org/10.5901/ajis.2013.v2n13p111

Adewumi, R., Agbasi, O. E., Mayowa, A. (2023). Investigating groundwater potential in northeastern basement complexes: A Pulka case study using geospatial and geo-electrical techniques. *HydroResearch*, 6, pp. 73–88. http://dx.doi.org/10.1016/j.hydres.2023.02.003

Agbasi, O. E., Aziz, N. A., Abdulrazzaq, Z. T., Etuk, S. E. (2019). Integrated Geophysical Data and GIS Technique to Forecast the Potential Groundwater Locations in Part of South Eastern Nigeria. *Iraqi Journal of Science*, 60 (5), pp. 1013–1022. http://dx.doi.org/10.24996/ijs.2019.60.5.11.

Agbasi, O. E., Etuk S. E. (2016). Hydro-Geoelectric Study of Aquifer Potential in Parts of Ikot Abasi Local Government Area, Akwa Ibom State, Using Electrical Resistivity Soundings. *International Journal of Geology and Earth Sciences*, 2 (4) pp. 43–54.

Agidi, B. M., Akakuru, O. C., Aigbadon, G. O., Schoneneich, K., Isreal, H., Ofoh, I., … Somonu, I. (2022). Water quality index, hydrogeochemical facies and pollution index of groundwater around Middle Benue Trough, Nigeria. *International Journal of Energy and Water Resources*, http://dx.doi.org/10.1007/s42108-022-00187-z.

Akaolisa, C. C. Z., Agbasi, O., Okeke, O. C., Okechukwu, S. (2022). An assessment of the groundwater potentials of the farm with preliminary geophysical method and grain size analysis prior to the drilling of boreholes. *HydroResearch*, 5, pp. 85–98. http://dx.doi.org/10.1016/j.hydres.2022.09.001

Akaolisa, C. C. Z., Ibeneche, W., Ibeneme, S., Agbasi, O. E., Okechukwu, S. (2022). Enhance groundwater quality assessment using integrated vertical electrical sounding and physio-chemical analyses in Umuahia South, Nigeria. *International Journal of Energy and Water Resources*, http://dx.doi.org/10.1007/s42108-022-00219-8.

Akaolisa, C. C. Z., Ofoh, I., Agbasi, O. E., Okoli, E. A., Okechukwu, S. (2022). Hydrogeochemical Data: A Tool for Mapping Aquifer Contamination from Landfill Dumpsites within Owerri Metropolis and Environs Southeastern Nigeria. *Civil Engineering Beyond Limits*, 2 (2022). https://doi.org/10.36937/cebel.2022.1571

Akinlalu, A. A., Mogaji, K. A., Adebodun, T. S. (2021). Assessment of aquifer vulnerability using a developed "GODL" method (modified GOD model) in a schist belt environ, Southwestern Nigeria. *Environmental Monitoring and Assessment*, 193 (4). http://dx.doi.org/10.1007/s10661-021-08960-z

Aladeboyeje, A. I., Coker, J. O., Agbasi, O. E., Inyang, N. J. (2021). Integrated hydrogeophysical assessment of groundwater potential in the Ogun drainage basin, Nigeria. *International Journal of Energy and Water Resources*, 5 (4), pp. 461–475. http://dx.doi.org/10.1007/s42108-021-00121-9

Albayrak, E., Erensal, Y. C. (2004). Using analytic hierarchy process (AHP) to improve human performance: An application of multiple criteria decision making problem. *Journal of Intelligent Manufacturing*, 15 (4), pp. 491–503. http://dx.doi.org/10.1023/b:jims.0000034112.00652.4c.

Arefin, R. (2020). Groundwater potential zone identification at Plio-Pleistocene elevated tract, Bangladesh: AHP-GIS and remote sensing approach. *Groundwater for Sustainable Development*, 10, 100340. http://dx.doi.org/10.1016/j.gsd.2020.100340

Arshad, A., Zhang, Z., Zhang, W., Dilawar, A. (2020). Mapping favorable groundwater potential recharge zones using a GIS-based analytical hierarchical process and probability frequency ratio model: a case study from an agro-urban region of Pakistan. *Geoscience Frontier*, 11 (5), pp. 1805–1819.

Aykut, T. (2021). Determination of groundwater potential zones using Geographical Information Systems (GIS) and Analytic Hierarchy Process (AHP) between Edirne-Kalkansogut (northwestern Turkey). *Groundwater for Sustainable Development*, 12, 100545. http://dx.doi.org/10.1016/j.gsd.2021.100545

Bangen, S. G., Wheaton, J. M., Bouwes, N., Bouwes, B., Jordan, C. (2014). A methodological intercomparison of topographic survey techniques for characterizing wadeable streams and rivers. *Geomorphology*, 206, pp. 343–361. http://dx.doi.org/10.1016/j.geomorph.2013.10.010

Cotton C. A. (1964). The control of drainage density. *New Zealand Journal of Geology and Geophysics*, 7 (2), pp. 348–352. http://dx.doi.org/10.1080/00288306.1964.10420180

Dinagarapandi, P., Saravanan, K., Mohan, K. (2020). Delineation of potential groundwater zones based on multicriteria decision making technique. *Journal of Groundwater Science and Engineering*, 8 (2), pp. 180–194. http://dx.doi.org/10.19637/j.cnki.2305-7068.2020.02.009

Ejepu, J. S., Jimoh, M. O., Abdullahi, S., Mba, M. A. (2022). Groundwater Exploration Using Multi Criteria Decision Analysis and Analytic Hierarchy Process in Federal Capital Territory, Abuja, Central Nigeria. *International Journal of Geosciences*, 13 (1), pp. 33–53.

Ejepu, J. S., Olasehinde, P., Okhimamhe, A. A., Okunlola, I. (2017). Investigation of hydrogeological structures of Paiko region, north-Central Nigeria using integrated geophysical and remote sensing techniques. *Geosciences*, 7 (4), p. 122.

Ejepu, J. S. (2020). Regional assessment of groundwater potential zone using remote sensing, GIS and multi criteria decision analysis techniques. *Nigerian Annals of Pure and Applied Sciences*, 3 (3b), pp. 99–111.

Ekanem, A. M., Ikpe E. O., George, N. J., Thomas J. E. (2022). Integrating geoelectrical and geological techniques in GIS-based DRASTIC model of groundwater vulnerability potential in the raffia city of Ikot Ekpene and its environs, southern Nigeria. *International Journal of Energy and Water Resources*. https://doi.org/10.1007/s42108-022-00202-3

Fan, L., Jianhua, W., Fei, X., Yongqiang, Y., Qianqian, D. (2022). Determination of the spatial correlation characteristics for selected groundwater pollutants using the geographically weighted regression model: A case study in Weinan, Northwest China. *Human and Ecological Risk Assessment: An International Journal*, 4, pp. 1–23.

Fasunwon, O. O., Olowofela, J. A., Akinyemi, O. D., Oluwatosin E. (2007). Contaminants Evaluation as Indicators of Water Quality in Ago-Iwoye, Southwestern, Nigeria. *Symposium on the Application of Geophysics to Engineering and Environmental Problems 2007*. http://dx.doi.org/10.4133/1.2924680

George, N. J., Agbasi, O. E., Umoh, J. A., Ekanem, A. M., Ejepu, J. S., Thomas, J. E., Udoinyang, I. E. (2022). Contribution of electrical prospecting and spatiotemporal variations to groundwater potential in coastal hydro-sand beds: a case study of Akwa Ibom State, Southern Nigeria. *Acta Geophysica*. http://dx.doi.org/10.1007/s11600-022-00994-2

Ghosh, A., Adhikary, P. P., Bera, B., Bhunia, G. S., Shit, P. K. (2022). Assessment of groundwater potential zone using MCDA and AHP techniques: Case study from a tropical river basin of India. *Applied Water Science*, 12, 37.

Gillan, J., Karl, J., Elaksher, A., Duniway, M. (2017). Fine-Resolution Repeat Topographic Surveying of Dryland Landscapes Using UAS-Based Structure-from-Motion Photogrammetry: Assessing Accuracy and Precision against Traditional Ground-Based Erosion Measurements. *Remote Sensing*, 9 (5) 437. http://dx.doi.org/10.3390/rs9050437

Girma, D. (2022). Identification of Groundwater Potential Zones Using AHP, GIS and RS Integration: A Case Study of Didessa Sub-Basin, Western Ethiopia. *Remote Sensing of Land*, 6, pp. 1–15. http://dx.doi.org/10.21523/gcj1.2022060101

Ibe Sr, K., Sowa, A. (2002). Hydrology of part of the Oramiriukwa River basin, southeast of Owerri, Imo State, Nigeria. *Hydrogeology Journal*, 10 (4), pp. 509–521. http://dx.doi.org/10.1007/s10040-002-0207-7

Ibuot, J. C., Aka, M. U., Inyang, N. J., Agbasi, O. E. (2022). Georesistivity and physicochemical evaluation of hydrogeologic units in parts of Akwa Ibom State, Nigeria. *International Journal of Energy and Water Resources*. http://dx.doi.org/10.1007/s42108-022-00191-3

Ifediegwu, S. I. (2022). Assessment of groundwater potential zones using GIS and AHP techniques: A case study of the Lafia district, Nasarawa State, Nigeria. *Applied Water Science*, 12, 10.

Ikpe, E. O., Ekanem, A. M., George, N. J. (2022). Modelling and assessing the protectivity of hydrogeological units using primary and secondary geo-electric indices: a case study of Ikot Ekpene Urban and its environs, southern Nigeria. *Modeling Earth Systems and Environment*. https://doi.org/10.1007/s40808-022-01366-x

Kessar, C., Benkesmia, Y., Blissag, B. et al. (2021). Delineation of groundwater potential zones in Wadi Saida Watershed of NW-Algeria using remote sensing, geographic information system-based AHP techniques and geostatistical analysis. *Journal of Groundwater Science and Engineering*, 9 (1), pp. 45–64. http://dx.doi.org/10.19637/j.cnki.2305-7068.2021.01.005

Kumar, P., Bansod, B. K. S., Debnath, S. K., Thakur, P. K., Ghanshyam, C. (2015). Index-based groundwater vulnerability mapping models using hydrogeological settings: A critical evaluation. *Environmental Impact Assessment Review*, 51, pp. 38–49. http://dx.doi.org/10.1016/j.eiar.2015.02.001

Luijendijk, C. (2022). Transmissivity and groundwater flow exert a strong influence on drainage density. *Earth Surface Dynamics*, 10 (1), pp. 1–22.

Mabee, S. B. Hardcastle, K. C., Wise, D. U. (1994). A method of collecting and analyzing lineaments for regional-scale fractured-bedrock aquifer studies. *Ground Water*, 32 (6), pp. 884–894.

Magesh, N. S., Chandrasekar, N., Soundranayagam, J. P. (2012). Delineation of groundwater potential zones in Theni district, Tamil Nadu, using remote sensing, GIS and MIF techniques. *Geoscience Frontiers*, 3 (2), pp. 2189–2196.

Magowe, M., Carr, J. R. (1999). Relationship between lineaments and ground water occurrence in western Botswana. Ground Water 37 (2), pp. 282–286.

Mogaji, K. A. (2016). Combining geophysical techniques and multi-criteria GIS-based application modeling approach for groundwater potential assessment in south-western Nigeria. *Environmental Earth Sciences*, 75 (16). http://dx.doi.org/10.1007/s12665-016-5897-6

Mogaji, K. A., Ezekiel, G. I., Abodunde, O. O. (2021). Modeling of aquifer potentiality using GIS-based knowledge-driven technique: a case study of hard rock geological setting, southwestern Nigeria. *Sustain. Water Resources and Management*, 7 (64). https://doi.org/10.1007/s40899-021-00538-4

Opara, A. I., Eke, D. R., Onu, N. N., Ekwe, A. C., Akaolisa, C. Z., Okoli, A. E., Inyang, G. E. (2020). Geo-hydraulic evaluation of aquifers of the Upper Imo River Basin, Southeastern Nigeria using Dar-Zarrouk parameters. *International Journal of Energy and Water Resources*, 5 (3), pp. 259–275. http://dx.doi.org/10.1007/s42108-020-00099-w

Roy, S. S., Rahman, A., Ahmed, S., Ahmad, I. A. (2022). Long-term trends of groundwater level variations in response to local level land use land cover changes in Mumbai, India. *Groundwater for Sustainable Development*, 18, 100797. http://dx.doi.org/10.1016/j.gsd.2022.100797

Saaty, R. W. (1987). The analytic hierarchy process-what it is and how it is used. *Math. Model.*, 9, pp. 161–176.

Saaty, T. L. (1980). The Analytic Hierarchy Process. New York, NY, McGrawHill, USA.

Sahu, U., Wagh, V., Mukate, S., Kadam, A., Patil, S. (2022). Applications of geospatial analysis and analytical hierarchy process to identify the groundwater recharge potential zones and suitable recharge structures in the Ajani-Jhiri watershed of north Maharashtra, India. *Groundwater Sustain. Development*, 17, 100733.

Sander, P. (2006). Lineaments in groundwater exploration: a review of applications and limitations. *Hydrogeology Journal*, 15 (1), pp. 71–74. http://dx.doi.org/10.1007/s10040-006-0138-9.

Sharma, M., Paige, G. B., Miller, S. N. (2010). DEM Development from Ground-Based LiDAR Data: A Method to Remove Non-Surface Objects. *Remote Sensing*, 2 (11), pp. 2629–2642. http://dx.doi.org/10.3390/rs2112629

Solomon, S., Ghebreab, W. (2006). Lineament characterization and their tectonic significance using Landsat TM data and field studies in the central highlands of Eritrea. *Journal of African Earth Sciences*, 46, pp. 371–378.

Suganthi, S., Elango, L., Subramanian, S. K. (2013). Groundwater potential zonation by remote sensing and GIS techniques and its relation to the groundwater level in the coastal part of the Arani and Koratalai river basin, Southern India. *Earth Science Research Journal*, 17, pp. 87–95.

Tamiru, H., Wagari, M. (2021). Evaluation of data-driven model and GIS technique performance for identification of groundwater potential zones: A case of Fincha Catchment, Abay Basin, Ethiopia. *Journal of Hydrology: Regional Studies*, 37, 100902. https://doi.org/10.1016/j.ejrh.2021.100902

Wind, Y., Saaty, T. L. (1980). Marketing applications of theanalytic hierarchy process. *Management Science*, 26, pp. 641–658.

Yisa, J., Jimoh, T. (2010). Analytical Studies on Water Quality Index of River Landzu. *American Journal of Applied Sciences*, 7 (4) pp. 453–458. http://dx.doi.org/10.3844/ajassp.2010.453.458

Geosciences and Engineering, Vol. 12, No. 1 (2024), pp. 57–74.
https://doi.org/10.33030/geosciences.2024.01.004

EXPLORING FOURIER TRANSFORMATIONS: BENEFITS, LIMITATIONS, AND APPLICATIONS IN ANALYZING TWO-DIMENSIONAL RIGHT RECTANGULAR PRISM'S MAGNETIC FIELD

KHOULOUD JLAIEL
Institute of Exploration Geosciences, University of Miskolc,
Khouloud.jlail@enis.tn
https://orcid.org/0009-0005-8503-1934

Abstract: Fourier Transformations are crucial in signal processing, offering a unique approach for complex data analysis. This paper explores their advantages and limitations, explaining key concepts like Fourier Transformation, Fourier series, Discrete Fourier Transform, and Continuous Fourier Transform, focusing on practical applications. The strengths, such as signal decomposition into frequency components, are exemplified through a case study on the total magnetic field of two-dimensional right rectangular prisms. However, limitations arise with non-stationary signals due to the assumption of stationarity. Alternative methods like the Wavelet Transformation and Short-Time Fourier Transformation are briefly discussed. Serving as a practical guide, this paper aids researchers in utilizing Fourier Transformations while recognizing scenarios where alternative techniques may be more suitable.

Keywords: *Discrete Fourier Transform, Continuous Fourier Transform, Wavelet Transform, Short-Time Fourier Transform, Right Rectangular Prisms*

1. INTRODUCTION

The roots of Fourier Transformations can be traced back to the pioneering work of Joseph Fourier, a renowned French mathematician and physicist of the 18th century. Fourier's groundbreaking contributions to the field of mathematics included the development of these transformative techniques. He introduced Fourier series as a powerful tool for analyzing periodic functions and decomposing complex signals into a series of simpler trigonometric components. Over the centuries, Fourier's work laid the foundation for significant advances in various scientific and engineering disciplines (Trigg, 2005) (Baron Fourier, 2003) (Oppenheim, 1999a).

As time progressed, Fourier Transformations evolved from their classical origins into an indispensable mathematical framework for addressing a wide range of contemporary challenges. Today, they are an integral part of fields such as signal processing, image analysis, data interpretation, and more. Their adaptability and utility continue to expand, as they provide valuable insights into the frequency-domain representation of data, enabling us to understand the hidden patterns and structures in complex information (Gray and Goodman, 2012; Briggs and Henson, 1995).

In our data-driven world, the growing complexity and volume of information present both opportunities and challenges. The significance of this study lies in its

exploration of the modern applications of Fourier Transformations, highlighting their pivotal role in contemporary data analysis and interpretation. Understanding how to harness these mathematical techniques in the face of increasingly intricate and large datasets is crucial for researchers, scientists, and engineers across numerous domains.

This study aims to shed light on the nuanced and evolving landscape of Fourier Transformations, revealing their applications, benefits, and limitations in a data-centric context. By doing so, it offers valuable insights into addressing the challenges associated with the processing and interpretation of complex data, equipping practitioners with the tools and knowledge needed to make informed decisions and drive innovation in their respective fields. The paper covers Fourier Transformations comprehensively.

2. FUNDAMENTAL CONCEPTS OF FOURIER TRANSFORMATIONS

2.1. Fourier Transforms

In this section we will introduce the Fourier Transform as a universal problem-solving technique. We investigate the Fourier Transform, its inversion formula, and its basic properties. The transform analysis technique is used to reduce the complexity of the problem so to simplify the problem-solving analysis. Fourier Transform is one of such analysis technique.

2.1.1. Basics of Fourier Transform analysis

The Fourier Transform analyzes signals in the time domain, representing them in the frequency domain. It breaks down complex signals into a sum of simpler, periodic signals with various frequencies, phases, and amplitudes

$$S(f) = \int_{-\infty}^{\infty} s(t) e^{-j2\pi ft}\ dt \tag{1}$$

where s(t) is the waveform to be decomposed into a sum of sinusoids, t is the time, f is the frequency, S(f) is the Fourier Transform of s(t), and $j = \sqrt{-1}$.

The Fourier Transform provides a powerful mathematical tool for analyzing signals and understanding their frequency content. Its pictorial representation can help to visualize and understand the transformation process and the resulting frequency spectrum (Bhattacharyya and Navolio, 1976; Kitney-Hayes et al., 2014).

The Fourier Transformation is an important image-processing tool that divides an Image into sine and cosine components. The transformation's output represents the Fourier or frequency domain image, while the input image is the spatial domain counterpart *(Figure 1)*. Each point in the Fourier domain image represents a different frequency contained in the spatial domain image.

The Fourier Transform is utilized in various applications, including image analysis, image filtering, image reconstruction, and image compression (Bracewell and Bracewell, 1986; Oppenheim, 1999b). One way to understand the Fourier Transform

is through its pictorial representation. When a signal is transformed using the Fourier Transform, the resulting representation is called the frequency spectrum. The frequency spectrum can be represented graphically as a plot of amplitude versus frequency. The amplitude represents the strength of each frequency component, and the frequency represents the frequency of the signal. Another way to visualize the Fourier Transform is through its representation as a series of sine and cosine waves.

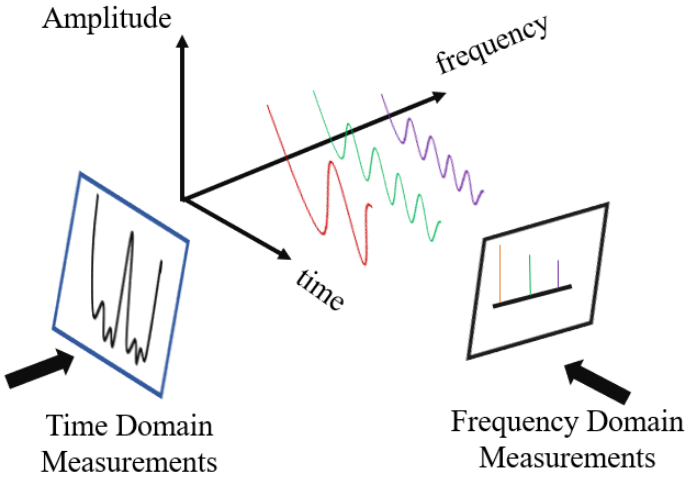

Figure 1

Fourier Transformation of the signal from time domain to frequency domain

2.1.2. Digital computer Fourier analysis

Digital computer Fourier analysis involves applying Fourier analysis algorithms on digital computers. Computational methods are used to calculate the discrete Fourier Transform for analyzing digital signals or data (Cooley and Tukey, 1965). Numerical integration of *Equation 1* implies the relationship

$$S(f_k) = \sum_{i=0}^{N-1} s(t_i)\, e^{-j2\pi f_k t_i}\, (t_{i+1} - t_i) \qquad \text{k=0, 1, …, N-1} \qquad (2)$$

where $S(f_k)$ denotes the Fourier Transform coefficient at frequency f_k, $s(t_i)$ represents the continuous-time signal sampled at N equally spaced time points t_i , k = 0, 1, ..., N-1 represents the frequency index.

Research and development in this area aimed to reduce the computational complexity and improve the performance for large-scale problems. While the computation of the DFT can be time-consuming for large N, the use of the fast Fourier Transforms algorithms (FFT), invented by Cooley and Tukey (1965), additionally to the advancements in hardware technologies can significantly mitigate this issue.

2.1.3. The inverse Fourier Transform

Mathematically, the Inverse Fourier transform can be defined as follows

$$s(t) = \int_{-\infty}^{+\infty} S(f) e^{j2\pi ft}\, df \tag{3}$$

The Inverse Fourier Transform (IFT) represent the reverses process of the Fourier Transform. It converts a frequency-domain representation of a signal back into the time-domain representation. $s(t)$ and $S(f)$ are called a Fourier transform pair, The IFT is the counterpart of the forward Fourier Transform and is often used in signal processing, image reconstruction, and various other applications. The existence of the Fourier integral is based on certain mathematical conditions. One important condition is the absolute integrability of the function $s(t)$ over its defined interval *(Equation 4)*. The function must be absolutely integrable for the Fourier integral to exist

$$\int_{-\infty}^{+\infty} |s(t)|\, dt \; < \infty \tag{4}$$

2.2. Properties of the Fourier Transform

The Fourier Transform is a powerful tool in signal processing and analysis, boasting key properties that enhance its effectiveness:

Linearity: The Fourier Transform is a linear operation. If a and b are constants, and $f(t)$ and g(t) are functions and they have the Fourier Transform $F(f)$ and $G(f)$, respectively, then $af(t) + b\, g(t)$a has a Fourier Transform $aF(f) + b\, G(f)$. $(af(t) + b\, g(t))$ and $(aF(f) + b\, G(f))$ are termed a Fourier Transform pair.

Symmetry: If $s(t)$ and $S(f)$ are a Fourier Transform, then $S(t)$ and $s(-f)$ are a Fourier Transform pair.

Time scaling: Time scaling in the Fourier Transform describes the impact of compressing or stretching a function in the time domain on its frequency domain representation (Oppenheim et al., 1997; Folland, 2009). The property states that if a function $f(t)$ is scaled by a factor α in the time domain, its Fourier Transform $F(\omega)$ will be scaled by $1/\alpha$. For a time-scaled version $g(t) = f(\alpha t)$,where α is a positive real number, the Fourier Transform $G(\omega)$ is given by this scaling relationship

$$G(\omega) = (1/|\alpha|) F(\omega/\alpha) \tag{5}$$

Frequency scaling: Frequency scaling in the Fourier Transform involves shifting the frequency components of a function in the time domain and observing the corresponding shift in the frequency domain. If a function $f(t)$ is multiplied by $e^{j\omega_0 t}$, where ω_0 is a real constant, its Fourier Transform $F(\omega)$ will be shifted by ω_0 units. For a frequency-scaled version $g(t) = e^{j\omega_0 t} f(t)$, the Fourier Transform $G(\omega)$ is given by

$$G(\omega) = F(\omega - \omega_0) \tag{6}$$

This property allows manipulation of a signal's frequency characteristics by introducing a constant frequency offset.

Alternate inversion formula: The alternate inversion formula is an alternative expression for the inverse Fourier Transform. It provides a different way to compute the time-domain function from its frequency-domain representation. The alternate inversion formula for the Fourier Transform pair $F(\omega)$ and $f(t)$ is given by

$$f(t) = \left[\int_{-\infty}^{+\infty} F^*(f)\, e^{j2\pi f t}\, df\right]^* \tag{7}$$

where $F^*(f)$ is the conjugate of $F(f)$; if $F(f) = R(f) + j\, I(f)$ then $F^*(f) = R(f) - jI(f)$.

Even functions: An even function $f(x)$ has the property $f(x) = f(-x)$ for all values of x. The Fourier Transform of an even function is real and even.

Odd function: An odd function $f(x)$ has the property $f(x) = -f(-x)$ for all values of x. The Fourier Transform of an odd function is purely imaginary and odd.

Complex time function: The Fourier Transform can be applied to complex time functions to obtain their frequency-domain representation. Understanding complex time functions and their Fourier Transforms is crucial for analyzing and manipulating signals in both the time and frequency domains. It allows for the extraction of frequency information, modulation analysis, filtering, and various other signal-processing operations.

2.3. The Fourier Series: Formulation and Diverse Applications

The Fourier series is a fundamental mathematical tool expanding periodic function, into an infinite sum of trigonometric functions like sines and cosines (Bracewell, 1986; Gray and Goodman, 2012). It elegantly approximates complex waveforms through simpler harmonic components. It extends to generalized Fourier series or transforms, representing functions as linear combinations of orthogonal basis functions, providing a versatile approach to expressing a wide range of periodic and non-periodic functions. These basis functions are typically chosen to be orthogonal where their inner products

$$(f, g) = \int_{\Omega} f(x)\, g(x)\, dx \tag{8}$$

satisfy certain properties (Elias and Stein, 2003). In the Fourier series, traditional basis functions are sine and cosine waves. However, in generalized Fourier series, various basis functions, such as Bessel functions, Legendre polynomials, and Hermite functions, can be used (Trigg, 2005; Silverman, 1972; Abramowitz and Stegun, 1968). A system of Fourier cosine functions represents a collection of cosine functions used in a Fourier series expansion. These functions are derived by taking the

real component of equivalent complex exponential functions. The general form of a Fourier cosine series for a function $f(x)$ on [a, a+2π] is as follows

$$f(x) = a_0 + 2\sum_{n=1}^{\infty} a_n \cos nx \qquad (a < x < a + 2\pi), \tag{9}$$

where a_0 and a_n called constant expansion coefficients

$$a_0 = \frac{1}{2\pi} \int_a^{a+2\pi} 1\, f(x)\, dx \tag{10}$$

$$a_n = \frac{1}{2\pi} \int_a^{a+2\pi} f(x) \cos nx\ dx\,, \qquad n = 1, 2, 3, \ldots \tag{11}$$

The Fourier sine system refers to a set of sine functions that can be used as a basis for representing functions in a Fourier series expansion (Bateman, H. and Erdélyi, A., 1954; James et al., 1996). These functions are defined by taking the imaginary part of the corresponding complex exponential functions. The Fourier sine series is defined by the following general form of the Fourier sine series

$$f(x) = 2\sum_{n=1}^{\infty} b_n \sin nx \qquad (a < x < a + 2\pi), \tag{12}$$

$where\ b_n$ constant expansion coefficients are calculated as

$$b_n = \frac{1}{2\pi} \int_a^{a+2\pi} f(x) \sin nx\ dx \qquad ,n = 1, 2, 3, \ldots \tag{13}$$

The Fourier sine system is advantageous for odd functions or those defined on an antisymmetric interval due to its focus on odd terms, aligning with the properties of sine functions. The trigonometric system, which combines Fourier sine and cosine functions, is commonly used for Fourier series expansions, accommodating both antisymmetric and symmetric functions(Bracewell, 1986; Kamen and Heck, 2006). The general form of the Fourier series using this trigonometric system is

$$f(x) = a_0 + 2\sum_{n=1}^{\infty} (a_n \cos nx + b_n \sin nx) \tag{14}$$

where

$$a_0 = \frac{1}{2\pi} \int_a^{a+2\pi} f(x)\, dx \tag{15}$$

$$a_n = \frac{1}{2\pi} \int_a^{a+2\pi} f(x) \cos nx\ dx, \qquad n = 1, 2, 3, \ldots \tag{16}$$

$$b_n = \frac{1}{2\pi} \int_a^{a+2\pi} f(x) \sin nx\ dx \qquad ,n = 1, 2, 3, \ldots \tag{17}$$

2.4. The Discrete Fourier Transform: Theory and Applications

The Discrete Fourier Transform (DFT) is crucial for analyzing discrete time domain signals, unveiling their frequency components by converting a sequence of complex numbers representing signal samples. Widely used in signal processing, the DFT helps determine frequency composition, ignores phase information, and facilitates convolution operations (Oppenheim, 1999a; Briggs and Henson, 1995). Mathematically, the DFT is formally defined as

$$DFT(X[k]) = \sum_{n=0}^{N-1}(x[n]e^{-j2\pi nk/N}) \tag{18}$$

where
$X[k]$ represents the k-th frequency component of the signal in the frequency domain,
$x[n]$ denotes the n-th sample of the discrete signal in the time domain,
j is the imaginary unit,
N is the total number of samples.

The DFT is a vital tool in digital signal processing, decomposing discrete signals to reveal their spectral content. Widely used in applications like telecommunications, audio processing, and image analysis, the DFT is integral to tasks such as image compression and enhancement (Bracewell, 1986; Bose and Meyer, 2003; Smith, 2008). Additionally, it enables fast computation through algorithms like the Fast Fourier Transform (FFT), facilitating real-time signal analysis in applications like audio processing and wireless communications (Bagchi and Mitra, 2012; Bracewell, 2004).

2.5. Continuous Fourier Transform: Theory and Applications

The Continuous Fourier Transform (CFT) is a mathematical technique used to analyze continuous, time-domain signals in terms of their frequency components

$$CFT\big(X(f)\big) = \int_{-\infty}^{\infty} x(t)\, e^{-j2\pi ft} dt \tag{19}$$

where
$X(f)$ represents the frequency component of the signal in the frequency domain,
$x(t)$ denotes the continuous signal in the time domain,
j is the imaginary unit,
f is the continuous frequency variable.

The CFT is essential for analyzing continuous time-domain signals, extending the capabilities of the Discrete Fourier Transform (DFT) to non-discretely sampled signals. Widely used in physics and quantum mechanics, the CFT provides insights into the spectral characteristics of quantum particles and various physical phenomena by revealing the frequency components of continuous signals (Lowrie, 2011).

3. BENEFITS OF FOURIER TRANSFORMATIONS AND LIMITATIONS

3.1. Advantages of Fourier Transformations

A fundamental strength of Fourier Transformations lies in their ability to decompose complex signals into their constituent frequency components. This feature is particularly advantageous when dealing with signals of diverse origins, allowing us to discern the underlying frequencies that make up these signals. This spectral decomposition serves as the foundation for many applications in signal processing and analysis. The Fourier series is a powerful tool for representing periodic signals by expressing them as combinations of sine and cosine functions. It simplifies the analysis of periodic phenomena, providing insights into harmonic content and temporal behavior, especially in fields like music, physics, and engineering (Bracewell, 1986).

In the realm of discrete signals, the DFT plays a pivotal role. Computing the DFT allows access to the frequency domain representation of discrete signals, aiding in understanding underlying frequencies and amplitudes in sampled data. This versatility makes the DFT crucial in applications from audio processing to telecommunications (Smith, 2008).

Real-world applications highlight the benefits of Fourier Transformations in signal processing, image analysis, and audio processing. These examples underscore the advantages of employing Fourier Transformations for effective signal analysis and interpretation.

3.2. Constraints of the Fourier Transformation

While Fourier Transformations offer a multitude of advantages, it is essential to acknowledge their limitations. One significant constraint pertains to the assumption of stationarity. The stationarity assumption implies that the signal's statistical properties remain constant over time (Smith, 1997) . However, many real-world signals exhibit variations in statistical properties, posing a challenge to the application of Fourier Transformations. In this context, it becomes imperative to delve into the specifics of stationarity constraints and their implications.

Another limitation concerns the sensitivity of Fourier Transformations to abrupt signal changes. When signals undergo sudden shifts or contain discontinuities, Fourier Transformations may encounter difficulties in accurately representing the signal's behavior. Addressing the challenges associated with abrupt changes in signals is essential to comprehensively understand the limitations of Fourier Transformations (Bracewell, 1986). The reduced accuracy of Fourier Transformations when applied to real-world data constitutes another critical limitation. Practical data often deviates from the idealized mathematical models assumed in Fourier analysis. As a result, the precision and the reliability of Fourier Transformations may diminish when dealing with complex, noisy, or imperfect data (Oppenheim, 1999c). Exploring the intricacies of this limitation is fundamental to grasping the practical constraints of Fourier Transformations in real-world scenarios.

In addition to theoretical constraints, practical aspects can also impose limitations on the utility of Fourier Transformations (Bracewell, 1986). Understanding the interplay between theoretical and practical constraints is vital in gaining insights into the boundaries of Fourier Transformations when applied in various domains. By comprehensively examining these limitations, we can make informed decisions about when to employ Fourier Transformations and when alternative methods may be more suitable.

4. ADDRESSING LIMITATIONS AND EXPLORING ALTERNATIVES

To address the limitations of Fourier Transformations, the exploration of alternative methods has become essential. These methods provide innovative ways to analyze signals and overcome the constraints associated with Fourier analysis. Alternative techniques often offer unique advantages in specific applications, making them valuable tools for researchers and practitioners working in signal analysis.

4.1. Wavelet Transform: Explanation and Applications

The Wavelet Transform is a mathematical technique used to analyze functions and signals by decomposing them into different scales and frequencies. Unlike the Fourier Transform, which represents a signal in the frequency domain, the Wavelet Transform simultaneously provides information in both the time and frequency domain (Mallat, 1999; Daubechies, 1992). This dual-domain analysis is one of the key advantages of wavelet analysis.

Mathematically, the continuous Wavelet Transform (CWT) of a signal x(t) is computed using the following formula

$$CWT(a,b) = \int x(t)\psi\left[\frac{(t-b)}{a}\right]dt \tag{20}$$

where
CWT (a, b) is the continuous Wavelet Transform at scale a and position b,
x(t) is the input signal in the time domain,
ψ is the complex conjugate of the mother wavelet function, which is a scaled and translated version of the mother wavelet.

The continuous Wavelet Transform examines signal x(t) at different scales (a) and positions (b), providing a time-frequency representation that's ideal for analyzing non-stationary signals. The choice of the mother wavelet function $\psi(t)$ determines the Wavelet Transform's properties, with wavelets like Morlet, Mexican hat, and Haar serving specific applications.

This versatile mathematical tool has diverse applications. In image processing, it aids in compression, denoising, and feature extraction, while data compression techniques efficiently reduce file sizes (Strang and Nguyen, 1996). In pattern recognition, particularly in computer vision and machine learning, it helps identify crucial features (Cohen, 2003). Wavelet analysis benefits biomedical signal

processing, environmental monitoring, speech and audio processing, and financial data analysis. Renowned for its adaptability and precise time-frequency information, the Wavelet Transform expands the signal analysis toolkit, offering an alternative to Fourier Transformations, especially for non-stationary signals (Mallat, 1999).

4.2. Short-Time Fourier Transform (STFT): Explanation and Applications

The Short-Time Fourier Transform (STFT) is one such alternative method that merits attention. It is designed to address a critical limitation of the standard Fourier Transform – the assumption of signal stationarity. The STFT overcomes this constraint by analyzing short, overlapping segments of a signal rather than the entire signal at once (Durak and Arikan, 2003). This approach allows for the examination of time-varying frequency components within a signal, making it particularly useful for non-stationary signals like speech, music, or any signal that changes over time

$$\mathrm{STFT(t,f)} = \int x(\tau)w(\tau t)e^{-j2\pi f\tau}d\tau \tag{21}$$

where

$\mathrm{STFT(t,f)}$ represents the Short-Time Fourier Transform at time t and frequency f,

$x(\tau)$ is the input signal in the time domain,

$w(t)$ is the window function, usually a short, localized function with non-zero values only within a limited time frame,

τ is the time variable used for shifting the window function,

t is a variable represents time,

$e^{-j2\pi f\tau}$ represents the complex exponential term for frequency f.

In the STFT, a window function slides over the signal, capturing a small portion at a time. By applying the Fourier Transform to each windowed segment, we obtain a time-frequency representation of the signal. This representation reveals how the frequency content evolves over time, providing crucial insights into transient events and non-stationary behavior. As a result, the STFT is widely used in applications like audio processing, speech recognition, and the analysis of time-varying phenomena. These are a few examples within the broader family of Fourier Transformations (These are shown in *Table 1*). The choice of which transform to use depends on the specific characteristics of the signal and the goals of the analysis.

Table 1

The system of Fourier Transformation and its characteristics, advantages, and disadvantages of some key transformations within the Fourier family

System of Fourier Transformations	Characteristics		Advantages	Disadvantages
Fourier Transform	Mathematical Representation	Continuous Domain	– Frequency Analysis. – Widespread Applicability.	– Computational Complexity – Limited for Discrete Signals
	Converts a function of time (or space) into a function of frequency. $F(\omega) = \int_{-\infty}^{\infty} f(t) \cdot e^{-j\omega t}\, dt$	Defined for continuous signals		
Discrete Fourier Transform (DFT)	Discretization	Finite-Length Signals	– Digital Implementation – Exact Representation	– Computational Complexity
	Computes the Fourier Transform for discrete signals	Suitable for processing finite-length signals		
Fast Fourier Transform (FFT)	Efficiency Improvement: An algorithmic approach to compute the DFT with reduced computational complexity.		– Efficiency – Widespread Use	– Requires Power-of-Two Lengths: Some FFT algorithms are most efficient when the signal length is a power of two.
Short-Time Fourier Transform (STFT) (Allen and Rabiner 1977; Cohen 1995)	Time-Frequency Analysis	Windowing	– Time-Frequency Localization – Adaptability: Suitable for non-stationary signals.	– Time-Frequency Resolution Tradeoff: The choice of window size affects time and frequency resolution; a smaller window provides better time resolution but poorer frequency resolution, and vice versa.
	Represents how the frequency content of a signal changes over time	Involves dividing the signal into short segments and applying Fourier Transform to each segment.		

5. EXPLORING THE PRACTICAL APPLICATIONS: TOTAL MAGNETIC FIELD ANALYSIS OF A TWO-DIMENSIONAL RIGHT RECTANGULAR PRISM AND ITS FOURIER TRANSFORM REPRESENTATION

The magnetic field of a 2D right rectangular prism, magnetized along the z-direction *(Figure 2)*, is determined using the 2D Fourier Transform. It is represented as the sum of magnetic fields from two infinite lines of dipoles (Kis, 2009). The inverse transform, employing the convolution theorem, yields a comprehensive magnetic field. The resulting expression depends on the prism's dimensions and the observation point's specific location (Griffiths and Inglefield, 2005; Jackson and Fox, 1999).

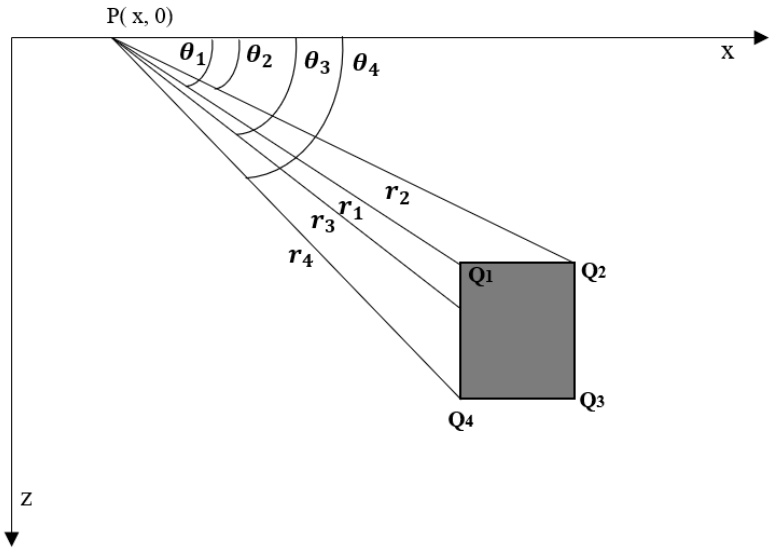

Figure 2

The location of a 2D right rectangular prism in the xz-coordinate system; the distances; r_1 , r_2, r_3, *and* r_4; *and angles* θ_1, θ_2, θ_3, *and* θ_4

The magnetic field produced by a 2D right rectangular prism *(Figure 2)* can be computed using the following analytical formula that involves the prism's dimensions and the coordinates of the observation point

$$\mathrm{T(x,z)} = -\frac{\mu_0 \mathrm{J}}{2\pi}\ (I_5 + I_6 + I_7 + I_8\ ) \tag{22}$$

where

$$I_5 = Kk\left(\tan^{-1}\frac{z-z_2}{x-x_2} - \tan^{-1}\frac{z-z_2}{x-x_1} - \tan^{-1}\frac{z-z_1}{x-x_2} + \tan^{-1}\frac{z-z_1}{x-x_1}\right) \tag{23}$$

Let us initiate the angles θ_1 , $\theta_2, \theta_3, and\ \theta_4$

$\theta_1 = \tan^{-1}\frac{z_1 - z}{x_1 - x}$, $\theta_2 = \tan^{-1}\frac{z_1 - z}{x_2 - x}$, $\theta_3 = \tan^{-1}\frac{z_2 - z}{x_2 - x}$, and $\theta_4 = \tan^{-1}\frac{z_2 - z}{x_1 - x}$

$$I_5 = Kk\,[\theta_1 - \theta_2 + \theta_3 - \theta_4]. \qquad \text{and} \qquad I_6 = Nkln\frac{r_1 r_3}{r_2 r_4}$$

With

$$r_1^2 = (x - x_1)^2 + (z - z_1)^2 \ , \ r_2^2 = (x - x_2)^2 + (z - z_1)^2,$$

$$r_3^2 = (x - x_2)^2 + (z - z_2)^2 \ , r_4^2 = (x - x_1)^2 + (z - z_2)^2 \ ,$$

$$I_7 = Knln\frac{r_1 r_3}{r_2 r_4}, \text{ and } \quad I_8 = Nn(-\theta_1 + \theta_2 - \theta_3 + \theta_4)$$

where $\mathrm{K} = \cos a \cos(A - b)$, $\mathrm{N} = \sin a$, $\mathrm{k} = \cos I \cos(A - D)$, $\mathrm{n} = \sin I$, $\mathrm{l} = \cos I \cos D$.

In the direction K, the angle A is the azimuth of the profile measured from the geographic North, a and b are the inclination and declination of the moment, respectively. The total magnetic field of a 2D right rectangular prism can be computed, given specific parameters such as the absolute value of the vector of magnetization (J), dimensions (rd), height (h), inclination of the earth's magnetic field (incl), declination of the earth's magnetic field (decl), and the position at which the magnetic field is to be calculated (x).

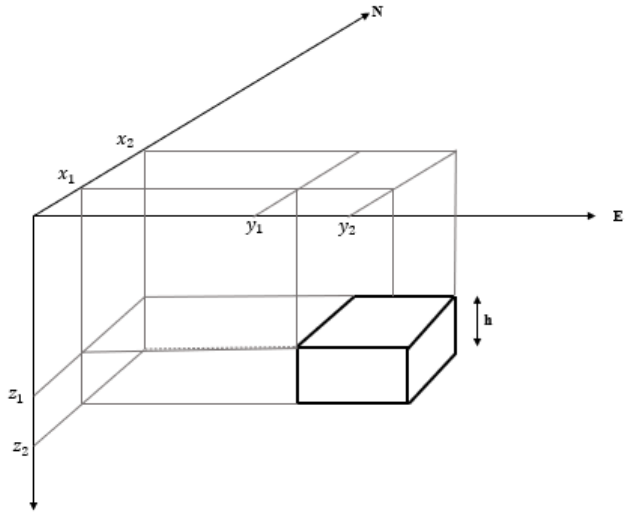

Figure 3

The position of 3D right rectangular prism in the xyz-coordinate system; the coordinates are x_1 , x_2, y_1, y_2 and z_1 and z_2

The function takes the following inputs as it is shown in the 2D and 3D representation, (*Figure 2* and *3*):
`J` is the magnetization of the prism in A/m,
`rd`is the dimensions of the prism represented as a vector [x_1, x_2, z_1, z_2], where x_1 and x_2 are the x-coordinates of the opposite corners in the x-direction, and z_1 and z_2 are the z-coordinates of the opposite corners in the z-direction,
`h`is the height of the prism in the y-direction,
`incl`is the inclination of the earth's magnetic field, provided as a vector [a, I], where 'a' is the angle of inclination in degrees from the horizontal plane, and 'I' is the angle of inclination in degrees from the northward vertical,
`decl` is the declination of the earth's magnetic field, expressed as a vector [b, D], where 'b' is the angle of declination in degrees from the geographic north to the magnetic north, and 'D' is the angle of declination in degrees from the magnetic north to the northward vertical,
`x` is the position at which the magnetic field is to be calculated, specified in the x-direction.

The function computes the magnetic field (in nT) at a specified x-position using the formula for a 2D rectangular prism, involving inclination and declination angle conversions, direction cosine calculations, and dipole moment vector components. It sums contributions from each prism side to determine the total field. The accompanying plotting script visualizes magnetic field variations for different angle configurations (D = β = 0; I = α = 0°, 30°, 60°, 90°) in *Figures 2.A.a, 2.B.d, 2.C.g,* and *2.D.j*.

Next, we introduce a Fourier Transform for the total field of a 2D right rectangular prism. The computation considers a source with a horizontal extension of 2a (symmetrical to the origin), upper and lower depths (d_1 and d_2), and uniform magnetization. The spatial frequency 'f' (in cycles per spatial unit) is used. The given equation yields result for z = 0 and f < 0

$$T(f) = \mu_0 J\, a\, sinc(2fa)\Big((Kk - Nn)\big(e^{-2\pi|f|d_2} - e^{-2\pi|f|d_1}\big) + j\,(Kn + Nk)\big(e^{-2\pi|f|d_2} - e^{-2\pi|f|d_1}\big)\Big)$$

For z = 0 and f > 0

$$T(f) = \mu_0 J\, a\, \mathrm{sinc}(2\mathrm{fa})\Big((Kk - Nn)\big(e^{-2\pi|f|d_2} - e^{-2\pi|f|d_1}\big) + j\,(Kn + Nk)\big(-e^{-2\pi|f|d_2} + e^{-2\pi|f|d_1}\big)\Big)$$

With a thickness t($t = d_2 – d_1$) the Fourier Transform of the total magnetic field of the 2D right rectangular prism is

$$T(f) = \mu_0 J\, a\, \mathrm{sinc}(2\mathrm{fa})\, e^{-2\pi|f|d_1}(e^{-2\pi|f|t} - 1)((Kk - Nn) - jsign(f)(Kn + Nk)$$

Figures 2 illustrates the real and imaginary parts of the spectrum of the total magnetic field of the 2D right rectangular prism. These functions are plotted with respect to the spatial frequency 'f', and the sampling interval is determined by the upper depth 'd1' (set at 1 km) and the horizontal extension '2a' (equal to 6 km), where 't' is 1 km. *Figures* (*4.A.b* and *4.A.c*), (*4.B.e* and *4.B.f*), (*4.C.h* and *4.C.i*), and (*4.D.k* and *4.D.l*) are generated for D = β = 0; I = α = 0°, 30°, 60°, 90°, respectively.

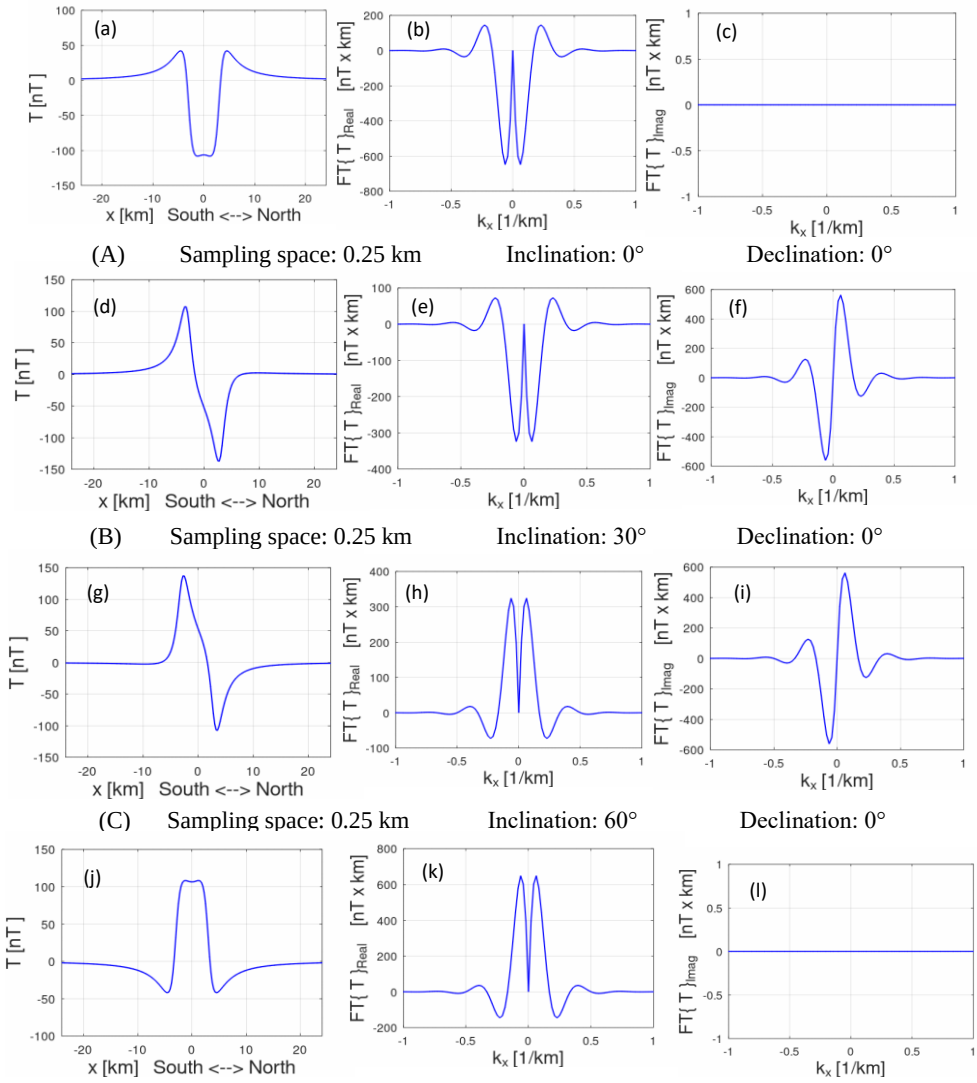

(A) Sampling space: 0.25 km Inclination: 0° Declination: 0°

(B) Sampling space: 0.25 km Inclination: 30° Declination: 0°

(C) Sampling space: 0.25 km Inclination: 60° Declination: 0°

(D) Sampling space: 0.25 km Inclination: 90° Declination: 0°

Figure 4

The total magnetic field of a 2D right rectangular prism with its Fourier Transforms representation

6. Conclusions

In conclusion, this paper has provided a comprehensive exploration of the historical significance, theoretical foundations, virtues, and limitations of Fourier Transformations. For professionals in diverse fields, understanding these aspects is essential for informed decision-making in signal analysis. We introduced alternative methods like the Wavelet Transform and Short-Time Fourier Transform, offering a comparative analysis for method selection. As technology advances, ongoing research into innovative methods and interdisciplinary approaches is crucial to address challenges in non-ideal scenarios and real-world data. Embracing a forward-looking perspective will contribute to the continuous advancement of signal analysis.

Acknowledgments

The author extends gratitude to the Stipendium Hungaricum scholarship for enabling their PhD studies in Hungary. Special thanks to prof. dr. Endre Turai and Dr. Péter Tamás Vass for their support. Appreciation is also conveyed to the Mikoviny Sámuel Doctoral School of Earth Sciences and the Department of Geophysics at the University of Miskolc for providing a valuable opportunity and an enriching research environment.

References

Abramowitz, M., Stegun, I. A. (1968). *Handbook of Mathematical Functions with Formulas, Graphs, and Mathematical Tables.* U.S. Government Printing Office.

Allen, J. B., Rabiner, L. R. (1977). A unified approach to short-time Fourier analysis and synthesis. *Proceedings of the IEEE*, 65, pp. 1558–1564.

Bagchi, S., Mitra, S. K. (2012). *The nonuniform discrete Fourier transform and its applications in signal processing.* Springer Science & Business Media.

Baron Fourier, J. B. J. (2003). *The analytical theory of heat.* Courier Corporation.

Bateman, H. and Erdélyi, A. (1954). Tables of Integral Transforms.

Bhattacharyya, B. K., Navolio, M. E. (1976). A Fast Fourier Transform method for rapid computation of gravity and magnetic anomalies due to arbitrary bodies*. *Geophys. Prospect.*, 24, pp. 633–649. https://doi.org/10.1111/j.1365-2478.1976.tb01562.x

Bose, T., Meyer, F., (2003). *Digital signal and image processing.* John Wiley & Sons, Inc.

Bracewell, R. (2004). *Fourier analysis and imaging.* Springer Science & Business Media.

Bracewell, R. N. (1986). *The Fourier Transform and Its Applications.* NY, McGraw-Hill.

Briggs, W. L., Henson, V. E. (1995). The DFT: An Owner's Manual for the Discrete Fourier Transform. *Society for Industrial and Applied Mathematics*. https://doi.org/10.1137/1.9781611971514

Cohen, A. (2003). *Numerical analysis of wavelet methods.* Elsevier.

Cohen, L. (1995). *Time-frequency analysis.* Prentice hall New Jersey.

Cooley, J. W., Tukey, J. W. (1965). An algorithm for the machine calculation of complex Fourier series. *Mathematics of Computation*, 19, pp. 297–301.

Daubechies, I. (1992). Ten Lectures on Wavelets. *Society for Industrial and Applied Mathematics*. https://doi.org/10.1137/1.9781611970104

Durak, L., Arikan, O. (2003). Short-time Fourier transform: two fundamental properties and an optimal implementation. *IEEE Transactions on Signal Processing*, 51, pp. 1231–1242.

Elias, M., Stein, R. S. (2003). *Fourier analysis: An introduction.*

Folland, G. B. (2009). *Fourier analysis and its applications.* American Mathematical Soc.

Gray, R. M., Goodman, J. W. (2012). *Fourier transforms: an introduction for engineers.* Springer Science & Business Media.

Griffiths, D. J., Inglefield, C. (2005). Introduction to Electrodynamics. *American Journal of Physics*, 73, pp. 574–574. https://doi.org/10.1119/1.4766311

Jackson, J. D., Fox, R. F. (1999). Classical Electrodynamics. 3rd ed. *American Journal of Physics*, 67, pp. 841–842. https://doi.org/10.1119/1.19136

James, J. F., Enzweiler, R. N., McKay, S., Christian, W. (1996). A student's guide to Fourier transforms with applications in physics and engineering. *Computers in Physics*, 10, pp. 47–47.

Kamen, E. W., Heck, B. S. (2006). *Fundamentals of signals and systems using the web and matlab.* Prentice-Hall, Inc.

Kis, K. (2009). *Magnetic methods of applied geophysics.* Eötvös University Press.

Kitney-Hayes, K. A., Ferro, A. A., Tiwari, V., Jonas, D. M. (2014). Two-dimensional Fourier transform electronic spectroscopy at a conical intersection. *The Journal of Chemical Physics*, 140, 124312. https://doi.org/10.1063/1.4867996

Lowrie, W. (2011). *A student's guide to geophysical equations.* Cambridge University Press.

Mallat, S. (1999). *A wavelet tour of signal processing.* Elsevier.

Oppenheim, A. V. (1999a). *Discrete-time signal processing.* Pearson Education India.

Oppenheim, A. V. (1999b). *Discrete-time signal processing.* Pearson Education India.

Oppenheim, A. V. (1999c). *Discrete-time signal processing.* Pearson Education India.

Oppenheim, A. V., Willsky, A. S., Nawab, S. H., Ding, J.-J. (1997). *Signals and systems.* Prentice Hall Upper Saddle River, NJ.

Silverman, R. A. (1972). *Special functions and their applications.* Courier Corporation.

Smith, J. O. (2008). *Mathematics of the discrete Fourier transform (DFT): with audio applications.* Julius Smith.

Smith, S. W. (1997). *The scientist and engineer's guide to digital signal processing.*

Strang, G., Nguyen, T. (1996). Wavelets and filter banks. SIAM.

Trigg, G. L. (ed.) (2005). *Mathematical Tools for Physicists.* 1st ed. Wiley. https://doi.org/10.1002/3527607773

Geosciences and Engineering, Vol. 12, No. 1 (2024), pp. 75–87.
https://doi.org/10.33030/geosciences.2024.01.005

EXPLORING UNCERTAINTY IN FLOW UNIT IDENTIFICATION AND PERMEABILITY PREDICTION

FRANKLIN GÓMEZ[1*], MARIANNA VADÁSZI[2]
[1*]*Institute of Mining and Energy, University of Miskolc, Hungary;*
gomez.soto.franklin.vinicio@student.uni-miskolc.hu
[1*]*Petroleum Department, Faculty of Geology and Petroleum Engineering, Escuela Politécnica Nacional, Ecuador*
[2]*Institute of Mining and Energy, University of Miskolc, Hungary;*
marianna.vadaszi@uni-miskolc.hu
[1]*https://orcid.org/0000-0003-4367-4972*
[2]*https://orcid.org/0000-0003-0649-311X*

Abstract: The study proposes a comparative uncertainty analysis of the main methods for permeability prediction or estimation, including the Cluster analysis (K-means), the Kozeny-Carman (KyC) equation for flow unit identification, and the K-nearest neighbor Density Estimate (KNN) algorithm, Kozeny-Carman equation, and One Flow Unit (OFU) for permeability prediction or estimation. The proposed analysis is applied to 13 wells in the Sacha field located in the Amazon region of Ecuador, targeting the Hollin and Napo formations, which mainly consist of sandstone, limestone, and shale. The selected wells have a sufficient number of laboratory measurements of permeability and electrical logs of porosity, permeability, natural gamma ray, medium, and deep resistivity. Initially, the K-means clustering and KyC methods are applied to identify the flow units, followed by a regression process to calculate the permeability using the KNN, KyC, and OFU methods. During the clustering process, the KyC method yielded better results, with the experimental data exhibiting uncertainties of less than ±35 mD, except in the outlier flow unit with an average porosity of 16.86% ±3.87% (Flow Unit D) whose average permeability is 407.52 mD and uncertainty of ±504.10 mD. For software simulation purposes, it is recommended to utilize the KyC method, as it employs basic concepts and equations in accordance with hydraulic principles.

Keywords: *uncertainty, permeability prediction, Sacha, flow units, K-nearest neighbor density estimate algorithm, cluster analysis*

1. INTRODUCTION

The process of modeling an underground reservoir requires the permeability property determination, but this property can be measured by pressure test or directly by core samples (Remeczki et al., 2020, Fanchi, 2018). This determination of the permeability is only developed in small portions of the reservoir. Therefore, the prediction process of the permeability is essential. The results obtained from permeability values vary widely between the laboratory data and the predictions of the different methods, however these predictions are used for modeling. Why are these values used in modeling despite their relatively wide difference? What is the method that

provides the best results? It is very important to know the uncertainties involved in each of the values of the methods used to predict permeability, since in this way the most appropriate method can be used.

The uncertainty in any measurement process has three components (Berg et al., 2021): the variation between the sample and the same rock type with heterogeneity, experimental uncertainty during the measurement, and the interpretation process related to the model application. Few research evaluates and gives directly the values of permeability (Johnston and Beeson, 1944) or others evaluate the uncertainty of the relative permeability (Berg et al., 2021, Mathias et al., 2013) but not the sample data permeability.

Normally, laboratory measurements are not carried out in all wells and at all depths, so it is decided to use well logs to obtain permeability values and identify flow units through different processes. In some cases, the Kozeny-Carman equation is used to discretize the porosity values and based on a certain number of laboratory measurements of permeability, identify the flow units, and obtain the permeability by regression for the other zones and wells. For instance, (Belhouchet and Benzagouta, 2019) use the Kozeny–Carman equation with the DRT (Discrete Rock Typing method) for predict the permeability in Algerian B-H oil field reservoir. This reservoir is composed of sandstone, limestone and dolomites and the results are based in the Correlation Coefficient R to determine if the estimation is right or wrong. However, they never expo the data of the permeability regression. Abbaszadeh et al. (1996), Amaefule et al. (1993) and Perez et al. (2005) use the same equations with different variations but with the main similar idea.

On the other side, Aminian et al. (2003) proposes the use of neural networks to base on training data predict the permeability and identify the flow units. It is similar to using the K-nearest-neighbor Density Estimate (KNN) which needs training data. In the case of study of the Norcan East Field (Bhattacharya et al., 2008) the methodology offers a complete process which includes validation based on the water saturation and capillary pressure which appear in the transition's zones. This methodology is more complete but never calculates the uncertainty of the permeability values. Data from 13 wells were used in this research, which are in total 428 samples measured its porosity and permeability. Three methods are proposed to identify the flow units, one based in the size of porous that we call Kozeny–Carman (KyC) method, other is the cluster analysis algorithm called K-means which identified centroids and classified the data according to the nearest points [Szabó et al. (2019), Ali, Sheng-Chang (2020)]. In addition to, on this research the called One Flow Unit (OFU) method which as its name implies all the data belongs to one flow unit, it is because in the process of modeling it is always used and certainly sometimes It gets the best history match with the real fluid production (Krause et al., 2009).

Permeability was estimated using the Kozeny–Carman equations with DRT (Discrete Rock Typing) (Belhouchet and Benzagouta, 2019; Amaefule et al., 1993) but also uses the K-nearest-neighbor Density Estimate (KNN) method (Gómez et al., 2022) which is based on a test data for learning and estimate the permeability. The third method uses exponential matching in One Flow Unit (OFU).

In addition, the uncertainty for the real sample data is determined with *Equations (14), (15)* and *(16)*. And for the estimation of the permeability the equation used will be determined with exponential matching (Papadopoulos and Yeung, 2001). However, the calculation of the error develops using the *Equation (17)*. The results show that the error and the uncertainty do not have any similarity and the uncertainty is always present.

2. METHODOLOGY

Permeability and porosity data are measured on 428 samples obtained from 13 wells in the Sacha field located in northeastern Ecuador (Baby et al., 2014). This data was matched with the well logs of natural gamma ray, superficial, intermediate, and deep resistivity, neutron porosity, gamma-gamma density and spontaneous potential. The methodology is divided into three stages:

- Flow unit identification,
- Permeability estimation,
- Uncertainty and error of permeability determination.

2.1. Flow Unit Identification

Using the Kozeny-Carman methodology four flow units were identified: A, B, C and D. The equations used are (Amaefule et al. 1993):

$$\theta_z = \frac{\theta}{1-\theta} \tag{1}$$

$$RQI = 0.0314\frac{K}{\theta} \tag{2}$$

$$FZI = \frac{RQI}{\theta_Z} \tag{3}$$

$$DRT = 2Log_eFZI + C \tag{4}$$

where Θ_z is normalized porosity in volume fraction, RQI is Rock quality index, K is permeability in mD, Θ is porosity in volume fraction, FZI is Flow zone indicator, DRT is Discrete rock typing. According to the theory in a graphic Log RQI vs Log Θ_z must draw parallels lines to differentiate the flow units (see *Figure 1*).

Discrete rock typing (DRT) gives integer numbers, in this case ranging from 6 to 27, and they are organized into larger groups called flow units. In this case, using MATLAB, the grouping of the values was easier because the parallel lines in *Figure 1* must have the same slope and the numbers are in order. In Table 1 are the numbers that are related to the flow units A, B, C, D.

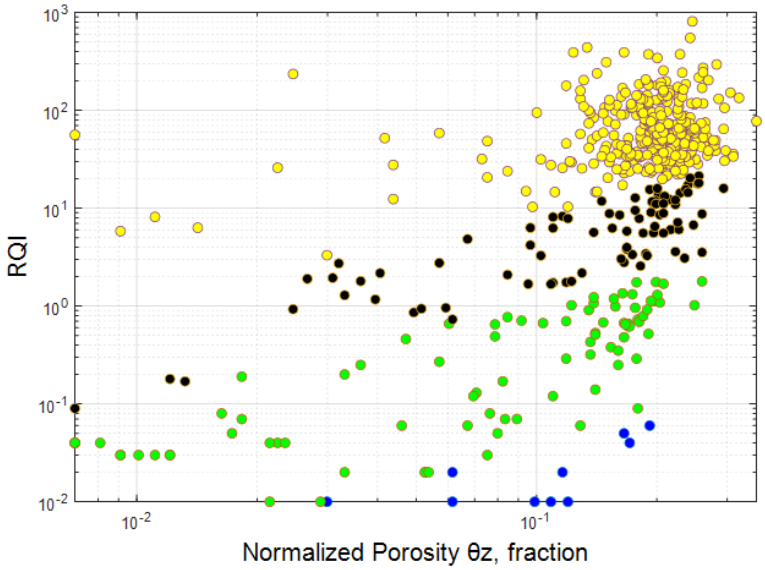

Figure 1

Log RQI vs log Θz of 428 samples of the Sacha Field. Blue, green, black and yellow represent the corresponding flow units A, B, C, D identified

The other method used to identify the flow units was using the Cluster Analysis methodology. K-means cluster analysis is a simple unsupervised statistical method that orders the objects of a multivariate dataset into groups (flow units) using the information of similarities given by metric distance (see *Figure 2*). The method is sensitive to the scale difference between variables, so normalization of the data set is required. Then, each object is designated into a non-overlapping group of great homogeneity and large differences from other groups. For further explanation see Szabó et al. (2019) and Ali and Sheng-Chang (2020). Mathematically, the method is expressed by the following equation:

$$J = \sum_{j=1}^{k} \sum_{i=i}^{n} \left\| x_i^{(j)} - c_j \right\|^2 \tag{5}$$

where J is objective function, x_i is the i-th analyzed object, i= 1,…, n, c_j is the j-th cluster centroid, j= 1,.., k, K is optimal number of clusters. The objective function converges at the minimum sums of square deviation of objects x_i, from the cluster centroid c_j.

The "City Block" distance metric is incorporated for this study. Here, each cluster centroid is the component-wise median of the points in the cluster

$$D_1 = \sum_{k=1}^{N} \left| x_k^{(i)} - x_k^{(j)} \right| \tag{6}$$

where D is sum of lengths between points, $x_k^{(i)}$ is distance of x_k from the centroid in component i, $x_k^{(j)}$ is distance of x_k from the centroid in component j. In this case, the four flow units identified were named 1, 2, 3 and 4. The data classification can be seen on *Figure 2*:

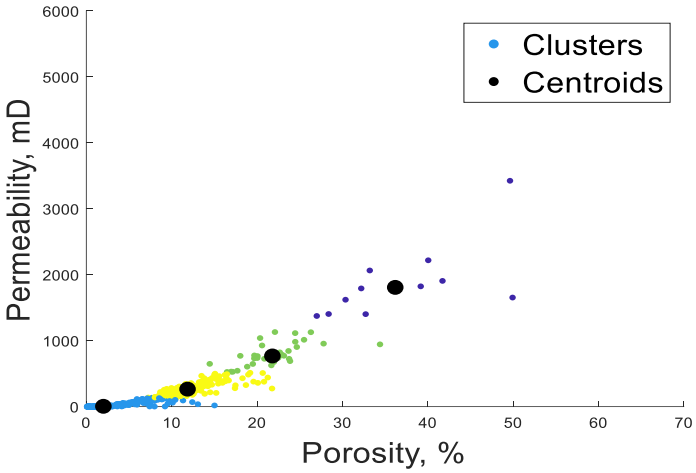

Figure 2

Permeability and porosity of 428 samples classified by K-means clustering algorithm. Light blue, yellow, green, and purple are the flow units 1, 2, 3, and 4 respectively. Black points are the centroids

Finally, the One Flow Unit (OFU) method to complete permeability data is presented in *Figure 3*.

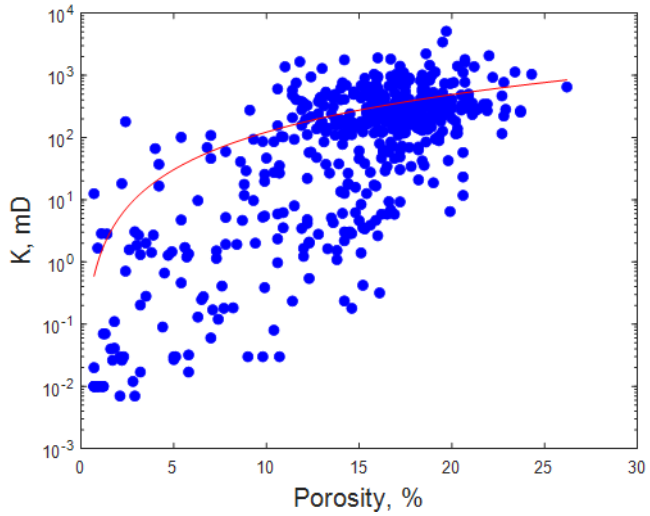

Figure 3

Logarithm of permeability vs. porosity (%) of the 428 samples.
Red line represents the exponential regression to predict the permeability

2.2. Permeability estimation

The permeability was estimated first using an exponential regression for each flow unit A, B, C and D. The empirical equations are given below

$$K_A = 4.804 * 10^{-6}\theta^{3.994} \tag{7}$$

$$K_B = 0.00179\theta^{2.862} \tag{8}$$

$$K_C = 0.01604\theta^{2.849} \tag{9}$$

$$K_D = 1.521\theta^{1.959} \tag{10}$$

The second method used for estimating the permeability was the K-nearest neighbor density estimate (KNN) which is a non-parametric method of estimating a probability density function. The algorithm estimates a function that predicts the rock type(z) according to the log-well registered values. Every interpreted rock category x is a p-dimensional random variable X. This means the interpretation of the rock permeability will depend on the pre-established rock type z. The d(x,z) represents the Euclidean distance between x and z. X is an example of z, consequently x is the permeability measured and matched with the logs before the prediction (Hu et al., 2008, Mitra et al., 2002). The hypersphere of radius r about z is designated by *Equation 11*

$$A_{r,z} = \{X \setminus d(x,z) \leq r\} \tag{11}$$

where $A_{r,z}$ is volume of the hypersphere, r is radius of the hypersphere, x isa categorical class, and X is a variable with p dimensions. Then *Equation 12* defines the density function:

$$f_N(z) = \frac{k(N)}{N} * \frac{1}{A_{rk(N),z}} \tag{12}$$

where $f_N(z)$ is a function f to estimate z with N, k(N) is a sequence of positive integers from x_1 to x_N, x is a rock type interpreted in a set of data. By the other hand, the OFU method determine the exponential equation. See *Figure 3*:

$$K_T = 0.9733\theta^{2.825} \tag{13}$$

2.3. Uncertainty and error of permeability determination

Here, the real sample data was measured in poropermeameter equipment whose precision is 0.1% for the porosity and 0.01 mD for the permeability. The process of divide the permeability in flow units suppose that in the modeling process the same equation will be used for all the data that belongs to this flow unit. It is similar to the up-scaling where a group of data of wells is assigned to a cell of a grid. For this reason, the *Equation 14* is used for determining the uncertainty in the experimental data. The *Equation 15* is used to determine the uncertainty when a regression process

is developed. The *Equation 16* is the porosity uncertainty necessary for the calculation of the permeability uncertainty (JCGM member organizations, 2008)

$$u(k) = \sqrt[2]{P_K^2 + S_K^2} \tag{14}$$

$$u(k) = \frac{\partial K}{\partial \theta} u(\theta) \tag{15}$$

$$u(\theta) = \sqrt[2]{P_\theta^2 + S_\theta^2} \tag{16}$$

where u is the uncertainty of the permeability and porosity, P is a precision of the poropermeameter equipment for permeability and porosity, S is the Standard Deviation for porosity and permeability. The calculation of the error was also developed using the equation:

$$\%E = \frac{RV - EV}{RV} * 100 \tag{17}$$

where %E is the data estimation Error with respect to the sample measured, RV is the real value with refer to the sample measured, and EV is the estimated value with the different proposed methods.

3. RESULTS

The results of the flow units and the permeability estimation according the KyC methodology is presented on the *Figure 4*, *Table 1* and *Table 2*. The θ_{mean} is the mean porosity in the flow unit, k_corr is the measured permeability, K_NN is the permeability estimated using the KNN method, E_KNN is the error between the measured and the estimated permeability, K_KyC is the permeability in the flow unit and E_KyC is the error. In the calculation of the errors the equation used was *Equation 17*.

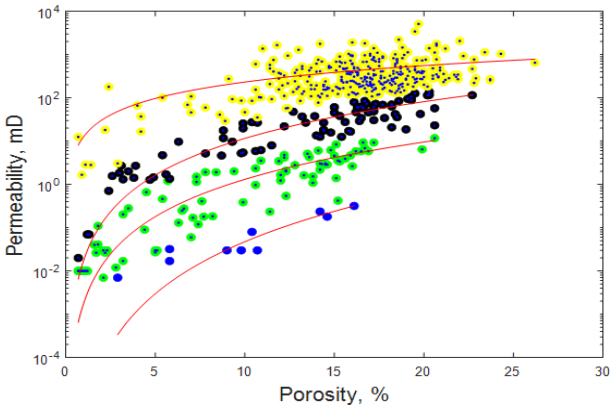

Figure 4

Logarithm of permeability vs. porosity (%) of the 428 samples divided in four flow units. Red lines represent the exponential regression to predict the permeability

Table 1

Flow units A, B, C, and D determined using the KyC method with the DRT (discrete rock typing) with porosity (Θ_{mean}), permeability (k_corr) measured in laboratory, and permeability calculated with KNN(K_{NN}) and KyC (K_KyC)

DRT	FLOW UNIT	NUMBER ELEMENTS	Θ_{mean} %	k_corr mD	K_NN mD	E_KNN	K_KyC mD	E_KyC
6	A	3.00	9.83	0.03	0.03	0.00%	0.07	131.88%
7		2.00	8.10	0.05	0.05	0.00%	0.05	4.28%
8		5.00	10.72	0.15	0.15	0.00%	0.28	81.82%
9	B	8.00	6.70	0.10	0.10	0.00%	1.36	1220.58%
10		5.00	6.56	0.13	0.13	0.00%	0.58	356.38%
11		5.00	9.50	0.46	0.46	0.00%	2.18	377.81%
12		13.00	7.27	0.60	0.60	0.00%	1.79	198.15%
13		19.00	10.35	2.04	2.04	0.00%	4.44	117.34%
14		21.00	9.50	2.88	2.88	0.00%	4.15	43.97%
15		15.00	10.81	4.28	4.28	0.00%	3.67	14.29%
16	C	21.00	10.41	8.42	8.42	0.03%	38.74	360.08%
17		11.00	14.59	23.46	19.83	15.46%	69.42	195.93%
18		16.00	13.09	30.12	30.12	0.00%	58.20	93.23%
19		33.00	14.78	62.62	62.62	0.00%	79.05	26.25%
20	D	41.00	16.95	142.72	141.69	0.72%	616.22	331.77%
21		79.00	17.69	230.72	227.98	1.19%	647.59	180.68%
22		66.00	16.91	327.78	327.78	0.00%	585.22	78.54%
23		29.00	16.39	551.21	545.49	1.04%	588.57	6.78%
24		26.00	15.07	770.47	770.47	0.00%	514.63	33.21%
25		6.00	14.85	1412.19	1412.19	0.00%	525.87	62.76%
26		2.00	17.75	2665.86	2665.86	0.00%	636.04	76.14%
27		2.00	15.75	3377.07	3377.07	0.00%	523.76	84.49%

In *Table 2* $u_{R\theta}$ is the porosity uncertainty in % determined using *Equation 16*, u_{RK} is the uncertainty in the permeability determined using *Equation 14* with the S_k of each flow unit of KyC, u_{KNN} is the uncertainty in the KNN permeability determined with *Equation 14* and the $u_{R\theta}$ for each KyC flow unit, U_{CK} is the uncertainty in the KyC permeability determined with *Equation 15* and $u_{R\theta}$ for each KyC flow unit.

Table 2

Uncertainty and Error values in the KyC method for flow units ($u_{R\Theta}$ Equation 16, u_{RK} Equation 14, U_{KNN} Equation 14, u_{CK} Equation 15 and 16) in KNN and KyC methods for permeability estimation

FLOW UNIT	# SAMPLES	Θ_{mean} %	$u_{R\Theta}$ %	K_R mD	u_{RK} mD	KNN _mD	U_{KNN} mD	E_KNN	K_kyC_mD	u_{CK} mD	E_KC
A	10	9.93	±4.26	0.10	±0.11	0.10	±0.15	0.00%	0.17	±0.08	77.81%
B	86	9.15	±5.65	2.04	±2.56	2.04	±2.56	0.00%	3.19	±1.78	56.77%
C	81	13.29	±5.66	36.83	±34.74	36.34	±34.94	1.34%	63.17	±30.90	71.54%
D	251	16.86	±3.87	407.52	±504.10	405.83	±504.68	0.42%	601.49	±173.21	47.60%

Table 3 presents the flow units according the K-means clustering method: $u_{R\theta}$ is the porosity uncertainty in % determined using *Equation 16*, u_{RK} is the uncertainty in the permeability determined using *Equation 14* with the Sk of each flow unit of K-means, u_{KNN} is the uncertainty in the KNN permeability determined with *Equation 14* and the $u_{R\theta}$ for each K-means flow unit, U_{KyC} is the uncertainty in the KyC permeability determined with *Equation 15* and $u_{R\theta}$ for each K-means flow unit.

Table 3

Uncertainty and error values in the K-means clustering method for flow units ($u_{R\Theta}$ Equation 16, U_{RK} Equation 14, U_{KNN} Equation 14, U_{KyC} Equation 15 and 16) in KNN and KyC methods for permeability estimation

FLOW UNIT	# SAMPLES	Θ_{mean} %	$u_{R\Theta}$ %	K_R mD	U_{RK} mD	KNN_mD	U_{KNN} mD	EKNN	KkyC Md	U_{KyC} mD	EKyC
	173	14.98	±4.98	233.03	±514.99	231.55	±515.26	0.64%	368.43	±38.31	58.10%
	79	13.00	±6.57	199.37	±270.59	198.83	±270.69	0.27%	287.29	±31.07	44.10%
	134	15.20	±4.93	254.43	±341.91	254.43	±341.91	0.00%	396.75	±59.86	55.94%
	42	12.80	±7.16	364.01	±535.80	360.05	±535.90	0.01	399.22	±435.10	9.67%

In *Table 4* we present the uncertainty and error with One Flow Unit method.

Table 4

Uncertainty and Error values in the OFU method for permeability estimation

K_OFU mD	u_{UFO} mD	E_KOFU
438.70	±349.59	78.73%

4. DISCUSSION

Unquestionably in this case, the KNN method gives the best result taking account the %Error (E_KNN) (*Table 1* and *2*) for both grouping methods, it attributes because KNN uses test data for estimate the permeability. If the permeability property is needed the KNN is the best option. However, it recommends using KyC method in modeling process. For modeling the up scaling Fanchi (2018) means grouping permeability for assign values or equations to a complete cell or cells. In his publication, Wang (2018) arrives at a similar conclusion regarding the identification of flow units for lithological purposes. In this work, Wang writes, "KNN (K-Nearest Neighbors) clustering in machine learning is a very efficient clustering method applied in lithology identification, reservoir type recognition, flow unit classification, and so on. However, it is not consistently effective due to its inherent limitations, such as its initial center selection and clustering center shift caused by outliers." Wang states that while the KNN method is generally efficient, it encounters problems with clustering, which he attributes to issues with the initial selection center (Wang et al., 2018). In the publication by Silva (2019) titled Petrofacies Classification using Machine Learning Algorithms, the precision for predicting petrofacies using KNN is 92% for homogeneous layers, while for heterogeneous layers, it is reduced to 85%. In this research, they utilize an 80/20 split, meaning 20% of the data

is used for testing, and 80% is for evaluation. The challenge in petrofacies identification lies in classifying heterogeneous layers. Permeability is a crucial aspect of petrofacies. This confirms the assertion because the data grouping directly addresses the heterogeneity of layers (Silva et al., 2020).

In this investigation % Error is calculated by comparing the measured data with the estimated data, and it is an individual comparison between two values, while the uncertainty first depends on the precision of measuring equipment and after of the clustering process. The standard deviation is an important part of the determination of uncertainty.

In the application of the KyC for identifying flow units, the suitable value of porosity varies from 9.15 ±5.65% to 16.86 ±3.87%. While the experimental data of permeability has a suitable value from 0.1 ±0.11 mD to 407.52 ±504.10 mD. Like, the estimated permeability varies from 0.10 ±0.15 mD to 405.83 ±504.68 mD with the KNN method. Comparable, in the KyC method the permeability varies from 0.17 ±0.08 mD to 601.49 ±173.21 mD. Certainly, the permeability has a huge uncertainty, and it increases when is tried to estimate with different methods.

By the other hand, in the application of the K-means method for identify flow units the suitable value of porosity varies from 12.80 ±7.16% to 15.20 ±4.93%. While the experimental data of permeability has a suitable value from 199.37 ±270.59 mD to 364.01 ±535.80 mD. Like, the estimated permeability varies from 198.83 ±270.69 mD to 360.05 ±535.90 mD with the KNN method. Comparable, in the KyC method the permeability varies from 287.29 ±31.07 mD to 399.22 ±435.10 mD. Here, the uncertainty is less in the KyC method than the KNN method. However, the % Error is higher for every mean permeability. Consequently, the KNN is better in individual analysis but in grouped data the KNN has higher uncertainty.

In the application of the OFU method for identifying flow units the suitable value of permeability is 438.70 ±349.59 mD with an error of 78.73%. If we compare this value with the other methods this value still inside the limits of the permeability measured or estimated for them. It means that the use of one flow unit in modeling is not a bad option considering that the uncertainty of permeability with the other methods has a huge variation.

5. CONCLUSIONS

According to our study, the best method to use in modeling process is KyC for flow units identification and permeability estimation. The uncertainty in *Table 2* and *3*, u_{KNN} (uncertainty in KNN method) and u_{CK} (uncertainty in method KyC) show smaller values in KyC method. The best method for determining the permeability is the KNN because the error is almost zero in all the flow unit classifications.

The flow unit D has uncertainty higher than the estimated value except in the KyC method, it is because the D flow unit is the one with bigger porous size and permeability measures. The KyC method always uses the size of the porous to grouping the data.

The KyC method uses the size of the porous-like base for dividing the data while K-means uses only mathematics for dividing. However, using K-means is disquieting to clustering the data of natural gamma ray or resistivity logs to identify some match with the groups of permeability with porosity. If a good correlation is found, is possible to develop equations for predicting permeability with log data. Certainly, it is recommended to use K-means in K vs. natural gamma ray or K vs. Resistivity or K vs. density and compare with K-means of K vs. porosity.

ACKNOWLEDGMENTS

The author, Franklin Gómez, would like to express his deepest gratitude to National Polytechnic School of Ecuador for their sponsorship and support as he embarks on his doctoral studies at the University of Miskolc. Furthermore, Franklin would like to extend his appreciation to the University of Miskolc and the Hungarian people who contribute their taxes to make the Hungarian Stipendium scholarship possible. Lastly, Franklin would like to thank Pierre Kuhmmert and E.P. Petroecuador for their collaboration in sharing valuable data. The methodology of the research was made in the frame of Project no. RRF-2.3.1-21-2022-00009, titled National Laboratory for Renewable Energy has been implemented with the support provided by the Recovery and Resilience Facility of the European Union within the framework of Program Széchenyi Plan Plus. The simulation process and the results were funded by the Sustainable Development and Technologies National Program of the Hungarian Academy of Sciences.

REFERENCES

Abbaszadeh, M., Fujii, H., Fujimoto, F. (1996). Permeability prediction by hydraulic flow units theory and applications. *Society of Petroleum Engineers*, 11 (4), pp. 263–271. Retrieved from https://doi.org/10.2118/30158-PA

Ali, A., Sheng-Chang, C. (2020). Characterization of well logs using k-mean cluster analysis. *Journal of Petroleum Exploration and Production Technology*, 10 (6), pp. 2245–2256. Retrieved from https://doi.org/10.1007/s13202-020-00895-4

Amaefule, J. O., Altunbay, M., Tiab, D., Kersey, D. G., Keelan, D. K. (1993). Enhaced reservoir description: using core and log data to identify hydraulic(flow) units and predict permeability in uncored intervals/wells. *Software: Practice and Experience*. pp. 205–220. Retrieved from https://api.semanticscholar.org/CorpusID:54908443.

Aminian, K., Ameri, S., Oyerokun, A., Thomas, B. (2003). Prediction of flow units and permeability using an artificial neural networks. *SPE West. Reg. Pacific Sect.*, pp. 299–305. Retrieved from https://api.semanticscholar.org/CorpusID:140543065.

Baby, P., Rivadeneira, M., Roberto, B. (2014). *La cuenca oriente: geologia y petroleo*. Institut français d'études andines.
Retrieved from https://doi.org/10.4000/books.ifea.2984

Belhouchet, H. E., Benzagouta, M. E. (2019). Rock typing: reservoir permeability calculations using discrete rock typing methods (DRT): case study from the Algerian B-H oil field reservoir. *Advances in Petroleum Engineering and Petroleum Geochemistry*. Retrieved from https://api.semanticscholar.org/CorpusID:134624668.

Berg, S., Unsal, E., Dijk, H. (2021). Non-uniqueness and uncertainty quatification of relative permeability measurements by inverse modelling. *Computers and Geotechnics*, 132. Retrieved from https://doi.org/10.1016/j.compgeo.2020.103964

Bhattacharya, S., Byrnes, A. P., Watney, W. L., Doveton, J. H. (2008). Flow unit modeling and fine-scale predicted permeability validation in Atokan sandstones: Norcan East Kansas. *AAPG Bulletin*, 92 (6), pp. 709–732. Retrieved from https://doi.org/10.1306/01140807081

Fanchi, J. R. (2018). *Principles of Simulation.* Fourth ed. Texas, Elsevier.

Gómez, F. V., Flores, Y., Vadászi, M. (2022). Comparative analysis of the k-nearest-neighbour method and k-means cluster analysis for lithological interpretation of well logs of the shushufindi oilfield, Ecuador. *Rudarsko-geolosko-naftni zbornik*, 37 (4), pp. 155–165. Retrieved from http://dx.doi.org/10.17794/rgn.2022.4.13

Hu, Q., Yu, D., Xie, Z. (2008). Neighborhood classifiers. *Expert Syst. Appl*., 34 (2), pp. 866–876. Retrieved from https://api.semanticscholar.org/CorpusID:11609344.

JCGM member organizations (2008). Evaluation of measurement data – Supplement 1 to the "Guide to the expression of uncertainty in measurement" Propagation of distributions using a Monte Carlo method. In: JCGM organizations: *Evaluation of Measurement data.* pp. 1–80.

Johnston, B. N., Beeson, C. M. (1944). Water permeability of reservoir sands. *Society of Petroleum Engineer Journal*, 160, pp. 43–55.
Retrieved from https://doi.org/10.2118/945043-G

Krause, M., Perrin, J. C., Benson, S. M. (2009). Modeling permeability distributions in a sandstone core for history matching coreflood experiments. *SPE International Conference CO2 Capture Storage, and Utilization*, pp. 25–38.
Retrieved from http://dx.doi.org/10.2118/126340-PA

Mathias, S. A., Gluyas, J. G., Martinez, G. J., Bryant, S. L., Wilson, D. (2013). On relative permeability data uncertainty and CO2 injectivity estimation for brine aquifers. *International Journal of Greenhouse Gas Control*, 12, pp. 200–212.
Retrieved from https://doi.org/10.1016/j.ijggc.2012.09.017

Mitra, P., Murthy, C. A., Pal, S. K. (2002). Density-based multiscale data condensation. *IEEE Transactions on Pattern Analysis and Machine Intelligence*, 24 (6), pp. 734–747. Retrieved from https://doi.org/10.1109/TPAMI.2002.1008381

Papadopoulos, C. E., Yeung, H. (2001). Uncertainty estimation and monte carlo simulation method. *Flow Measurement and Instrumentation*, 12 (4), pp. 291–298. Retrieved from https://doi.org/10.1016/S0955-5986(01)00015-2

Perez, H. H., Datta-Gupta, A., Mishra, S. (2005). The role of electrofacies, lithofacies, and hydraulic flow units in permeability prediction from well logs: a comparative analysis using classification trees. *SPE Reservoir Evaluation & Engineering*, 8 (2), pp. 143–155. Retrieved from https://doi.org/10.2118/84301-PA

Remeczki, F., Szabó, P. N., Dobróka, M. (2020). Flow rate and permeability determination in rock samples from unconventional reservoirs to support the geophysical inversion model. *Geosciences and Engineering*, 8, pp. 154–166.

Silva, A. A., Tavares, M. W., Carrasquilla, A., Misságia, R., Ceia, M. (2020). Petrofacies classification using machine learning algorithm. *Geophysics*, 85, pp. 101–113. Retrieved from https://doi.org/10.1190/geo2019-0439.1

Szabó, N. P., Nehez, K., Hornyák, O., Piller, I., Deák, C., Hanzelik, P. P., Ott, K. (2019). Cluster analysis of core measurements using heterogeneous data sources: an application to complex miocene reservoirs. *Journal of Petroleum Science and Engineering*, 178, July 2019, pp. 575–585.
Retrieved from https://doi.org/10.1016/j.petrol.2019.03.067

Wang, X., Yang, S., Zhao, Y., Wang, Y. (2018). Lithology identification using an optimized KNN clustering method based on entropy-weighed cosine distance in Mesozoic strata of Gaoqing field, Jiyang depression. *Journal of Petroleum Science and Engineering*, 166, pp. 157–174.
Retrieved from https://doi.org/10.1016/j.petrol.2018.03.034

Geosciences and Engineering, Vol. 12, No. 1 (2024), pp. 88–99.
https://doi.org/10.33030/geosciences.2024.01.006

COMPARISON OF DIFFERENT ROCK PHYSICS MODELS FOR ACOUSTIC VELOCITY

HADEER HASSAN
Institute of Exploration Geosciences, Department of Geophysics, University of Miskolc, Hungary; hm.geophysicist@gmail.com
https://orcid.org/0009-0000-8493-4051

Abstract: Unlocking the secrets of rocks is an important task to explore, we require a deep understanding of rock physics. By describing the influence of rock physics on seismic velocities, we attempt to provide a comprehensive understanding of rock physics models and their application to predicting velocities. Throughout the discussion of the most used rock physics models. Moreover, we summarize the results of models using synthetic data to represent relationships between rock physics and elastic moduli. Knowing rock physics models for acoustic waves enhances the interpretation of seismic data, improves reservoir characteristics, aids in fluid identification, and supports uncertainty analysis. However, the choice of model depends on the specific properties of the rock and the application.

Keywords: *rock physics, model, acoustic velocity, elastic moduli, porosity*

1. INTRODUCTION

Rock physics characterizes the performance and physical properties of rocks and geological materials (Mavko et al., 2009). The rock physics aims to construct P-wave velocity (Vp), S-wave velocity (Vs), density (ρ), and their relationships to elastic moduli such as bulk modulus (K) and shear modulus (G), quality factor (Q), porosity (ϕ), pore fluid, pressure, for given lithology and fluid types (Wyllie et al., 1958), (Wyllie et al., 1956). Rock physics is frequently called "velocity-porosity" science. The concept behind this name is to estimate elastic-wave velocities in porous rock based on its porosity (Nur et al., 1998), or to perform an inverse operation and interpret velocity reported in a well (Nolen-Hoeksema and Richard, 2000). In the field of geophysics, acoustic measurements are often used to study the properties of rocks and the subsurface, thus rock physics talks about velocities and elastic parameters because these are what link physical rock properties to seismic expressions which can provide us with valuable information about exploration and production of natural resources, such as water, gas, and oil. To interpret acoustic measurements, rock physics models are used. Rock physics models (RPMs) are used to describe the relationship between the physical properties of rocks and the acoustic properties (Mavko et al., 2020). These models are important for a wide range of applications, including oil and gas exploration, geothermal energy, and earthquake seismology. However, by using these models, geophysicists can better understand the subsurface and make

more accurate predictions about the location and characteristics of subsurface resources. The most used rock physics model is the elasticity model which is widely used for describing the acoustic behavior of the rock (Berryman, 1995). Several rock physics models can be used to describe acoustic measurements, depending on the specific properties of the rock being. In this paper, we will review some of the most used rock physics models for describing acoustic measurements, based on the literature available up to now such as Biot model (Biot, 1956), Gassmann model (Gassmann, 1951), Biot–Gassmann model (Lee, n.d.), Wyllie model (Wyllie et al., 1956), Raymer model (Raymer et al., 1980), the pressure dependence of acoustic velocity and quality factor – new petrophysical models – by Dobróka (Dobróka and Molnár, 2012). These models provide an approach for describing the acoustic behavior of the rock based on its properties. We constructed to test these different models using synthetic data for the physical properties of quartz, and it is assumed to be filled with water. These data are essential in understanding the behavior of acoustic velocity propagation through the different used rock physics models.

2. MATERIALS AND METHODS

The secrets of the rock are so complex that cannot be described without using the exact key to unlock the hidden properties of the rock, moreover, the exact key will not represent all physical properties of the rock it will only show what we search for. Hence, we will go through the most important properties and neglect the others which are dependent on the assumption used for the different models and the parameters used in the different equations to estimate the acoustic velocity.

2.1. Biot model

Biot model (Biot, 1956) is used to describe elastic wave propagation in fluid-saturated porous media. Biot (1941) assumes that the rock formation is porous and saturated with a single fluid, while the rock is isotropic, homogeneous, linearly elastic, and contains well-connected and small pores (Chandrasekaran et al., 2022) with an incompressible fluid.

The Biot theory (Biot, 1956) uses the concept of linear continuum mechanics, connects the elastic moduli and density to the P- and S-wave velocity of the elastic waves in rock matrix as

$$V_P = \sqrt{\frac{K+\frac{4}{3}\mu}{\rho}} \tag{1}$$

$$V_S = \sqrt{\frac{\mu}{\rho}} \tag{2}$$

assuming that the wavelength is much higher than the grain size and the porosity is isotropic and uniform. (Here K is the bulk modulus, μ is the shear modulus, ρ is the

density.) Biot's equation of motion couples the displacement of the rock matrix and that of the fluid constituents. The Biot model has limitations, including assumptions about hypotheses, homogeneous media, static properties (Thomsen, 1985), liquid characteristics (Borregales et al., 2019), and non-uniqueness. These assumptions may lead to inaccurate predictions, as they assume porous media are homogeneous and isotropic. Additionally, static properties do not reflect the dynamic behavior of porous mediums, and the model does not consider the compaction of liquids. Furthermore, the model is not unique, making it difficult to determine the true properties of porous media from velocity data alone. Despite its limitations, Biot's theory has a wide range of applications used in various fields, it is utilized in geophysics (Sahay, 2008), petroleum engineering (Suvorov and Selvadurai, 2019), and civil engineering for interpreting seismic data, predicting fluid flows, and evaluating soil and rock mechanical behavior. However, it has limitations and requires more advanced models to overcome.

2.2. Gassman model

The Gassmann model (Gassmann, 1951) is a widely used theoretical model in geophysics that describes the behavior of fluid-saturated porous rocks (Ciz et al., 2007) which is used to predict seismic velocity when fluid content changes in rocks. Gassmann assumes that the porous material is isotropic, elastic, homogeneous, and composed of one type of mineral. The Gassmann model predicts that the seismic velocity of the rock decreases with increasing fluid saturation, while the attenuation of seismic waves increases (Han and Batzle, 2004). To predict the seismic velocity using the Gassmann model, we first need to calculate the bulk modulus of the saturated rock using the Gassmann equation (Al-Khateb, 2013; Berryman, 1999) which is a key component of the Gassmann model and describes the bulk modulus of the fluid-saturated porous rock (in a low-frequency approximation) as

$$K_s = K^* + \frac{K_0\left(1-\frac{K^*}{K_0}\right)^2}{(1-\phi)\frac{K^*}{K_0}+\phi\frac{K_0}{K_f}} \tag{3}$$

where $K_0, K_f, K^*,$ and K_s are the bulk moduli of the mineral, fluid, dry rock, and saturated rock frame, respectively, ϕ is the porosity. The Gassmann model predicts that the P-wave and S-wave velocities decrease as the fluid saturation of the rock increases. The Gassmann model (Berryman and Milton, 1991) is a widely used tool in geophysics, reservoir engineering, and rock physics. It assumes isotropy, homogeneity, and incomprehensibility of fluids, neglecting frequency and attenuation effects, and ignoring pore liquid chemistry effects. It also assumes that fluid is balanced with external fluid, which may not be the case in all cases. The model is widely used in seismic exploration, reservoir characterization, monitoring of reservoirs, geomechanics, rock physics modelling, and unconventional reservoirs like shale gas

and tight oil formations. However, it should be used with caution and consider its limitations when interpreting seismic data.

2.3. Wyllie model

The Wyllie model (Wyllie et al., 1956) is used to estimate the porosity and P-wave velocity of a rock formation. It is assumed that the density of the rock's solid minerals and its bulk density are connected to the rock's porosity. The Wyllie time-average equation, proposed by Wyllie, Gregory and Gardner (Wyllie et al., 1956), relates sonic velocities to rock porosity. The equation states that total travel time is the sum of the time spent on the rock matrix and that in the pores giving for the propagation velocity

$$\frac{1}{V} = \frac{1-\phi}{V_m} + \frac{\phi}{V_f} \tag{4}$$

where V_m, V_f, ϕ are the matrix velocity, the fluid velocity, and the porosity, respectively. The expression also can be written in terms of interval travel time as

$$\Delta t = \phi \Delta t_f + (1-\phi)\Delta t_m \tag{5}$$

where Δt_f and Δt_m are the values of acoustic travel-time in fluid and rock matrix, respectively.

The Wyllie model has limitations, including its assumption of constant density and velocity for solid minerals, and the rock's internal fluid, as well as its assumption of uniform rocks, and its assumption of isotropic properties. However, it is widely used in petrophysics for estimating porosity, interpretation of seismic data, prediction of rock properties, and reservoir simulation. The model is particularly useful for simple, homogeneous, and water-saturated rocks, but should be considered when applying it to more complex geological settings. By combining Wyllie models with other data, reservoir representations can be more accurate and production strategies optimized.

2.4. Raymer model

Raymer model (Raymer et al., 1980) estimates compressional wave velocity in rock formations using porosity and mineralogy measurements from wireline logs. It assumes matrix and pore space rocks, filled with fluid, and uses density and resistivity measurements to determine reservoir productivity. The Raymer–Hunt–Gardner (RHG) formula proposed a new empirical equation to calculate P-wave velocity in the porous rock sample as a function of the porosity, using matrix- and fluid velocity

$$V_P = (1-\phi)^2 V_m + \phi V_f \tag{6}$$

and for S-wave velocity in dry rocks

$$V_S = (1 - \phi)^2 V_s \tag{7}$$

where V_S is the S-wave velocity in the solid constituent.

The Raymer model has limitations, such as assuming homogeneous and elastic matrix rock and incompressible fluid filling pore space. This can lead to mistakes in porosity and compressional wave velocity estimates. It also has limited accuracy in complex formations, as it is most accurate in simple rock formations with uniform characteristics. The model relies on empirical correlations to determine compressional wave velocity, which may not apply to all types of rocks and fluid mixtures. Additionally, it ignores shear wave velocity, which is crucial in geo-mechanical studies. The Raymer model has several applications in the oil and gas industry, including reservoir characterization, well planning, completion design, production optimization, and seismic interpretation. However, it is essential to consider these limitations when interpreting reservoir data and adjusting production strategies.

2.5. Rock physical model to describe pressure dependence

To describe the pressure dependence of acoustic velocity and quality factor in porous materials (Dobróka and Molnár, 2012) proposed a mathematical model based on the idea that microcracks in rocks open and close under the change of pressure. The model assumes that the material is isotropic and homogeneous. These assumptions are reasonable for materials with homogeneous compositions and structures but may not apply to all materials or conditions. It focuses on uniaxial stress states and longitudinal acoustic waves, providing a theoretical link between propagation speed and rock pressure. The model equation shows that the propagation speed – as a stress function – starts at V_0 (at zero pressure) and increases to $V_{max} = V_0 + \Delta V$ value (at high pressure). The mathematical model gives a velocity vs. pressure expression according to the function $1–\exp(-\lambda\sigma)$, which specifies the range of speeds in which the propagation speed can vary from stress-free states to states characterized by high rock pressure as

$$V(\sigma) = V_o + \Delta V(1 - e^{-\lambda\sigma}) \tag{8}$$

The three model parameters $(V_o, \Delta V, \lambda)$ can be estimated in the inversion of the acoustic velocity dataset measured on rock samples at various pressures. As an example, we show the results sound in the case of a fine-grained sand sample. The measured dataset is shown in *Table 1*.

Table 1

The measured sonic velocity dataset

$\boldsymbol{\sigma}$	0	0.45	0.9	1.8	2.7	3.6	4.5	5.4	6.3
V	2.719	2.733	2.761	2.837	2.934	3.021	3.081	3.13	3.186
$\boldsymbol{\sigma}$	7.2	8.1	9	10.8	12.6	14.4	16.21	18.01	19.81
V	3.219	3.248	3.293	3.349	3.402	3.446	3.496	3.536	3.56

Starting from an initial model $\vec{m}_0$ an iteration procedure is used to improve the model as

$$\vec{m}_{new} = \vec{m}_{old} + \delta\vec{m} \tag{9}$$

with

$$\delta\vec{m} = G^{-g}\delta\vec{d} \tag{10}$$

Here $\delta\vec{d}$ is the data correction,

$$G^{-g} = (\underline{\underline{G}}^T \underline{\underline{G}})^{-1}\underline{\underline{G}}^T \tag{11}$$

is the generalized inverse matrix where $\underline{\underline{G}}$ is the Jacobi matrix, T is the symbol of matrix transpose. The errors of the estimated parameters are computed using the model covariance matrix

$$\underline{\underline{\mathrm{cov}}}^{(m)} = \underline{\underline{G}}^{-g}\,\underline{\underline{\mathrm{cov}}}^{(d)}(\underline{\underline{G}}^{-g})^T \tag{12}$$

where $\underline{\underline{\mathrm{cov}}}^{(d)}$ in the data covariance matrix. The estimation error of the i-th model parameter is given by

$$\sigma_i^{(m)} = \sqrt{\mathrm{cov}_{ii}^{(m)}} \tag{13}$$

In this procedure, *Equation (8)* serves as a forward problem formula. The estimated model parameters with their estimation errors are shown in Table 2.

Table 2

Model parameters estimated by inversion and their estimation errors

	$\mathbf{m_{new}}$	**estimation error**
$\mathbf{V_0}$	2.6936	0.0028
$\Delta\boldsymbol{V}$	0.9767	0.0064
$\boldsymbol{\lambda}$	0.1063	0.0017

The fit between the measured and calculated data is shown in *Figure (1)*. To characterize the accuracy of the estimation, the relative data distance (D [%]) is used

$$D = \sqrt{\frac{1}{N}\sum_{k=1}^{N}\left(\frac{d_k^{(meas)} - d_k^{(calc)}}{d_k^{(calc)}}\right)^2} \quad *100\% \tag{14}$$

where $d_k^{(meas)}$ and $d_k^{(calc)}$ are the k-th measured and calculated data, respectively, N is the total number of data. In our example D = 0.47%.

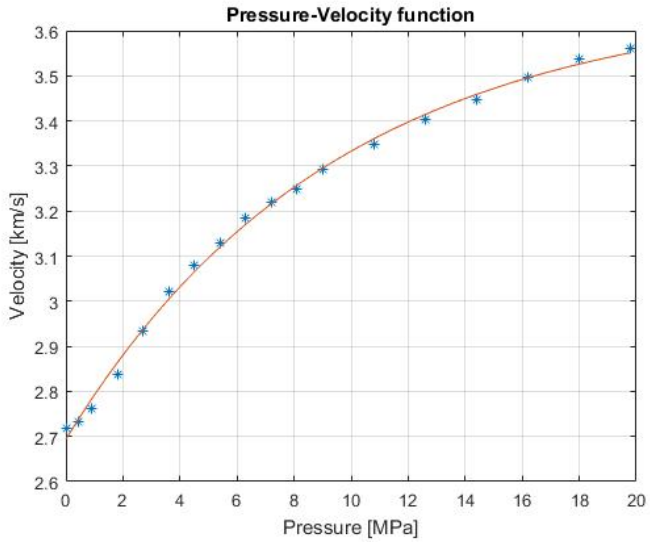

Figure 1

The fit between the measured data given in Table 1 and the calculated ones in LSQ inversion using the forward model in Equation (8)

The above-discussed rock-physical models have several limitations when studying the pressure dependence of acoustic velocity and quality factor in materials. The model can provide useful insights into the pressure dependence of acoustic properties in materials, but its limitations should be carefully considered when interpreting its predictions. Experimental validation and careful parameter selection are essential to ensure the model's accuracy. The model has various applications in materials science, geophysics, and engineering. It is useful for studying the pressure dependence of acoustic properties in rocks and minerals, interpreting seismic data, and making predictions about the behavior of rocks and minerals under high-pressure conditions. It is also useful in materials science and engineering for analyzing material behavior under various pressure conditions, as well as in seismology for a better understanding of the Earth's crust and mantle.

3. RESULTS AND DISCUSSION

MATLAB program has been developed to test these different models using synthetic data. The Biot model states that increasing porosity decreases wave velocity due to a decrease in effective bulk modulus *[Figure 2(a)]*. This model showed the inverse relationship between porosity and velocity in a porous medium *[Figure 2(b)]*.

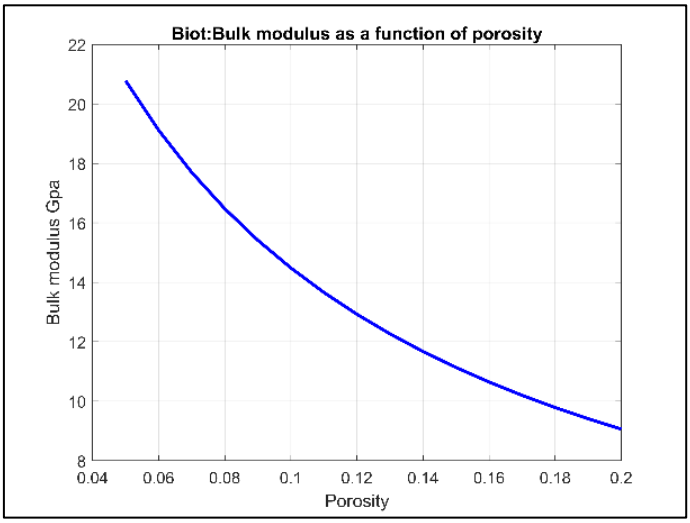

(a)

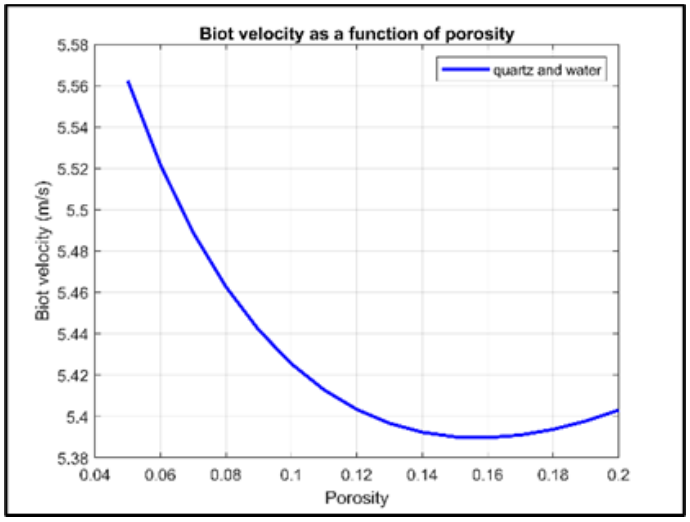

(b)

Figure 2

Biot model (a) Bulk modulus as a function of porosity, (b) velocity as a function of porosity

The Gassmann model describes the relationship between porosity and elastic properties in fluid-saturated porous mediums. *Figure 3(a)* demonstrates that the bulk modulus decreases with increasing porosity, as the effective bulk modulus decreases. *Figure 3(b)* illustrates an inverse relationship between porosity and velocity.

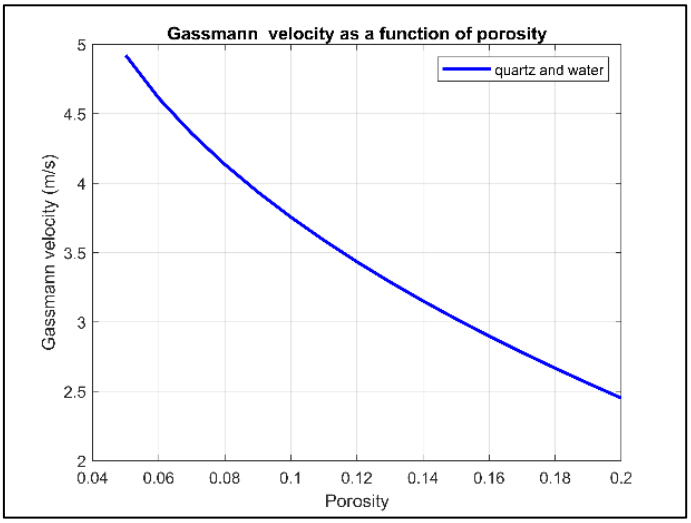

(a)

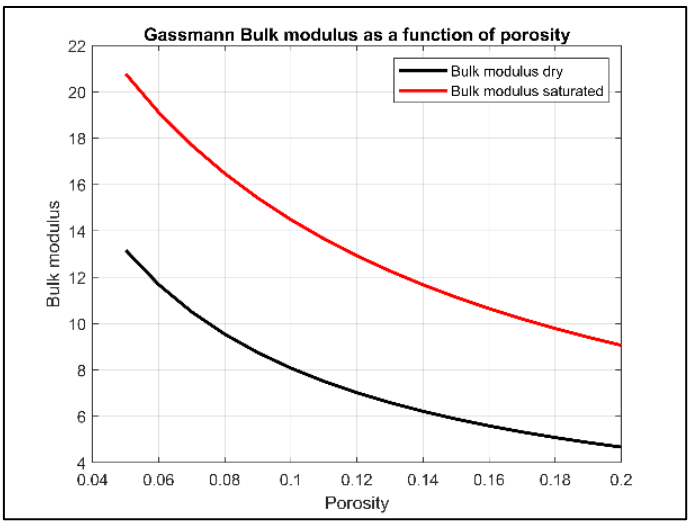

(b)

Figure 3

Gassmann model (a) velocity as a function of porosity, (b) Bulk modulus as a function of porosity

One of the earliest and most widely used transforms is the Wyllie time-average equation (Wyllie et al., 1958) which is used to determine a relationship between compressional velocity (or acoustic velocity) and porosity. This relationship is only reliable for consolidated sandstones over a small porosity range of 25%–30% (Raymer et al., 1980). The Wyllie model states that seismic wave velocity is directly propor-

tional to the compressional modulus and inversely proportional to porosity. As porosity increases, the velocity decreases, while an improved version of the time-average equation, developed by Raymer et al. (1980), is shown in *Figure 4*.

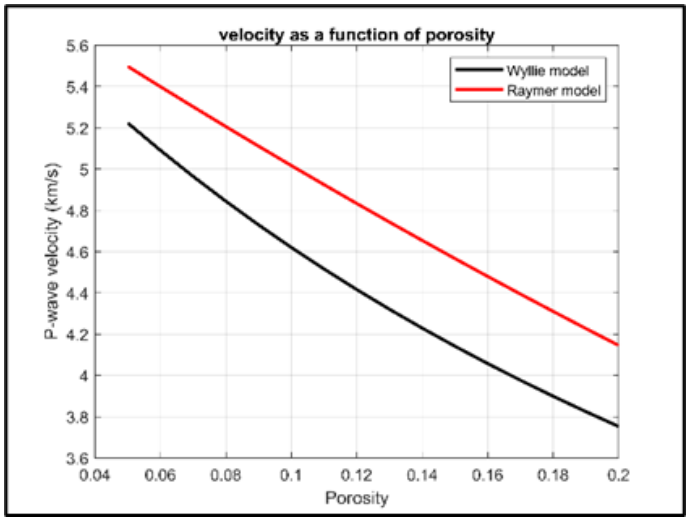

Figure 4
Velocity as a function of porosity in Wyllie and Raymer models

4. CONCLUSIONS

Theoretical modeling of velocity plays an important role in describing the acoustic behavior of rocks. Furthermore, we can recognize the inverse relation between porosity and velocity in all the discussed models. For porosities greater than the critical porosity, velocity is not strongly dependent on porosity. For values below the critical porosity, velocity depends strongly on porosity and increases significantly with a small decrease in porosity and the models described in this paper are just a few examples of the many models that have been developed over the years. The choice of model depends on the specific properties of the rock. By understanding these models, scientists and engineers can better predict the behavior of rocks and improve our understanding of the subsurface.

REFERENCES

Al-Khateb, N. (2013). A look into Gassmann's Equation. *Integration, geoConvention, Proceedings geoConvention*, Calgary, Canada, pp. 1–6.

Berryman, J. G. (1995). *Mixture Theories for Rock Properties.* Book Series: American Geophysical Union. pp. 205–228. https://doi.org/10.1029/rf003p0205

Berryman, J. G. (1999). Origin of Gassmann's equations. *Geophysics*, 64 (5), pp. 1627–1629. http://library.seg.org/

Berryman, J. G., & Milton, G. W. (1991). Exact results for generalized Gassmann's equations in composite porous media with two constituents. *Geophysics*, 56 (12), pp. 1950–1960. https://doi.org/10.1190/1.1443006

Biot, M. A. (1941). General theory of three-dimensional consolidation. *Journal of Applied Physics*, 12 (2), pp. 155–164. https://doi.org/10.1063/1.1712886

Biot, M. A. (1956). Theory of Propagation of Elastic Waves in a Fluid-Saturated Porous Solid. I. Low-Frequency Range. *The Journal of The Acoustical Society of America*, 28 (2), pp. 168–178.

Borregales, M. A., Kumar, K., Nordbotten, J. M., & Radu, F. A. (2019). *Iterative solvers for Biot model under small and large deformation*. http://arxiv.org/abs/1905.12996.

Chandrasekaran, S. N., Näsholm, S. P., & Holm, S. (2022). Wave equations for porous media described by the Biot model. *The Journal of the Acoustical Society of America*, 151 (4), pp. 2576–2586. https://doi.org/10.1121/10.0010164

Ciz, R., & Shapiro, S. A. (2007). Generalization of Gassmann equations for porous media saturated with a solid material. *Geophysics*, 72 (6). https://doi.org/10.1190/1.2772400

Dobróka, M., & Molnár, J. S. (2012). New petrophysical model describing the pressure dependence of seismic velocity. *Acta Geophysica*, 60 (2), pp. 371–383. https://doi.org/10.2478/s11600-011-0079-0

Gassmann, F. (1951). Elastic Waves Though a Packing of Spheres. *Geophysics*, 16, pp. 673–685. http://library.seg.org/

Han, D. H., & Batzle, M. L. (2004). Gassmann's equation and fluid-saturation effects on seismic velocities. *Geophysics*, 69 (2), pp. 398–405. https://doi.org/10.1190/1.1707059

Lee, M. W. (n.d.). *Comparison of the Modified Biot-Gassmann Theory and the Kuster-Toksöz Theory in Predicting Elastic Velocities of Sediments*. http://www.usgs.gov/pubprod

Mavko, G., Mukerji, T., & Dvorkin, J. (2009). *Rock Physics Handbook: Tools for Seismic Analysis of Porous Media*. Cambridge University Press.

Mavko, G., Mukerji, T., & Dvorkin, J. (2020). Empirical Relations. In *The Rock Physics Handbook*. Cambridge University Press. pp. 474–524. https://doi.org/10.1017/9781108333016.008

Nolen-Hoeksema, & Richard, C. (2000). Modulus-porosity relations, Gassmann's equations, and the low-frequency elastic-wave response to fluids. *Geophysics*, 65 (5), pp. 1355–1363.

Nur, A., Mavko, G., Dvorkin, J., & Galmudi, D. (1998). Critical porosity: A key to relating physical properties to porosity in rocks. *The Leading Edge*, 17, pp. 357–362. http://library.seg.org/

Raymer, L. L., Hunt, E. R., & Gardner, J. S. (1980). An improved sonic transit time to porosity transform. *SPWLA Logging Symposium, 21st annual* (Transactions), 12.

Sahay, P. N. (2008). On the Biot slow S-wave. *Geophysics*, 73 (4). https://doi.org/10.1190/1.2938636

Suvorov, A. P., & Selvadurai, A. P. S. (2019). The Biot coefficient for an elasto-plastic material. *International Journal of Engineering Science*, 145. https://doi.org/10.1016/j.ijengsci.2019.103166

Thomsen, L. (1985). Biot-consistent elastic moduli of porous rocks: Low-frequency limit. *Geophysics*, 50 (12).

Wyllie, M. R. J., Gregory, A. R., & Gardner, G. H. F. (1958). An Experimental Investigation of Factors Affecting Elastic Wave Velocities in Porous Media. *Geophysics*, 23 (3), pp. 459–493. http://library.seg.org/

Wyllie, M. R. J., Gregory, A. R., & Gardner, I. W. (1956). Elastic Wave Velocities in Heterogeneous and Porous Media. *Geophysics*, XXI (1), pp. 41–70. http://library.seg.org/

Geosciences and Engineering, Vol. 12, No. 1 (2024), pp. 100–118.
https://doi.org/10.33030/geosciences.2024.01.007

RECYCLING TECHNIQUES FOR CRYSTALLINE SILICON AND THIN FILM PV PANELS: AN OVERVIEW

MAEN ALWAHSH[1*], GÁBOR MUCSI[2]
[1*]*Institute of Raw Material Preparation and Environmental Technology, University of Miskolc, Miskolc, Hungary; maenalwahsh@hotmail.com*
[2]*Institute of Raw Material Preparation and Environmental Technology, University of Miskolc, Miskolc, Hungary; gabor.mucsi@uni-miskolc.hu*

Abstract: Over the last few years there has been a growing trend towards using solar electricity as an alternative source of energy. In order to meet the world's projected energy needs, PV panel technology is a major alternative to fossil fuels. Due to the increase in production, PV panels with a lifetime of between 25 and 30 years are potential for photovoltaic waste over the next few years. The environmental damage caused by PV panels is significantly reduced when they are recycled. The recycling also contributes to the recovery of materials, some of which are rare in nature. The structure of the components that make up this paper. From 2050 onwards, the estimated PV waste projections for the world have been analyzed.

Keywords: *Solar energy, photovoltaic panel, components of PV panel, recycling*

1. INTRODUCTION

Originally utilized in space, solar photovoltaic (PV) energy technologies are now widely applicable anywhere electricity is needed. One of the most developed and promising methods for producing renewable energy is photovoltaic (PV) energy production. PV technology is a common way to generate power and is also environmentally friendly. After hydropower and wind power, which are currently the world's most popular renewable energy sources, solar energy technology is currently in third place (Paiano, 2015). PV energy sources also produce electricity with minimal emissions of carbon that contribute to global warming. Moreover, the amount of CO_2 emitted per kWh from fossil fuel-generated power ranges from 400 to 1000 g CO_2 equivalent, while silicon-based solar panels emit very little CO_2 (Shin et al., 2017). The comparison between CO_2 emissions in the production and recycling of photovoltaic (PV) panels reveals significant variations based on panel type and manufacturing process. In the production phase, the amount of CO_2 emitted varies by nation and panel type, with polycrystalline panels generally emitting around 17-182 kg CO_2 per 1 m^2. Conversely, recycling processes result in significantly lower emissions due to reduced energy and raw material requirements (Vellini et al., 2017). Overall, while PV panel production contributes to CO_2 emissions, recycling processes significantly reduce these emissions, highlighting the

importance of sustainable practices in the solar energy industry. Solar energy is dependable, efficient, safe, and pollutant-free. As a result, PV technology has a very promising future for meeting global energy demands. Solar PV power has been used more often over the last few decades. PV panels have a sizable market today and have the ability to generate sustainable energy on a global scale. Furthermore, it is anticipated that PV-generated electricity will overtake other worldwide energy sources as the dominant energy source within the current century (Xu et al., 2018). The growth of renewable capacity over the next five years will happen far more quickly than was predicted even a year ago. According to IEA's projection, renewables will grow by about 2400 GW over 2022–2027, which is equivalent to China's whole installed electricity capacity at present. This represents IEA's highest-ever upward revision and an acceleration of 85% from the prior five years and approximately 30% above the prediction in the previous year's report. Over 90% of the increase in the world's electrical capacity is expected to come from renewable sources during the projection period (Paiano, 2015). As a result, a sustainable plan for the removal of outdated solar panels is required for the growth of PV module recycling as a multidisciplinary field of study. Examining the available technologies can be useful in controlling and assessing the EoL PV modules (Mahmoudi et al., 2019). Developing low-cost recycling technology is essential for the developing PV sector in order to ensure the sustainability of PV at high deployment stages. Concurrently with these new technologies' quick commercialization. In an effort to reduce the detrimental effects of the continuous increase in the volume of PV waste and to institute solar module recycling, the European Union (EU) has incorporated PV waste into the new Waste of Electrical and Electronic Equipment (WEEE) directive (D'Adamo et al., 2017).

2. COMPONENTS OF PHOTOVOLTAIC PANELS

A solar panel, a battery or battery pack, and a solar controller are the three main components of a conventional solar power system. An inverter is required as part of the arrangement whether the output power is 110 V (AC) or 220 V (AC). Heat is produced as a result of the low energy waves that the PV modules have effectively collected, and shortwave irradiance from the sun is directly transformed into electricity by the semiconductor component of the PV cell. A photovoltaic system's internal components and exterior environmental conditions can affect how much power and current a solar cell can produce. Numerous elements, including installation, PV system, cost, and environmental considerations, influence the operation of solar systems and the power they produce. The two primary categories of solar panels available on the market are crystalline silicon and thin-film silicon (Artaş et al., 2023). Silicon, both monocrystalline and polycrystalline, is the most common material used to make PV panels. Solar arrays are equipped with crystalline silicon panels, which offer excellent recycling capacity. The primary goal of thin-film solar panels is cost reduction; these panels appear uniform but have extremely poor efficiency. Solar radiation is directly converted into electrical energy

by solar panels through the use of the photovoltaic effect of the semiconductor material in the panel. A few solar cells connected in series make up the PV panel, which is the fundamental part of the system. The battery group's job is to store the energy released during panel illumination so that it can be supplied to the load whenever needed. The controller's job is to automatically guard against overcharging the battery. Transforming direct current into alternating current is the inverter's job. The fundamental power producing components of a solar power system are solar panels (Xu et al., 2018).

The typical PV panel components listed below are presented in *Figure 1* (Krebs & Frischknecht, 2022). Aluminum (Al) frame, Tempered glass, Solar cells, EVA Film (ethylene/vinyl acetate copolymer), Backsheet (TPT, Topotecan Hydrochloride), and Junction box.

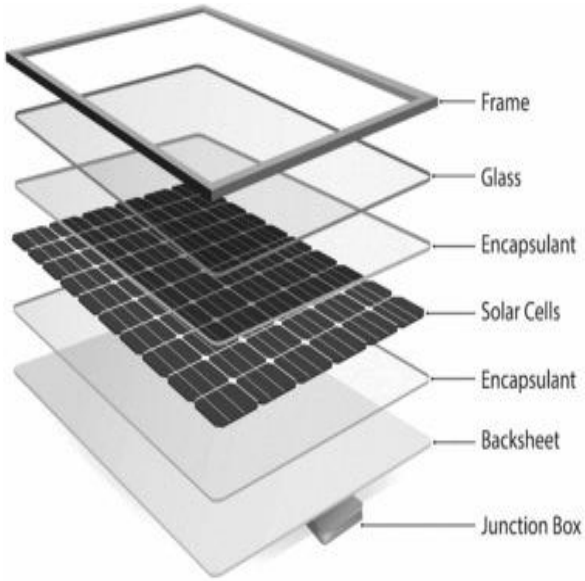

Figure 1
PV panel components (Krebs & Frischknecht, 2022)

With the advancement of technology and a more competitive industry, panels have grown tougher and lighter over time. It comes from mass reduction brought about by thinner glass sheets, frames, and layers as a result of optimized cell and panel designs. The composition of the materials used in PV panels has not changed significantly. Every link in the PV value chain makes it possible to produce more goods with a given amount of materials and resources. The goal of resource and material efficiency is to maximize environmental benefits while making sustainable use of the planet's finite resources. The mass/power ratio has been continuously declining over time as a result of material savings in PV panels and increased solar cell efficiency, as seen in *Figure 2* from IRENA (Weckend et al., 2016).

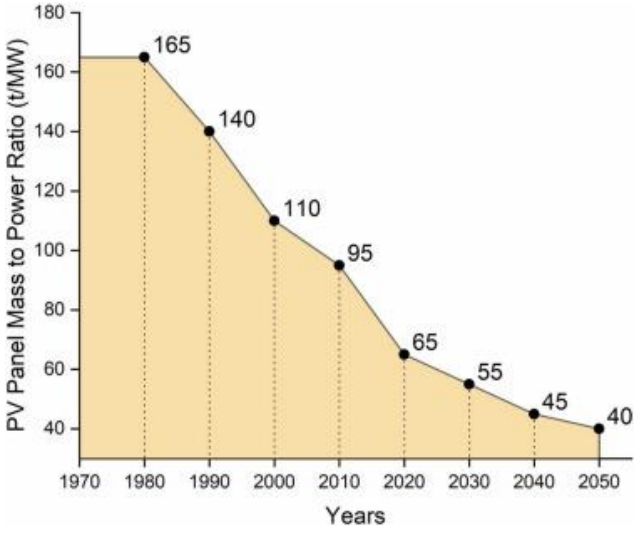

Figure 2

Decreasing of the mass/power ratio over the years (t/MW) (Weckend et al., 2016)

2.1. Crystal Silicon PV Panel

The earliest photovoltaic technologies are crystalline silicon PV panels, which currently hold a 92% market share (51% for polycrystalline and 41% for monocrystalline technologies when the global market is taken into account). In terms of crystalline silicon technology, monocrystalline silicon PV panels hold a 45% market share, while polycrystalline silicon PV panels hold a 55% share. Due to low productivity rates, production of a-Si products has been halted recently, and its market share is currently very small. Ninety-three percent of c-Si PV modules were made by Asian producers in 2021. With a share of 70%, China leads the way (Artaş et al., 2023).

2.1.1. Monocrystalline Silicon PV Panel

Using the Czochralski technique, which requires silicon to be in a molten state at 1400 ºC, first-generation monocrystalline silicon is formed as ingots. These solar cells are the most expensive of all solar cells and, in spite of their great lifetime and efficiency, demand a comparatively large energy expenditure for first-generation PV when compared to other technologies (Wang et al., 2014). PV cells are made primarily of semiconductor materials. A highly pure form of silicon is used to create monocrystalline silicon cells, which increases their photoelectric conversion efficiency. Compared to other solar cells, monocrystalline solar cells are more efficient, with an efficiency of above 20%. An additional benefit of monocrystalline cells is their extended longevity. For this kind of system, many manufacturers issue warranties of up to 25–30 years. Thus, from a financial standpoint, consumers typically choose polycrystalline solar panels as their primary PV panel type (Fernandes et al., 2016).

2.1.2. Polycrystalline Silicon PV Panel

A vital component in the manufacture of photovoltaic panels is polycrystalline silicon. The polycrystalline silicon solar cell has become increasingly more significant than the single-crystal silicon cell due to its simpler production process, which also makes it less expensive overall. Moreover, the efficiency of commercial polycrystalline silicon cells ranges from 13 to 19%. Cells that comprise several tiny silicon crystals are the building blocks of polycrystalline modules. Polycrystalline modules have an ice appearance due to many tiny crystals (Chen et al., 2011).

2.2. Thin-film PV Panel

Thin-film panels are 7% of PV panels. In terms of technology, silicon-based panels are simpler than thin-film panels. Thin-film panels are composed of massive materials such as polymer, glass, or metal that have thin layers of semiconductor material placed on them. There are two main types of thin-film technologies: CdTe (cadmium telluride) and CIGS (copper indium gallium selenide). With a laboratory efficiency of 21.0% for CdTe cells and 23.4% for CIGS cells, the cell efficiency is the greatest in thin-film technology. From 9% to 19%, the efficiency of CdTe modules has recently enhanced (Artaş et al., 2023).

2.2.1. CIGS (Copper-Indium-Gallium-Selenide)

Because of its many advantages, including easier fabrication processes and increased efficiency at the module and cell levels, the CIGS-based solar cell is regarded as one of the most promising thin-film solar cells. Simultaneously, because CIGS solar cells provide the user additional options of flexibility and low weight, they are excellent candidates for use in the manufacturing of thin-film cells. Alkali element post-deposition procedures, particularly those involving heavy alkali elements, have recently had a major impact on raising CIGS cell performance (Bouabdelli et al., 2020).

2.2.2. CdTe (Cadmium Telluride)

Both substrate and top sheet configurations are possible for the CdTe panel, with the top sheet variant being selected for higher than 17% efficiency. In thin-film cells, CdTe is crucial. According to some reports, CIGS panels cost about 30% more than CdTe technology. Thus, thin-film cells based on CdTe can yield a good efficiency/cost ratio (Nykyruy et al., 2019).

3. SOLAR PV PANEL WASTE PROJECTION

The number of waste streams from PV panels will rise as PV is deployed globally. For the years up until 2050 (Weckend et al., 2016).

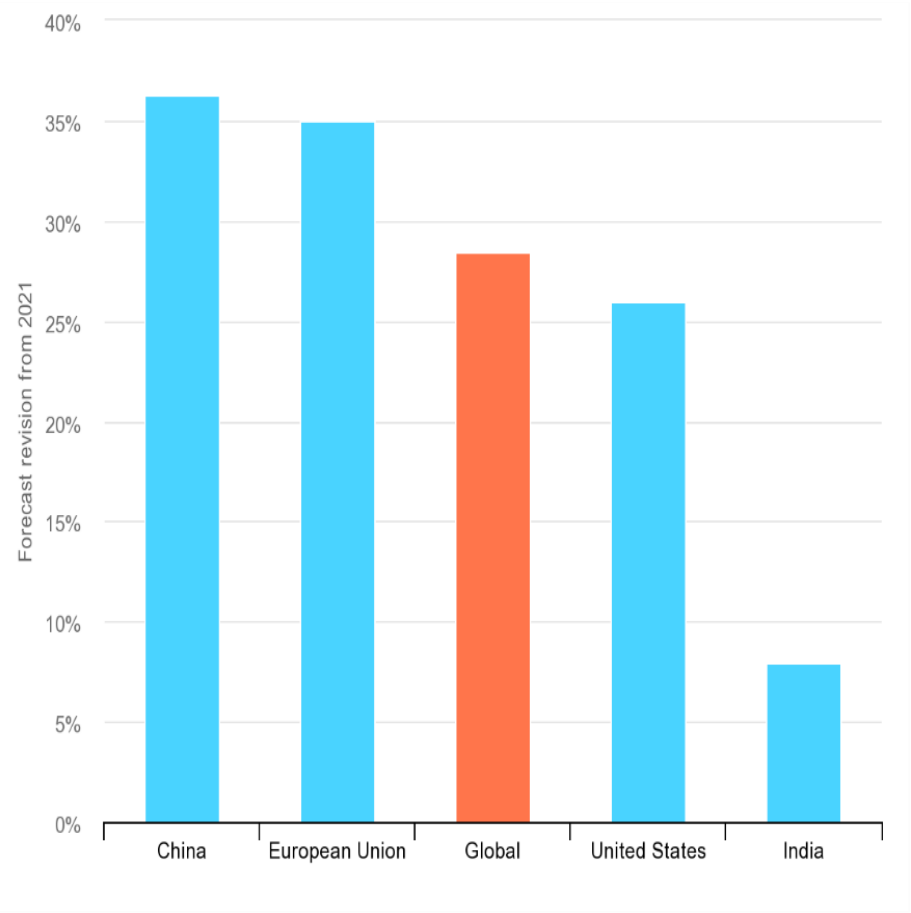

Figure 3
Upward revisions to renewable capacity expansion forecasts from Renewables 2021 to Renewables 2022 (Weckend et al., 2016)

Figure 4 displays the market share of solar panels by technology group. The number of fully connected PV panels is currently rapidly increasing. Given that solar panels typically have a 25-year useful life, rapid expansion is predicted in the upcoming years. Nonetheless, it is anticipated that by 2050, the entire amount of EOL PV panels would be 9.57 million tons. In 2014, silicon-based c-Si panels held a 92% market share, followed by CdTe-based panels at 5% and copper indium gallium (CIGS) at 2%. The remaining 1% of the market was occupied by panels made of other materials, such as dye-sensitized, CPV, and organic hybrids. Between 2014 and 2030, the market share of c-Si PV panels is expected to drop from 92% to 44.8% (Bouabdelli et al., 2020) (Nykyruy et al., 2019). Over the same time span, third-generation PV panels are expected to increase from a base of 1% in 2014 to 44.1% (Chowdhury et al., 2020).

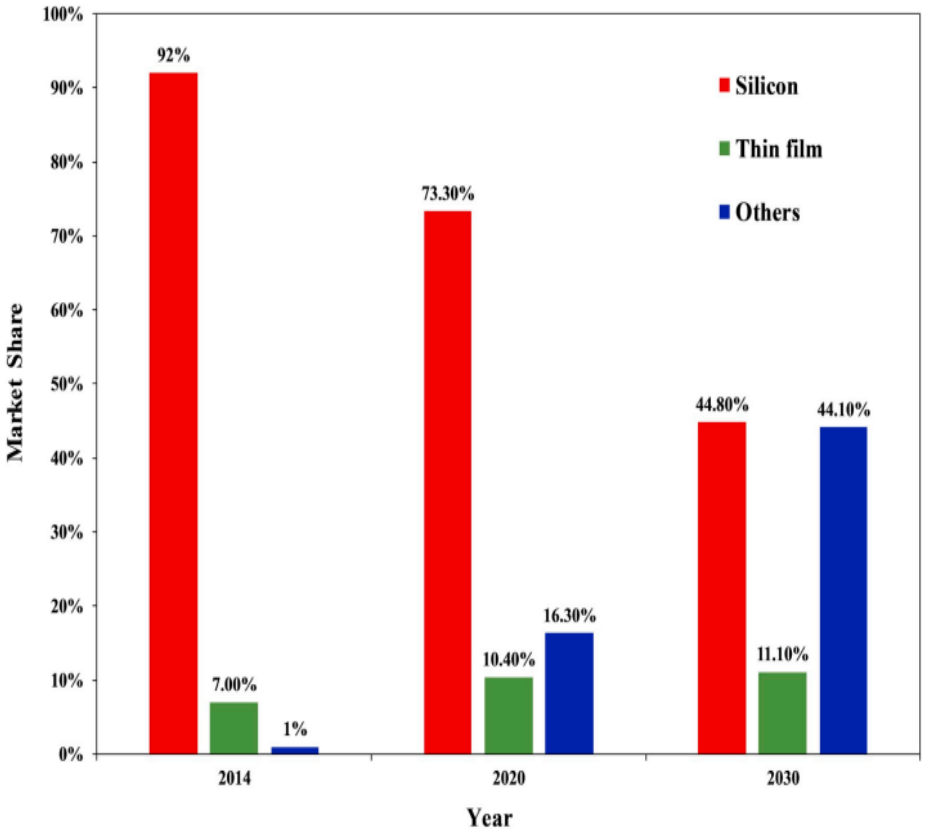

Figure 4
Market share of PV panels by technology type (2014–2030)
(Chowdhury et al., 2020)

According to estimates from the International Renewable Energy Agency (IRENA), there were over 250,000 metric tons of discarded solar panels in the world by the end of 2016 (Huang et al., 2017). Lead (Pb), cadmium (Cd), and numerous other dangerous substances are present in the solar panels and cannot be eliminated even if the panel breaks completely. The Japanese Environment Minister warned in November 2016 that the nation lacked preparations to properly and safely dispose of the 10,000–800,000 tons of solar panel waste produced year in Japan by 2040 (Yi et al., 2014). According to a recent statement, Toshiba Environmental Solutions estimates that it will take roughly 19 years to reprocess all of Japan's huge solar waste that is created by 2020. By 2034, the annual garbage will have increased 70–80 times compared to the year prior to 2020 (Yi et al., 2014). There are now two commercially accessible types of PV recycling technology, although additional technologies are being investigated. Thin film technology employing either CdTe or CIGS technology is the second-largest market segment, followed by panels produced using c-Si

technology. Because of their distinct module architectures, the recycling procedures for c-Si PV panels differ from those used for thin film PV panels (Smith & Bogust, 2018). One significant difference is that the goal of removing the encapsulant from the compound photovoltaic modules' layered structure is to retrieve the substrate glass and quilted glass, which house the semiconductor layer. Thus, the goal of recycling c-Si modules is to separate the glass and retrieve the Si cells along with other metals. The process used to recycle Si-based PV panels involves layer separation, which calls for the removal of the panel's encapsulant and the Si cells themselves in order to recover the metals (Kurinec, 2018).

3.1. Causes of solar PV panel failure

New solar panels should have comparatively few problems, with minor erosion (0.5–5%) being the most common; the main causes are subpar design and manufacturing flaws. According to *Figure 5*, there are various reasons for panel failure, including problems with grounding and electrical equipment such charge controllers, junction boxes, fuse boxes, and cabling. Early on in its manufacture, solar panels experienced incoherency from broken solar cells and deterioration of the colorless ethylene vinyl acetate (EVA) anti-reflective coating layer that was added to the glass (Chowdhury et al., 2020).

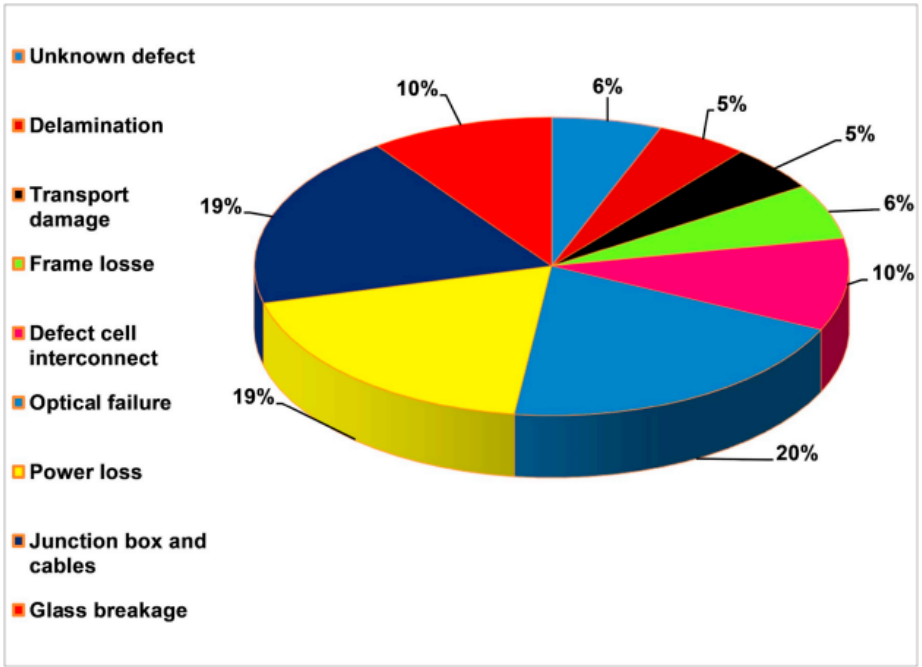

Figure 5

PV panel failure rates according to customer complaints (Chowdhury et al., 2020)

Over the course of the first 12 years of operation, a number of factors contributed to failures, including repeated load cycles brought on by wind, snow, and temperature variations that resulted in degradation, contact defects in junction boxes, glass breakage, burst frames, cell interconnection breaks, and issues with the diodes linked to an increased rate of interconnectors and cell degradations. According to earlier studies, microscopic cracks and failures accounted for 40% of PV panel failures. Since 2008, when thin cell panel production started, this explanation has become the most prevalent in more recent panels (Weckend et al., 2016).

4. COMPARISON OF THE AMOUNT OF CO2 EMISSIONS OCCURRING IN PHOTOVOLTAIC PANEL PRODUCTION AND RECYCLING

Since solar energy produces fewer carbon emissions than other energy production techniques, it is seen as an ecologically beneficial means of producing electricity. However, these techniques not only use energy but also have an impact on the environment, either directly or indirectly. several procedures, such as the procurement and processing of certain materials utilizing chemicals in manufacturing. However, even though adding panels to solar power plants produces energy, doing so damages the environment and releases some CO_2 emissions into the atmosphere. PV technology is receiving a lot of attention, which is causing it to advance gradually and produce many panels with higher performance (Yildiz et al., 2020). The raw materials used and differences in the manufacturing process cause the quantity of CO_2 emissions to vary based on the type of solar panel. By 2050, using more than 8500 GW of solar energy may provide more than 25% of the world's electrical needs and perhaps save significant CO_2 emissions (4.9 Gt CO_2). This illustrates how energy efficiency measures and renewable energy sources may reduce CO_2 emissions by 21% of the total. Up to 2050, photovoltaic technology has the largest potential to reduce CO_2 emissions of all low-carbon options. The primary reason for this is the significant growth of solar energy, which has supplanted conventional power generating methods with the finest technological solutions and sufficient resource availability at better resource areas (Gielen et al., 2019).

Due to advancements in the photovoltaic sector and rising demand, CO_2 emissions from the manufacture of solar panels have nearly quadrupled globally to 51,900 kilotonnes of carbon dioxide in 2021, or around 0.15% of all energy-related emissions worldwide. However, improvements in material and energy efficiency as well as lower emissions from the production of power have offset increases in CO_2 emissions in several nations (Abdelilah et al., 2022). This section looks at the CO_2 emissions produced during the manufacturing and recycling of CdTe and polycrystalline panels, as well as the variations in their amounts. Currently, the study is concentrated on CdTe and polycrystalline panels because CdTe PV technology contains toxic materials like gallium, arsenic, cadmium, lead, and selenium, which pose serious environmental and health risks if not properly managed at the end of their life cycle (European Commission, 2011). Additionally, polycrystalline panels, which include high-value c-Si PV modules, are significant due to the economic impact of materials

like silver and aluminum, with silver contributing the most to revenue due to its high market price and aluminum being important because of the large quantity used in frames (Hocine & Samira, 2019).

4.1. Average Amount of CO_2 Emissions in Polycrystalline PV Panel Production

The usage of a certain quantity of energy at each stage of the production of solar panels results in either direct or indirect CO_2 emissions. In the nations that produce PV panels, the quantity of CO_2 emissions emitted during the production of 1 m^2 of polycrystalline PV panels has been estimated roundly. Various CO_2 emission amounts have been observed in each nation during the production of a 1 m^2 polycrystalline panel.

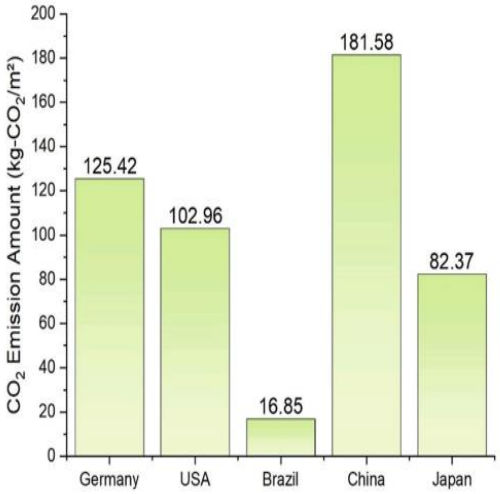

Figure 6

This is the distribution of the average amount of CO2 emissions released to the environment in the production of polycrystalline PV panels by country (Gökhan et al., 2020)

The estimated CO_2 emissions, as shown in *Figure 6*, are as follows: approximately 125 kilogram CO_2 in Germany, approximately 102 kg CO_2 in the USA, approximately 17 kg CO_2 in Brazil, approximately 83 kg CO_2, and approximately 182 kg CO_2 in Japan and China (Yildiz et al., 2020).

4.2. Average CO_2 Emission Amount During Recycling of Polycrystalline PV Panel

PV panels that are recycled contribute significantly to the output of new panels. Due to the fact that many recycled panel methods use fewer raw materials (Müller, 2006). When comparing the recycling process to the normal process, which involves procuring silicon and manufacturing sheets, relatively few raw materials are used.

Lower CO_2 emissions are produced by the recycling process as it requires a lot less energy and raw materials than the conventional method from silicon supply to sheet production (Yue et al., 2014). The recyclable panel serves as the primary source of raw materials for the backsheet's manufacturing. By using this process, 0.888 m^2 of polycrystalline solar panels are produced, assuming that a 1 m^2 polycrystalline panel is recycled. This process consumed 21.1 kWh of energy. Because energy usage generates indirect CO_2 emissions, it varies between nations by 2.20–20.47 kg-CO_2. The countries' CO_2 emission levels are displayed in *Figure 7*. The computation's result indicates that the production of recycled panels and non-recyclable panels results in significantly different CO_2 emissions. These findings demonstrate the significance of recycling.

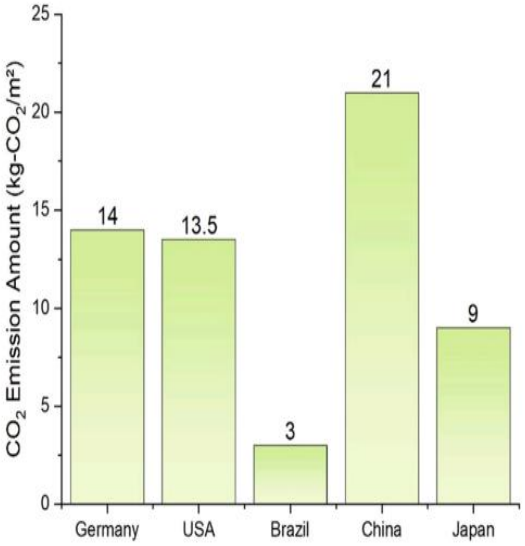

Figure 7
The amount of CO2 emission during the recycling of the polycrystalline panel
(Yildiz et al., 2020)

4.3. Average Amount of CO_2 Emissions in CdTe PV Panel Production

1.25 kWh of electricity are needed for the cadmium purification process in order to produce 1 kilogram of cadmium. Consequently, CO_2 emissions in the range of 0.11–1.21 kg-CO_2 are seen when five nations are compared. The energy required in the semiconductor cadium manufacturing process is 3.86 kWh after purification. Emissions of CO_2 into the atmosphere during this process range from 0.35 to 3.74 kg-CO2. Utilizing 0.0425 kWh of energy, 0.646 kg of semiconductor cadmium and 0.419 kilogram of hydrochloric acid react to make 1 kg of $CdCl_2$. Low CO_2 emissions of around 0.3–41.23 g-CO_2 are produced by this technique. Following this technique results in the production of CdS using 0.004 kWh of energy and insignificant CO_2 emissions for the process within the range of 0.00036−0.00388 g-cCO_2 (Corcelli et

al., 2017). A little amount of CO_2 emissions, between 3.87 and 41.71 g-CO_2, are produced during the 0.043 kWh of power consumed in the tellurium procurement process that is necessary for the production of PV panels. CO_2 emissions range from 0.98 to 10.56 kg-CO_2 throughout the process of turning tellurium into semiconductor tellurium. The environmental CO_2 emissions linked to the production of CdTe PV panels are broken out by nation in *Figure 8*. Based on data from five nations, the CO_2 emission quantity of 1 m^2 CdTe PV manufacturing was computed. Various CO_2 emission amounts have been observed in each nation during the manufacture of 1 m^2 CdTe PV panels.

Furthermore, when the production of a 1 m^2 CdTe PV panel is compared to that of a 1 m^2 polycrystalline PV panel, the CdTe PV panel is determined with values that result in lower CO_2 emissions (Yildiz et al., 2020).

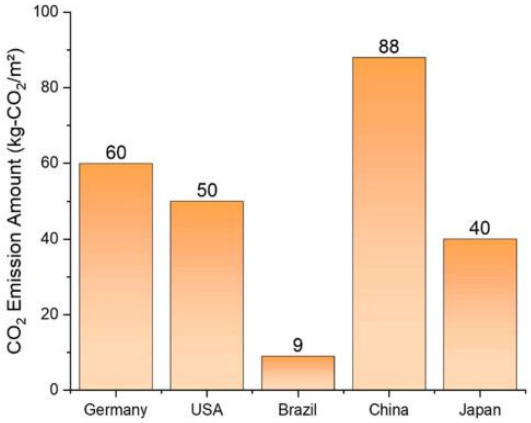

Figure 8

Distribution of the average amount of CO2 emissions released to the environment in CdTe PV panel manufacturing by country (Yildiz et al., 2020)

4.4. Average CO_2 Emission Amount During Recycling of CdTe PV Panel

Roughly 90% of CdTe photovoltaic panels that are recycled are retrieved. This makes the process of fabricating CdTe photovoltaic panels relatively easy and resource efficient. Analyzing the recycling of a 1 m^2 CdTe PV panel reveals that the procedure results in the discharge of 0.0412 kg of CdTe PV panel. In this procedure, 4.4 kWh of energy are consumed, and as a result, indirect CO_2 emissions vary from 0.4 to 4.27 kg-CO_2 (Vellini et al., 2017). The quantity of CO_2 emissions that each nation has released into the atmosphere as a result of recycling CdTe photovoltaic panels is displayed in *Figure 9*. The manufacturing of CdTe PV panels and recycled panels is seen to produce notably different CO_2 emissions and non-recyclable panels. Research has demonstrated that every type of photovoltaic panel provides notable energy savings during production, which in turn leads to substantial reductions in

CO2 emissions through recycling (Yildiz et al., 2020). Despite the fact that cadmium is one of the most toxic substances known to man, a CdTe panel has lower primary energy consumption, an EPBT value, and all other impact potentials because of the recycling process, which guarantees that a significant amount of CdTe semiconductor is supplied to the panel fabrication stage. Panel production is a simpler process than that of silicon panels. The findings demonstrate that although CdTe cells have a poorer energy efficiency than Si cells, they can compensate for this with benefits to the economics, environment, and energy (Vellini et al., 2017).

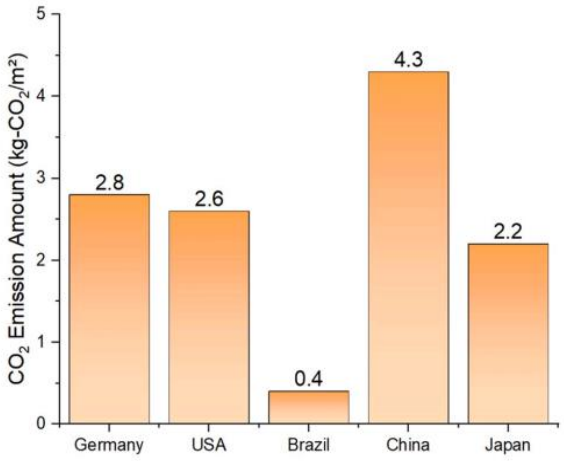

Figure 9
The amount of CO2 emissions during the recycling of CdTe panels
(Yildiz et al., 2020)

5. EXISTING METHODS OF THE RECYCLING PROCESS

5.1. Recycling Techniques of Crystalline Silicon PV Panels

Before the sandwich-sheet-like structure can be removed from crystalline silicon solar panels for recycling, a frame needs to be separated. Since each manufacturer has a different profile, size, and method of fastening, the frame is often disassembled by hand. The delamination of the EVA layer is the next stage in separating the silicon cell and glass. The waste panels enter at this point as a whole, and the EVA glass components are separated once they are separated (Artaş et al., 2023). There are two types of delamination techniques: chemical and thermal. Thermal treatments include fluidized bed heat treatment, pyrolysis, and electro-thermal heating. Chemical techniques include the use of solvent, nitric acid dissolution, ultrasonic irradiation, and solvent dissolution. Methods such as fluidized bed pyrolysis, electro-thermal heating, and nitric acid dissolution combine to yield silicon as one output and metal assemblages and transparent glass as the other. After delamination, glass components, crystalline silicon cells, and metal compounds move

on to the material separation stage. Glass and metal compounds are produced as one output, and silicon cell chips are produced as the result of a combination of ultrasonic irradiation, solvent, solvent dissolution, and heat treatment. Chemical etching is the only method available for material separation in c-Si. This process mixes nitric, ethanoic, and hydrofluoric acids in the presence of bromine gas. Glass is helped to separate from silicon cells and metal compounds by this process (Maani et al., 2020).

5.2. Recycling Techniques of Thin Film PV Panels

Modules can be divided by cutting, crushing, or both, as well as by a thermal or solvent-based delamination process. The mechanical methods include hot wire cutting, hammer grinding, laser irradiation, and shredding. A life cycle study of laser irradiation and hot wire cutting cannot be performed at this time because there is no industrial instruction available. The sole thermal method requires heating the panels to 500 °C in a laboratory-scale oven for heat treatment. The procedure of wet and dry mechanical processing (abrasion) is used to separate the EVA from the glass and semiconductor material in thin-film components. Because of the more intricate structure of thin film panels, the delamination process takes a little longer for CdTe PV panels (Isherwood, 2022). However, material separation for thin films is a multi-step process with multiple moving parts. Abrasion is a wet mechanical process that uses friction and shear forces on the surface of the particles to be separated. Thin film fragments decompose into glass, semiconductors, and EVA as they wear. Glass and EVA are sifted during the sieving process used for this product. Substances finer than 150 μm, such as glass, are floated. The product then produces metal compounds, which are eliminated by dry etching or leaching. However, material separation for thin films is a multi-step process with multiple moving parts (Maani et al., 2020).

5.3. Challenges and future outlook

The future of PV solar panel recycling lies in a combination of physical and chemical technologies, as well as the use of light, water, and biodegradable auxiliaries (Palitzsch & Loser, 2018). Design for Recycling (DfR) and Design for Durability (DfD) are crucial in identifying optimal materials and geometries for more efficient recycling (Calì et al., 2022). The resource efficiency of PV recycling processes can be significantly improved, with high-efficiency processes able to recycle up to 83% of the waste panel (Ardente et al., 2019). The widespread adoption of advanced recycling techniques for PV solar panels faces several challenges. These include technological complexities, inadequate infrastructure, and economic hurdles (Gerold & Antrekowitsch, 2024). While proven recycling technologies exist, they need to be made more efficient and less complex, with reduced energy requirements and chemical use. The lack of economic viability and unfavorable policies also hinder the recycling process (Tao & Yu, 2015). The disposal of end-of-life PV modules in landfills or bulk recycling facilities can lead to environmental issues,

highlighting the need for high-value closed-loop recycling (Yu et al., 2022). The impending surge in PV waste, combined with inefficient recycling technologies, poses a significant problem (Peplow, 2022). To address these challenges, concerted action is needed to drive the development of efficient and sustainable PV module recycling practices (Gerold & Antrekowitsch, 2024). The importance of reducing recycling costs and environmental impacts, while maximizing material recovery was emphasized by (Heath et al., 2020). This is echoed by (Xu et al., 2018) , who calls for the development of economically feasible and non-toxic recycling technologies. Both authors stress the need for adaptable recycling infrastructure to keep pace with technological advancements. (Tao & Yu, 2015) and (Lunardi et al., 2018) highlight the potential of recycling pathways and processes, but note the challenges in terms of process efficiency, energy requirements, and economic viability. They also emphasize the importance of regulatory frameworks and producer responsibility to support the PV recycling industry. These studies collectively point to the need for further research and development in the areas of cost-effective and environmentally friendly recycling technologies, efficient collection networks, and supportive regulatory frameworks.

6. CONCLUSIONS

In order to the development of photovoltaics to take place, a low production cost will have to be achieved given that there are plenty of cheap common energy sources available. The transition to a low carbon energy paradigm is also an important challenge for the environmental and economic sustainability of the PV supply chain, particularly at the module's end-of-life phase. At the same time, by managing photovoltaic modules at an end of its useful life, it will be possible to make substantial progress towards a Sustainable Solar Industry. It shall also ensure that appropriate waste treatment technologies and recycling and recovery strategies are adopted in relation to the decommissioning of photovoltaic power plants. Due to the growing use of PV panels and their production capacities, waste from these panels is expected to be a key issue within 10 years. This will make it more important than ever that they are recycled. Reprocessing is therefore likely to significantly improve the current situation, when PV modules are able to function for a period of 25–30 years without deterioration. Valuable materials are thrown in the landfill immediately after PV panels are disposed of. Significant profits can be obtained from recovering rare materials like tellurium and indium, precious resources like copper, silver, aluminum, silicon, and glass, and hazardous materials like lead, selenium, and cadmium, depending on their economic viability. The investigation concludes that the world should not become a dumping ground for photovoltaic panels over the next few years. The overview shows that careful planning for recycling will become indispensable as the most popular photovoltaic panels are approaching their end of life in the coming years.

REFERENCES

IEA (2022). *Special Report on Solar PV Global Supply Chains*. Paris, OECD Publishing. https://doi.org/10.1787/9e8b0121-en

Ardente, F., Latunussa, C. E., & Blengini, G. A. (2019, May). Resource efficient recovery of critical and precious metals from waste silicon PV panel recycling. *Waste Management*, 91, pp. 156–167. https://doi.org/10.1016/j.wasman.2019.04.059

Artaş, S. B., Kocaman, E., Bilgiç, H. H., Tutumlu, H., Yağlı, H., & Yumrutaş, R. (2023, June). Why PV panels must be recycled at the end of their economic life span? A case study on recycling together with the global situation. *Process Safety and Environmental Protection*, 174, pp. 63–78. https://doi.org/10.1016/j.psep.2023.03.053

Bouabdelli, M. W., Rogti, F., Maache, M., & Rabehi, A. (2020). Performance enhancement of CIGS thin-film solar cell. *Optik*, 216 (March), 164948. https://doi.org/10.1016/j.ijleo.2020.164948

Calì, M., Hajji, B., Nitto, G., & Acri, A. (2022). The Design Value for Recycling End-of-Life Photovoltaic Panels. *Applied Sciences*, 12 (18), 9092, https://doi.org/10.3390/app12189092

Chen, H., Chang, L., Jeng, M., & Lai, C. (2011). Solid-State Electronics Characterization of laser carved micro channel polycrystalline silicon solar cell. *Solid State Electronics*, 61 (1), pp. 23–28. https://doi.org/10.1016/j.sse.2011.02.005

Chowdhury, M. S., Rahman, K. S., Chowdhury, T., Nuthammachot, N., Techato, K., Akhtaruzzaman, M., Tiong, S. K., Sopian, K., & Amin, N. (2020). An overview of solar photovoltaic panels' end-of-life material recycling. *Energy Strategy Reviews*, 27, 100431. https://doi.org/10.1016/j.esr.2019.100431

Corcelli, F., Ripa, M., & Ulgiati, S. (2017). End-of-life treatment of crystalline silicon photovoltaic panels. An emergy-based case study. *Journal of Cleaner Production*, Vol. 161, pp. 1129–1142, https://doi.org/10.1016/j.jclepro.2017.05.031

D'Adamo, I., Miliacca, M., & Rosa, P. (2017). Economic Feasibility for Recycling of Waste Crystalline Silicon Photovoltaic Modules. *International Journal of Photoenergy*, Vol. 2017, Article ID 4184676, p. 6. https://doi.org/10.1155/2017/4184676

El-Fayome, E., Abdelhamed, M. A., El-Shazly, A., Abouelatta, M., & Zekry, A. (2023). End Of Life Management Of Solar Panels. *40th National Radio Science Conference (NRSC)*, Giza, Egypt, 2023, pp. 286–293, https://doi.org/10.1109/NRSC58893.2023.10152958

European Commission (2011). *Study on photovoltaic panels supplementing the impact assessment for a recast of the WEEE directive.* Paris, France, Bio Intelligence Service, 86 p.

Hocine, L., & Samira, K. M. (2019). Optimal PV panel's end-life assessment based on the supervision of their own aging evolution and waste management forecasting. *Solar Energy*, 191, pp. 227–234. https://doi.org/10.1016/j.solener.2019.08.058

Kurinec, S. K. (ed.) (2018, December 3). *Emerging Photovoltaic Materials: Silicon & Beyond.* Beverly, Massachusetts, USA, Scrivener Publishing LLC, https://doi.org/10.1002/9781119407690

Fernandes, C. A. F., Torres, J. P. N., Morgado, M., & Morgado, J. A. (2016, September). Aging of solar PV plants and mitigation of their consequences. *2016 IEEE International Power Electronics and Motion Control Conference (PEMC)*, Varna, Bulgaria, pp. 1240–1247, https://doi.org/10.1109/epepemc.2016.7752174

Gielen, Dolf, Gorini, Ricardo, Asmelash, Elisa, Prakash, Gayathri, Leme, Rodrigo, (2019). *Future of Solar Photovoltaic: Deployment, investment, technology, grid integration and socio-economic aspects.* A Global Energy Transformation: paper. Abu Dhabi, International Renewable Energy Agency.

Gerold, E., & Antrekowitsch, H. (2024). Advancements and Challenges in Photovoltaic Cell Recycling: A Comprehensive Review. *Sustainability*, 16 (6), 2542. https://doi.org/10.3390/su16062542

Gökhan, Y., Etem, A., & Ceylan, İ. (2020). Investigation of life cycle CO_2 emissions of the polycrystalline and cadmium telluride PV panels. *Environmental Nanotechnology , Monitoring & Management*, Vol. 14 (June), 100343. https://doi.org/10.1016/j.enmm.2020.100343

Heath, G. A., Silverman, T. J., Kempe, M., Deceglie, M., Ravikumar, D., Remo, T., Cui, H., Sinha, P., Libby, C., Shaw, S., Komoto, K., Wambach, K., Butler, E., Barnes, T., & Wade, A. (2020). Research and development priorities for silicon photovoltaic module recycling to support a circular economy. *Nature Energy*, 5 (7), pp. 502–510. https://doi.org/10.1038/s41560-020-0645-2

Huang, W. H., Shin, W. J., Wang, L., Sun, W. C., & Tao, M. (2017). Strategy and technology to recycle wafer-silicon solar modules. *Solar Energy*, 144, pp. 22–31. https://doi.org/10.1016/j.solener.2017.01.001

Isherwood, P. J. M. (2022). Reshaping the Module: The Path to Comprehensive Photovoltaic Panel Recycling. *Sustainability*, 14 (3), 1676, https://doi.org/10.3390/su14031676

Krebs, L., & Frischknecht, R. (2022). *Resource Use Footprints of Residential PV Systems*. IEA PVPS Task 12, International Energy Agency (IEA) PVPS Task 12, Report T12-22:2022. www.iea-pvps.org

Lunardi, M. M., Alvarez-Gaitan, J. P., Bilbao, J. I., & Corkish, R. (2018). A Review of Recycling Processes for Photovoltaic Modules. In: *Solar Panels and Photovoltaic Materials.* InTech, https://doi.org/10.5772/intechopen.74390

Maani, T., Celik, I., Heben, M. J., Ellingson, R. J., & Apul, D. (2020). Environmental impacts of recycling crystalline silicon (c-SI) and cadmium telluride (CDTE) solar panels. *Science of the Total Environment*, 735, 138827. https://doi.org/10.1016/j.scitotenv.2020.138827

Müller, A., Wambach, K., & Alsema, E. (2006). Life Cycle Analysis of Solar Module Recycling Process. *MRS Proceedings*, 895. https://doi.org/10.1557/proc-0895-g03-07

Mahmoudi, S., Huda, N., Alavi, Z., Islam, T., & Behnia, M. (2019). Resources , Conservation & Recycling End-of-life photovoltaic modules: A systematic quantitative literature review. *Resources, Conservation & Recycling*, 146 (October 2018), pp. 1–16. https://doi.org/10.1016/j.resconrec.2019.03.018

Nykyruy, L. I., Yavorskyi, R. S., Zapukhlyak, Z. R., Wisz, G., & Potera, P. (2019). Evaluation of CdS/CdTe thin film solar cells: SCAPS thickness simulation and analysis of optical properties. *Optical Materials*, 92 (April), pp. 319–329. https://doi.org/10.1016/j.optmat.2019.04.029

Paiano, A. (2015). Photovoltaic waste assessment in Italy. *Renewable and Sustainable Energy Reviews*, 41, pp. 99–112. https://doi.org/10.1016/j.rser.2014.07.208

Palitzsch, W., & Loser, U. (2018). Integrated PV-Recycling-More Efficient, More Effective. *2017 IEEE 44th Photovoltaic Specialist Conference (PVSC)*, pp. 2272–2274, Washington D.C., USA, https://doi.org/10.1109/pvsc.2017.8521517

Peplow, M. (2022). Solar Panels Face Recycling Challenge. *ACS Central Science*, 8 (3), pp. 299–302. https://doi.org/10.1021/acscentsci.2c00214

Shin, J., Park, J., & Park, N. (2017). A method to recycle silicon wafer from end-of-life photovoltaic module and solar panels by using recycled silicon wafers. *Solar Energy Materials and Solar Cells*, 162 (September 2016), pp. 1–6. https://doi.org/10.1016/j.solmat.2016.12.038

Smith, Y. R., & Bogust, P. (2018). Review of Solar Silicon Recycling. In: Sun, Z. et al.: *Energy Technology 2018.* TMS 2018. The Minerals, Metals & Materials Series. Cham, Springer, pp. 463–470. https://doi.org/10.1007/978-3-319-72362-4_42

Tao, J., & Yu, S. (2015). Review on feasible recycling pathways and technologies of solar photovoltaic modules. *Solar Energy Materials and Solar Cells*, 141, pp. 108–124. https://doi.org/10.1016/j.solmat.2015.05.005

Vellini, M., Gambini, M., & Prattella, V. (2017). Environmental impacts of pv technology throughout the life cycle: Importance of the end-of-life management for si-panels and cdte-panels. *Energy*, Vol. 138, pp. 1099–1111, https://doi.org/10.1016/j.energy.2017.07.031

Weckend, S., Wade, A., and Heath, G. A. (2016). *End of Life Management: Solar Photovoltaic Panels.* United States: N. p. Web. https://doi.org/10.2172/1561525.

Xu, Y., Li, J., Tan, Q., Peters, A. L., & Yang, C. (2018). Global status of recycling waste solar panels: A review. *Waste Management*, 75, pp. 450–458. https://doi.org/10.1016/j.wasman.2018.01.036

Yıldız, G., Çalış, B., Gürel, A. E., & Ceylan, L. (2020). Investigation of life cycle CO_2 emissions of the polycrystalline and cadmium telluride PV panels. *Environmental Nanotechnology, Monitoring & Management*, 14, 100343. https://doi.org/10.1016/j.enmm.2020.100343

Yi, Y. K., Kim, H. S., Tran, T., Hong, S. K., & Kim, M. J. (2014). Recovering valuable metals from recycled photovoltaic modules. *Journal of the Air & Waste Management Association*, 64 (7), pp. 797–807. https://doi.org/10.1080/10962247.2014.891540

Yue, D., You, F., & Darling, S. B. (2014). Domestic and overseas manufacturing scenarios of silicon-based photovoltaics: Life cycle energy and environmental comparative analysis. *Solar Energy*, 105, pp. 669–678. https://doi.org/10.1016/j.solener.2014.04.008

Yu, H. F., Hasanuzzaman, M., Rahim, N. A., Amin, N., & Nor Adzman, N. (2022). Global Challenges and Prospects of Photovoltaic Materials Disposal and Recycling: A Comprehensive Review. *Sustainability*, 14 (14), 8567, https://doi.org/10.3390/su14148567

Geosciences and Engineering, Vol. 12, No. 1 (2024), pp. 119–124.
https://doi.org/10.33030/geosciences.2024.01.008

ANALYSIS OF THE EARTHQUAKE IMPACT ON URBAN TUNNELS USING MODELING IN PHASE 2 SOFTWARE

MAHDI DASHTI[1]*, ZOLTÁN VIRÁG[2]
[1*]*Institute of Mining and Energy, University of Miskolc;*
mahdi.dashti@student.uni-miskolc.hu
[2]*Institute of Mining and Energy, University of Miskolc;*
zoltan.virag@uni-miskolc.hu
[2]*https://orcid.org/0000-0003-2259-8878*

Abstract: This article presents a comprehensive survey of the seismic impact experienced by urban tunnels, with a specific focus on the Line 7 of the Tehran Metro. Employing finite element software during Phase 2 of modeling, the study investigates the potential effects of seismic activity on tunnel stability. The research involves a meticulous examination of concurrent factors, primarily alterations in earthquake acceleration values and adjustments to the depth of the tunnel. The findings reveal that effective maintenance practices within the underground Metro Stations play a crucial role in minimizing the seismic impact on tunnel stability. The study underscores that the key mitigation strategy involves enhancing the structural integrity and reinforcing the conditions under which the tunnel is maintained. By doing so, the article suggests that urban planners and engineers can contribute significantly to the overall resilience and safety of underground metro systems in seismic-prone regions, such as Tehran.

Keywords: *Earthquake, Urban tunnels, Tehran Metro Line 7, Modeling, Phase 2, Seismics*

1. INTRODUCTION

Nowadays, human activities (e.g., towers and buildings constructions, tunneling and underground excavations, traffic) have been increasing due to the need for development (Tavanaei et al., 2020). The extraction and transportation of rock, particularly in mining and tunneling operations, are perceived as potential triggers for seismic activity, potentially leading to slip along fault lines (Kocharyan et al., 2022). The study on the vulnerability of tunnels under seismic loading has been of great interest among researchers under various geological conditions (Srivastav and Satyam, 2020). The construction of earthquake-resistant underground structures requires an understanding of how the propagating seismic waves, as caused by earthquakes. in this case, interact with an underground system such as tunnels. For most underground structures, the underlying rock's inertia is large relative to the structural inertia and hence the tunnel's seismic reaction is determined by the surrounding soil or rock mass response. However, a surface structure's seismic reaction is governed by its inertial effects (Forcellini, 2017; Forcellini, 2018; Forcellini, 2019). Previous natural disasters, including earthquakes, had a significant impact on transport networks with severe consequences for the users and supply chain. The resilience

assessment of critical assets such as tunnels is of paramount importance for increasing safety and maintaining their functionality in seismic-prone areas (Huang et al., 2022). The study has been conducted using Rocscience's Phase 2 software which has been used frequently to understand various case scenarios related to the seismic response of tunnels (Sun and Dias, 2019). We seek to provide valuable insights into the dynamic interactions between seismic forces and tunnel structures. Furthermore, our objective is to identify and emphasize the critical role of effective maintenance practices within the underground Metro Stations in mitigating the seismic impact on tunnel stability.

2. MATERIALS AND METHODS

The Phase 2 software, specifically in its 8.1 version, necessitates specific data inputs to facilitate the modeling process. Phase 2 offers robust tools for simulating dynamic loads and seismic events. Its ability to model the complex interactions between seismic waves and geological materials is crucial for accurate seismic analysis, these models ensure realistic simulation of ground response during an earthquake. Therefore, for this situation of the project, our best choice was Phase 2.

The required data encompasses various parameters and specifications essential for accurately representing the conditions and characteristics within the system being analyzed. This inclusive data set serves as the foundational information that the software utilizes to generate a comprehensive and detailed model, enabling a thorough exploration and evaluation of the targeted subject matter. For numerical modeling, we need to collect the following data and apply them in the right order in the software:

- The "Define Material" stage: Specific Gravity of Soil, Poisson's Ratio, Friction Angle, Cohesion, Young's Modulus, Shear Strength.
- The "Define Liner" stage: Liner Type, Young's Modulus, Tensile Strength, Specific Gravity, Compressive Strength, Liner Thickness, Poisson's Ratio.
- The "Define Joint" stage: Normal Hardness, Shear Hardness.
- The "Define Bolt" stage: Bolt Diameter, Young's Modulus, Tensile Strength, Bolt Spacing.

The required data were obtained from the engineering geology unit specifications (ET) differentiated in soil layers along the tunnel route. To assess the earthquake impact, a station from Tehran Metro Line 7 was selected. In this station, a tunnel with a diameter of 9.2 m is located at a depth of 19.6 m. In each stage, the earthquake acceleration is increased by 0.1 g, and the induced changes in the vicinity of the tunnel are examined. The tunnel, excavated in ET-5 soil, is composed of silty and clayey materials with the addition of sand, characterized as follows:

- Effective Cohesion: c = 31 KPa
- Effective Internal Friction Angle: $\Phi = 28°$
- Poisson's Ratio: $\upsilon = 0.35$

To mitigate the boundary effects on the results, the side boundaries of the tunnel are considered to be 10 times the tunnel radius. It should be noted that the tunnel radius is 4.6 m.

3. FINDINGS AND RESULTS

Considering the given information, a geometric model of the tunnel was created using Phase 2 software, as depicted in *Figure 1*. Subsequently, the created model underwent analysis under various earthquake accelerations, and the obtained results were examined.

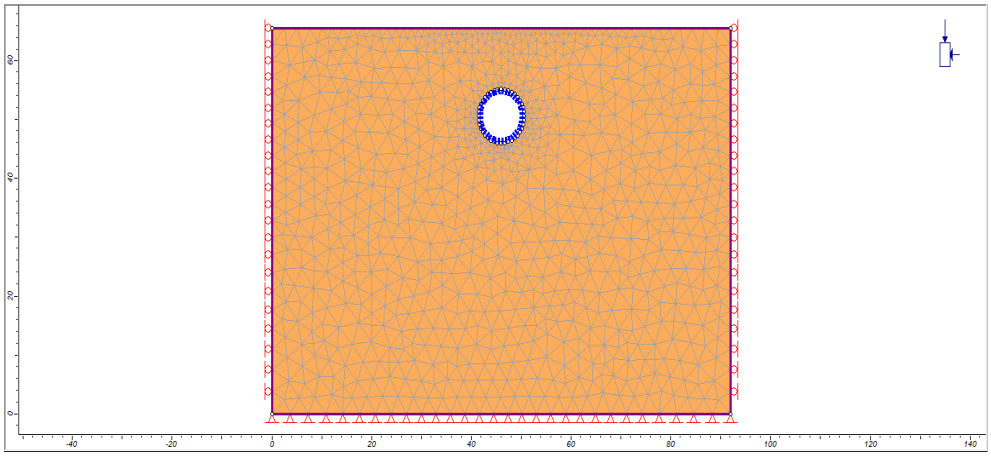

Figure 1

The model created by Phase 2 for the tunnel with a depth of 19.6 m was analyzed without the influence of an earthquake

In the subsequent stages, the earthquake acceleration is increased by 0.1 g, and the results are examined under accelerations 0.1 g, 0.2 g, 0.3 g, and 0.4 g. The results of the earthquake impact on the stability of the tunnel at a depth of 19.6 m are presented in *Table 1*.

Table 1

The results of the earthquake impact on the stability of the tunnel located at a depth of 19.6 m

The imposed acceleration	Minimum safety factor	Maximum displacement [cm]	Maximum share force [N]	Maximum bending moment [kNm]
without influence	0.95	0.89	91.078	202.44
0.1	0.95	0.97	106.33	239.43
0.2	0.63	1.33	107.59	241.05
0.3	0.63	0.489	109.68	245.2
0.4	0.63	0.63	114.01	256.45

To investigate whether the depth of the tunnel influences the earthquake's impact on tunnel stability, an example is considered for analysis at a depth of 15 m, based on the design of Tehran Metro Line 7 tunnel. The details of this analysis will be discussed further.

Analysis of the problem at a depth of 15 m: considering the provided information and utilizing the Phase 2 software, a geometric model of the tunnel was created as depicted in *Figure 2*. Subsequently, the created model underwent analysis under various earthquake accelerations, and the obtained results were examined.

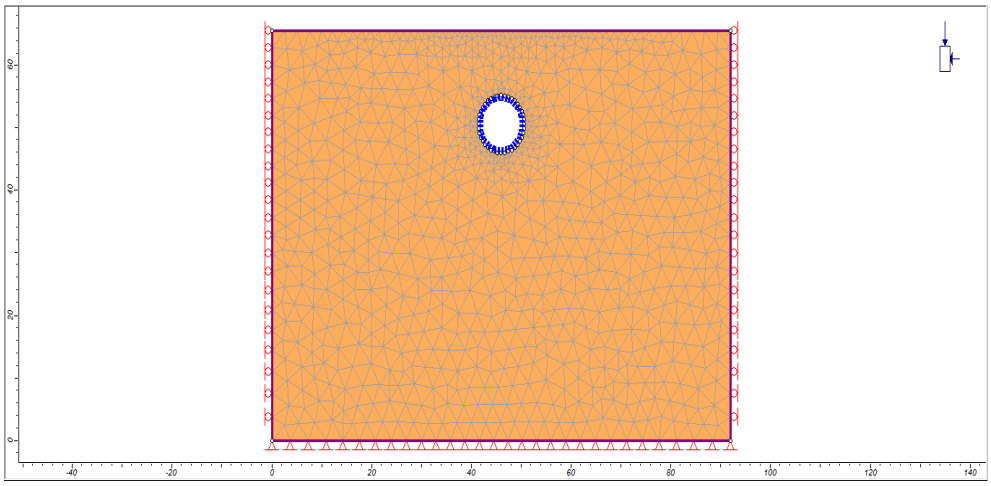

Figure 2
The model created by Phase 2 for the tunnel with a depth of 15 m and earthquake acceleration of 0.1 g

Similar to the analysis at a depth of 19.6 m, in the subsequent stages, the earthquake acceleration is increased by 0.1 g, and the results are examined under accelerations 0.1 g, 0.2 g, 0.3 g, and 0.4 g. The results of the earthquake impact on the stability of the tunnel at a depth of 19.6 m are presented in *Table 2*.

Table 2
The results of the earthquake impact on the stability of the tunnel placed at a depth of 15 m

The imposed acceleration	Minimum safety factor	Maximum displacement [cm]	Maximum share force [N]	Maximum bending moment [kNm]
without influence	0.95	0.73	80.941	183.95
0.1	0.95	0.899	81.968	185.22
0.2	0.95	1.28	83.101	186.46
0.3	0.95	0.49	85.871	191.42
0.4	0.95	0.63	89.368	200.77

For the assessment of tunnel stability under various seismic intensities, a circular tunnel with a diameter of 9.2 m at a depth of 15 m in the soil of Tehran was modeled using the finite element method in the Phase 2 software. Based on this, the variations in displacement, safety factor, shear force, and flexural moment (induced in the support system) were examined under different earthquake accelerations. It was observed that at a depth of 15 m, the earthquake intensity had no effect on the safety factor, and the safety factor remained constant. The maximum displacement occurred at an earthquake intensity of 0.2 g, and with increasing earthquake intensity, both the maximum shear force and the maximum flexural moment also increased. This assessment was also conducted for depths of 25 and 30 m, separately, and the results were nearly similar to those at a depth of 15 m, except for the maximum displacement, which occurred at an earthquake intensity of 0.1g for depths of 25 and 30 m.

4. DISCUSSION AND CONCLUSIONS

In summary, based on the obtained results, it seems that earthquake occurrences have not significantly affected the stability of tunnels, However, in urban tunnels, even minor displacements could potentially lead to considerable damage, especially at the surface. Therefore, it is highly advisable to employ modeling and predictive techniques to anticipate and mitigate potential displacements in these areas.

Considering the variations in shear forces and flexural moments imposed on the support system, it can be concluded that in seismically active areas, the tunnel maintenance system should be designed and implemented with greater strength and fundamentality. The complex interaction of geological forces in seismically active areas requires a careful investigation of the effects on tunnel structures. The need for a comprehensive approach to tunnel maintenance is highlighted by the fluctuations in flexural moments and shear stresses that the support system experiences during seismic events. Given that these forces have the potential to place significant strain on the infrastructure, it is necessary to improve the structural stability and fundamental strength of the tunnel maintenance system. This supports the tunnels' immediate stability and establishes a foundation for long-term resilience against the unpredictability of the forces released by seismic activity.

Additionally, the dynamic character of seismic forces should be considered in the design of the tunnel maintenance system, which calls for a forward-looking strategy. Infrastructure in seismically active regions must be able to endure both the immediate effects of seismic waves and any possible aftershocks. It becomes critical to put in place a stronger maintenance system since it acts as a preventative precaution against possible harm and guarantees the tunnel structures' long-term survival. Strong implementation and strategic planning are essential for protecting tunnel infrastructure from the intricate problems that seismicity presents. The study focused on a specific tunnel geometry, which may limit the applicability of the findings to other types of tunnels. Expanding the study to include a wider variety of tunnel designs could provide a more comprehensive understanding of tunnel behavior under diverse conditions.

REFERENCES

Forcellini D. (2017). Cost assessment of isolation technique applied to a benchmark bridge with soil structure interaction. *Bulletin of Earthquake Engineering*, Vol. 15, No. 1, pp. 51–69. https://doi.org/10.1007/s10518-016-9953-0

Forcellini D. (2018). Seismic assessment of a benchmark based isolated ordinary building with soil structure interaction. *Bulletin of Earthquake Engineering*, Vol. 16, No. 5, pp. 2021–2042. https://doi.org/10.1007/s10518-017-0268-6

Forcellini D. (2019). Numerical simulations of liquefaction on an ordinary building during Italian (20 May 2012) earthquake. *Bulletin of Earthquake Engineering*, Vol. 17, No. 9, pp. 4797–4823. https://doi.org/10.1007/s10518-019-00666-5

Huang, Z., Zhang, D., Pitilakis, K., Tsinidis, G., Huang, H., Zhang, D., Argyroudis, S. (2022) Resilience assessment of tunnels: Framework and application for tunnels in alluvial deposits exposed to seismic hazard. *Soil Dynamics and Earthquake Engineering*, Vol. 162, 107456, p. 13. https://doi.org/10.1016/j.soildyn.2022.107456

Kocharyan, G., Qi, C., Kishkina, S., Kulikov, V. (2022). Potential triggers for large earthquakes in open-pit mines: A case study from Kuzbass, Siberia. *Deep Underground Science and Engineering*, Vol. 1, No. 2, pp. 101–115. https://doi.org/10.1002/dug2.12028

Srivastav, A., Satyam, N. (2020). Understanding the impact of the earthquake on circular tunnels in different rock mass: a numerical approach. *Innovative Infrastructure Solutions*, Vol. 5, 32, p. 9. https://doi.org/10.1007/s41062-020-0278-0

Sun, Q. Q., Dias, D. (2019). Assessment of stress relief during excavation on the seismic tunnel response by the pseudo-static method. *Soil Dynamics and Earthquake Engineering*, Vol. 117, pp. 384–397. https://doi.org/10.1016/j.soildyn.2018.09.019 .

Tavanaei, F., Hassanpour, J., Memarian, H. (2020). Urban noises and earthquakes effects on dynamic slope stability – a case study: Arash-Esfandiar tunnel. *International Journal of Geotechnical Engineering*, Vol. 14, No. 4, pp. 420–427. https://doi.org/10.1080/19386362.2018.1433347

Geosciences and Engineering, Vol. 12, No.1 (2024), pp.125–138.
https://doi.org/10.33030/geosciences.2024.01.009

EDGE DETECTION OF TOMOGRAPHIC IMAGES USING TRADITIONAL AND DEEP LEARNING TOOLS

TÜNDE EDIT DOBRÓKA[1], ISTVÁN SZŰCS[2], MIHÁLY DOBRÓKA[3*]
[1]*Faculty of Earth and Environmental Sciences and Engineering, University of Miskolc;*
afkdobroka@uni-miskolc.hu
[2]*Faculty of Engineering and Information Technology, University of Pécs;*
dr.szucsistvan@t-online.hu
[3*]*Department of Geophysics, University of Miskolc;*
dobroka@uni-miskolc.hu

Abstract: Edge detection is regularly used as a fundamental operation for correctly identifying and measuring some required features. In a grey-level image, an area where the grey-level value moves from a high value to a low value or vice versa is considered an edge. Edges are indicative of a boundary between an object and a background or between two objects. Consequently, edge detection in earth sciences is an important tool for locating geological features and determining their shapes and sizes. Edge detection usually forms a part of the geophysical interpretation or inversion procedure. Seismic tomography is a straightforward field of applying edge detection because the tomogram can be directly considered as an image. In the tomographic reconstruction of seismic travel time data, care must be taken to keep the propagation of data errors to the model space under control. The noise – especially the outliers in the data sets – can cause appreciable distortions in the tomographic imaging. To reduce the noise sensitivity well-developed tomography algorithms can be used. On the other hand, the quality of the tomogram can further be improved by using image processing tools. This is especially important in edge detection, as it is extremely sensitive to noise. In the paper, we present two ways to find robust edge detection. At first, remaining in the framework of traditional image processing a robust Cauchy–Steiner filter is used to improve the quality of edge detection in tomographic images. In the second part of the paper Deep Learning algorithm developed for edge detection is shown and investigating its noise sensitivity the robustness of the method is demonstrated.

Keywords: *image processing, edge detection, seismic tomography, Deep Learning*

1. INTRODUCTION

The seismic tomography methods are used to reconstruct the velocity distribution for the investigated part of the Earth such that the travel time data should agree with measurements. In most of the methods, this is done by solving a least-squares (LSQ) problem. In tomography, the least-squares problems are frequently solved by the so-called row action methods (Nolet, 1987; Herman, 2009) as the Algebraic Reconstruction Technique (ART) or Simultaneous Iterative Reconstruction Technique (SIRT). On the other hand, it is well-known that the least-squares solution is very sensitive to the non-Gaussian nature of the noise distribution, especially sparsely distributed large errors,

i.e. outliers in the dataset. So robust estimation methods should be used. One of the most frequently used robust optimization procedures is the Least Absolute Deviation (LAD) method using the L_1 norm to characterize the misfit between the observed and predicted data. An efficient algorithm was developed for its tomographic use by Scales et al. (1988). Another possibility to address the question of statistical robustness is the use of the Cauchy criterion (Amundsen, 1991). In this case, the misfit function is the weighted norm of the deviation between the observed and predicted data vectors (the weights are the so-called Cauchy weights with a priori known scale parameters). In the framework of the Most Frequent Value method (MFV), Steiner (1988) developed a more flexible procedure for determining the weights, in which the scale parameters are automatically derived from the data set. Combining the two approaches the weights (called Cauchy–Steiner weights) are applied in an iteratively reweighted least-squares procedure, resulting in an efficient outlier reduction. In the paper the tomograms given by traditional SIRT and its improved version, the W-SIRT [in which Cauchy–Steiner weights are applied to produce robust tomographic reconstruction (Dobróka et al., 2014)] is applied. The resulting tomograms are utilized for robust edge detection. Doing this the results given by the traditional image processing tools (improved by using Cauchy–Steiner weights) are compared to those produced by a Deep Learning (DL) procedure.

In the first part of the paper, a robust image processing tool – called Steiner filter – is introduced, in which MFV-weights are applied for further reduction of the influence of outliers. To analyze the noise reduction capability of the new filter medium-sized tomographic images (containing 100 × 100 pixels) are used. The same datasets are applied to show the efficiency of noise rejection capacity in edge detection of the DL procedure. In this second part, we applied the U-Net Convolutional Network architecture, which is a widely used deep learning tool developed for image segmentation. After some necessary modifications, the procedure is applicable to edge detection with improved noise reduction capacity.

2. EDGE DETECTION USING IMAGE PROCESSING TOOLS

In a 2D case, the tomogram is an array of seismic velocity or slowness data along a (usually) regular grid. In an element of the grid, the $f(i,j)$ value of the physical quantity (velocity or absorption coefficient) is constant. Here $(i = 1,\dots N, j = 1,\dots,M)$, where N, M are the tomogram's sizes in grid cell units. Considering the cell as a pixel with the constant (of the physical quantity) in it, a straightforward analogy can be declared between the tomogram and an image. Thus, the methods of image processing are obviously can be applied to improve the quality of tomographic pictures. To filter the tomogram one can define a 2D window containing *(2k+1)x(2k+1)* pixels (*k=1,2,…*) around the (i,j) pixel symmetrically. The middle of the window is placed to the (i,j) pixel of the tomogram which finds the filtered value given as

$$g(i,j) = \sum_{u=-k}^{k} \sum_{v=-k}^{k} T(u,v) f(i-u, j-v) \tag{1}$$

where $T(u,v)$ is the filter function (kernel or mask) $(i = 1,\dots N-k, j = 1,\dots,M-k)$. In noise reduction, the smoothing filters

$$\boldsymbol{T}_1 = \frac{1}{9}\begin{bmatrix}1 & 1 & 1\\ 1 & 1 & 1\\ 1 & 1 & 1\end{bmatrix} \quad \text{and} \quad \boldsymbol{T}_2 = \frac{1}{16}\begin{bmatrix}1 & 2 & 1\\ 2 & 4 & 2\\ 1 & 2 & 1\end{bmatrix} \tag{2}$$

are frequently used with the masks (in the 3 × 3 case), where $\boldsymbol{T}_1$ and $\boldsymbol{T}_2$ give the arithmetic-, and the binomial mean, respectively. In image processing, the median filter is extensively used in which the filtered value is the median of the data in the window defined by the mask

$$g(i,j) = median\{f(i,j,u,v)\}, (u,v = -P,\ldots,P) \tag{3}$$

P being the window's size. A more general filter can give a weighted average of the noisy pixel values

$$\boldsymbol{T}_w = \frac{1}{\sum_{u,v=1}^{3} w_{u,v}}\begin{bmatrix}w_{11} & w_{12} & w_{13}\\ w_{21} & w_{22} & w_{23}\\ w_{31} & w_{32} & w_{33}\end{bmatrix} \tag{4}$$

In our present investigation, the *Steiner filter* is introduced with the weights

$$w_k = \frac{\varepsilon^2}{\varepsilon^2 + (d_k - M)^2},\ (k = 3(v-1)+u) \tag{5}$$

in Equation 4, where the ε and M are the scale-, and location parameters calculated in an iterative procedure with

$$M_{j+1} = 3\frac{\sum_{k=1}^{N}\frac{d_k}{\left(\varepsilon_j^2+(d_k-M_j)\right)^2}}{\sum_{k=1}^{N}\left(\frac{1}{\varepsilon_j^2+r_k^2}\right)^2}, \varepsilon_{j+1}^2 = 3\frac{\sum_{k=1}^{N}\frac{r_k^2}{\left(\varepsilon_j^2+r_k^2\right)^2}}{\sum_{k=1}^{N}\left(\frac{1}{\varepsilon_j^2+r_k^2}\right)^2} \tag{6}$$

in the *j*-th iteration ($r_k = d_k - M_j$). The starting value for the location parameter is the mean of the data (in the mask), while ε is given as $\varepsilon_0 \leq \sqrt{3}(r_{max} - r_{min}/2)$ (Steiner, 1988).

2.1. Application of the Steiner filter in noise reduction of seismic tomography images

For the numerical experiments, a rectangular test area of 100 × 100 cells was defined *(Figure 1)*. The model contains three anomalies of the velocity 5 km/s (red color) located in a homogeneous background of 4 km/s velocities (blue color). Sources and receivers were positioned along the x- and y-axis in an arrangement fulfilling the requirement of full tomographic ray coverage, thus the theoretical travel time data were computed along 60000 ray traces. To model quasi-measured data containing outliers, the theoretical travel times were contaminated with 1% Gaussian distributed noise and an extra 10% noise was added to a randomly selected 10% portion of the data. The tomographic reconstruction was made using the traditional Simultaneous

Iterative Reconstruction Technique (SIRT method) and its improved version, the W-SIRT robustified by using MFV weights (Dobróka, 2007). Instead of displaying the exact model, its SIRT reconstructed tomogram using the noise-free dataset is presented in *Figure 1*.

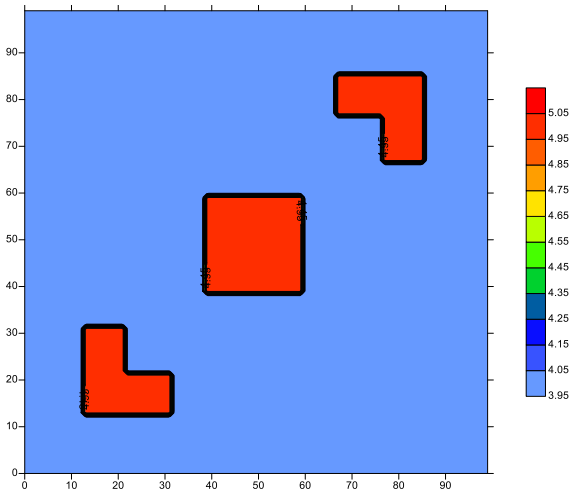

Figure 1

The model reconstructed by means of noise-free travel time data

The Simultaneous Iterative Reconstruction Technique is one of the most frequently used methods in seismic tomography. In the typical step of the algorithm, the arithmetic mean of the so-called ART correction belonging to the seismic rays crossing the *j*-th cell is calculated as

$$s_j^{(q+1)} = s_j^{(q)} + \frac{1}{Q_j}\sum_{i=1}^{Q_j}\frac{D_{ij}r_i^{(q)}}{\sum_k D_{ik}^2} \tag{7}$$

$s_j^{(q)}$ is the slowness of the *j*-th cell in the *q*-th iteration, Q_j denotes the number of rays crossing the *j*-th cell, $r_i^{(q)}$ means the difference between the *i*-th measured and calculated traveltime and D_{ij} is the ray section of the *i*-th ray in the *j*-th cell. If instead of this simple arithmetic mean, a weighted average of the ART corrections is used

$$s_j^{(q+1)} = s_j^{(q)} + \frac{1}{\sum_{l=1}^{Q_j} W_{ll}}\sum_{i=1}^{Q_j} W_{ii}\frac{D_{ij}r_i^{(q)}}{\sum_k D_{ik}^2}, \tag{8}$$

a new version of the SIRT algorithm can be defined. Using the Cauchy–Steiner weights given in *Equation 4*, a robust W-SIRT method can be defined (Dobróka and Szegedi, 2014; Dobróka and Kale, 2016).

To characterize the accuracy of the reconstruction the relative model distance

$$D = \sqrt{\frac{1}{M}\sum_{j=1}^{M}\left(\frac{s_j - s_j^{(0)}}{s_j^{(0)}}\right)^2} \tag{9}$$

was used. Here s_j and $s_j^{(0)}$ denotes the slowness in the j-th cell of the reconstructed picture and the model, respectively, M is the total number of cells. The tomograms given by the SIRT or W-SIRT methods contain the slowness data in each pixel, so it can be considered as a black-and-white image in which the grey level is the slowness (or velocity). Using this procedure the SIRT and W-SIRT tomograms were converted to jpg images of the size of 100 × 100 pixels. *Figures 2a* and *2b* show the tomograms (color-coded in displaying).

Utilizing *Equation 8*, the distance between the noise-free image *(Figure 1)* and the SIRT reconstructed noisy one *(Figure 2a)* is D = 0.0265. The image depicted in *Figure 2b* given by the W-SIRT method (using Steiner weights) is characterized by D = 0.0197 model distance. The improvement due to the use of the robust tomography method is 25.6%. It can be seen, that in the tomographic reconstruction of the data set containing outliers, the robust W-SIRT method has better noise reduction capability.

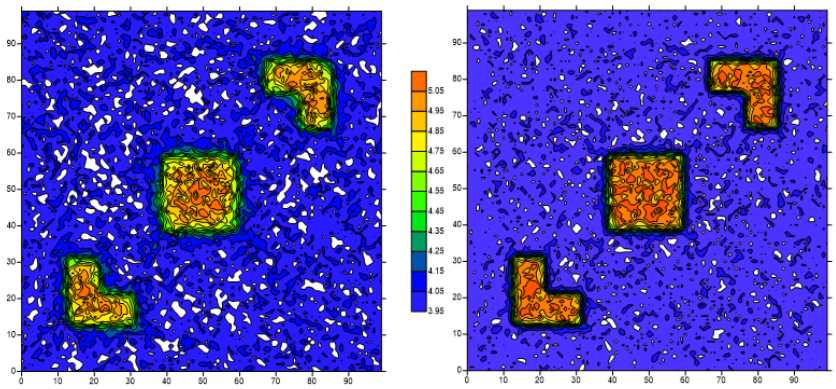

a) b)

Figure 2

The reconstruction of the noisy travel time data (including outliers) using a) SIRT and b) W-SIRT tomography methods

Figures 3a and *3b* show the effect of the Steiner filter on the reconstructed SIRT and W-SIRT images, respectively. The model distance between the noise-free and the Steiner-filtered SIRT reconstruction *(Figure 3a)* is D = 0.0232. Relative to *Figure 2a* an improvement of 12.5% is found due to the use of the Steiner filter. The same calculation gives D=0.0156 model distance in the case of the Steiner-filtered W-SIRT picture *(Figure 3b)* with 20.8% improvement due to the application of the Steiner filter. It can be seen that by using image processing tools, the quality of noisy

tomograms can further be improved. Our investigations show that the outlier reduction effect of the new Steiner filter is similar to that of the median filter.

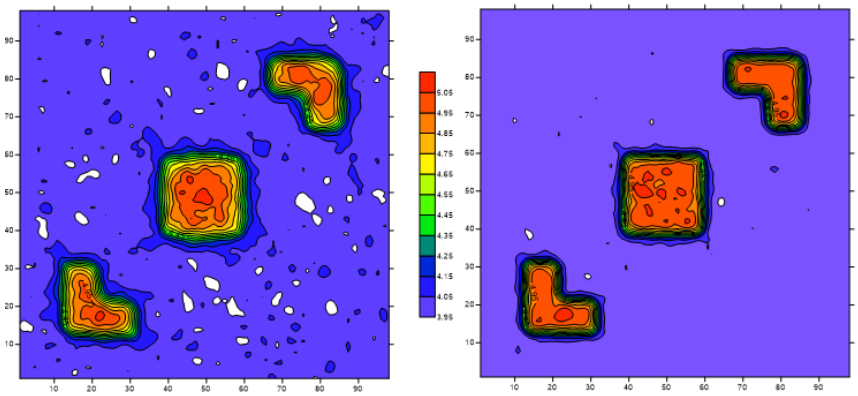

a) b)

Figure 3

The effect of the Steiner filter on a) SIRT and b) W-SIRT images

2.2. Application of the Steiner filter in edge detection of seismic tomography images

In seismic tomography, the geological structure is investigated using seismic travel time data. To support the interpretation of the tomographic result special transformations can be applied to the tomogram. It is a frequent problem to emphasize the borders of a certain geological structure (layer boundaries, fault, etc.). There are commonly used tools for edge detection in image processing: the Prewitt and Sobel operators.

The difference along the x and y-axis is calculated utilizing the convolution masks of the Prewitt operator as

$$D_x=\begin{bmatrix}-1 & 0 & 1\\ -1 & 0 & 1\\ -1 & 0 & 1\end{bmatrix}/3 \quad \text{and} \quad D_y=\begin{bmatrix}1 & 1 & 1\\ 0 & 0 & 0\\ -1 & -1 & -1\end{bmatrix}/3$$

It can be seen that the difference is calculated 3 times, and their arithmetic mean is used as a local difference. In the case of the Sobel operator, the difference is also calculated 3 times, but the binomial mean is used to characterize the local difference:

$$D_x=\begin{bmatrix}-1 & 0 & 1\\ -2 & 0 & 2\\ -1 & 0 & 1\end{bmatrix}/4 \quad \text{and} \quad D_y=\begin{bmatrix}1 & 2 & 1\\ 0 & 0 & 0\\ -1 & -2 & -1\end{bmatrix}/4$$

Using these convolution masks the change along the x-axis (approximates the x-derivative) can be calculated as

$$\boldsymbol{\partial_x(i,j)} = \sum_{\boldsymbol{u=-k}}^{\boldsymbol{k}} \sum_{\boldsymbol{v=-k}}^{\boldsymbol{k}} \boldsymbol{D_x(u,v) f(i-u, j-v)},$$
$$(\boldsymbol{i = 1, \ldots N-k, j = 1, \ldots, M-k}) \quad (10)$$

and similarly

$$\boldsymbol{\partial_y(i,j)} = \sum_{\boldsymbol{u=-k}}^{\boldsymbol{k}} \sum_{\boldsymbol{v=-k}}^{\boldsymbol{k}} \boldsymbol{D_y(u,v) f(i-u, j-v)},$$
$$(\boldsymbol{i = 1, \ldots N-k, j = 1, \ldots, M-k}) \quad (11)$$

with *k=(S-1)/2*, where *S* is the mask size. These quantities can be considered as the two components of the 2D gradient vector. Its direction gives the direction of the maximal change of the slowness function, while its absolute value (the edge gradient $\sqrt{\boldsymbol{\partial_x^2 + \partial_x^2}}$) defines the rate of the total change in the same direction.

In *Figure 4* the effect of the (edge gradient) Sobel operator is demonstrated on a test image ("Lena", frequently used in image processing). As it can be seen, on the homogeneous ranges the gradient is zero, thus in the edge gradient image, the black color is dominant. The edges appear as strong lines. In color images, the Sobel filters should be calculated on all the three matrices (red, blue and green) constituents of the image.

Figure 4
The effect of the edge gradient (Sobel filter)

Using the edge filters on tomograms the boundaries of geological models can be detected. We demonstrate the effect of Sobel edge detection on filtered and non-filtered SIRT and W-SIRT tomograms. As a first step, the Sobel operator is applied to the noise-free tomogram of *Figure 1*. The result is shown in *Figure 5* (the small disturbances are caused by reconstruction errors).

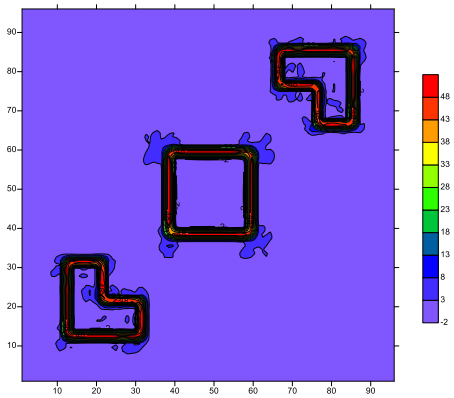

Figure 5
The effect of the Sobel edge detector on the noise-free tomogram

This picture serves as a reference for later tests, the model distances will be calculated from this image. To calculate the model distance, *Equation 9* is not applicable, because the reference image contains zero values (in the homogeneous segments). The new distance formula is

$$D = \sqrt{\frac{\sum_{j=1}^{M}\left(s_j - s_j^{(0)}\right)^2}{\sum_{j=1}^{M}\left(s_j^{(0)}\right)^2}}, \tag{12}$$

where $\boldsymbol{s_j}$and $\boldsymbol{s_j^{(0)}}$ denotes the difference values in the *j*-th cell of the actual- and the reference images, respectively, *M* is the total number of cells.

Figure 6a shows the effect of the Sobel filter on the SIRT reconstructed noisy tomogram *(Figure 2a)* while *Figure 6b* demonstrates the effect of Sobel edge detection on the Steiner filtered SIRT tomogram *(Figure 3a)*. The model distances relative to the image in *Figure 5* are D = 0.703 and D = 0.661 in the case of *Figure 6a* and *Figure 6b*, respectively.

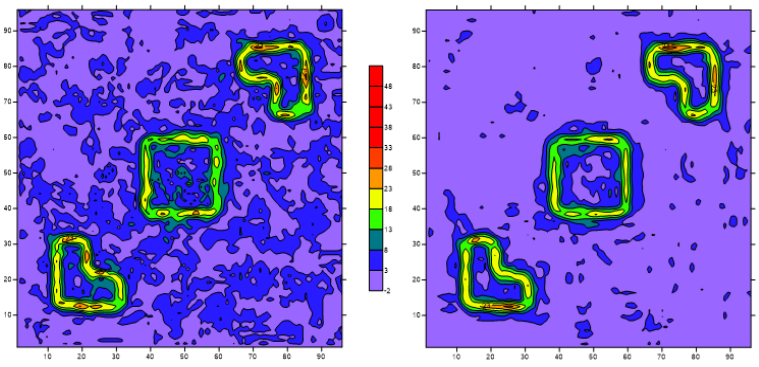

a) b)

Figure 6. *The effect of the Sobel edge detector on the a.) non-filtered and b.) Steiner-filtered SIRT tomogram*

A similar test was performed on the W-SIRT images. *Figure 7a* shows the effect of the Sobel filter on the W-SIRT tomogram (D = 0.515), while *Figure 7b* demonstrates the effect of Sobel edge detection on the Steiner-filtered W-SIRT tomogram (D = 0.495).

It can be seen that the combined use of edge detection and noise reduction by smoothing filters as well as the robust Steiner filter sufficiently improve the quality of the seismic tomographic images.

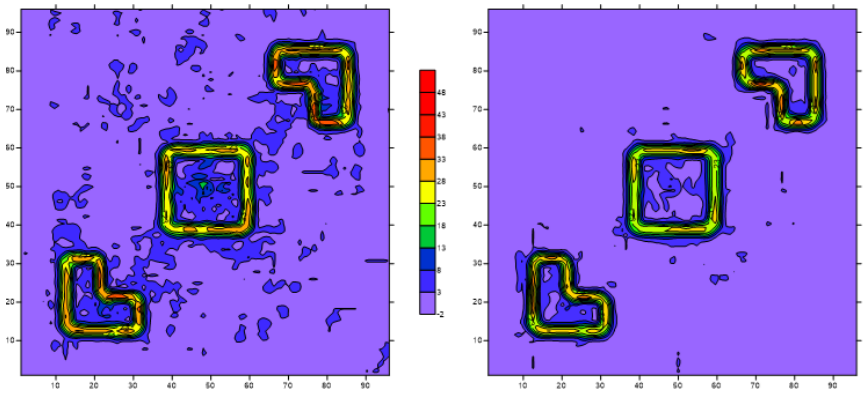

a) b)

Figure 7

The Sobel filter on a) non-filtered and b) Steiner-filtered W-SIRT tomogram

3. APPLICATION OF DEEP LEARNING IN EDGE DETECTION

Machine learning has many possible applications and opens new perspectives in many fields, including earth science. In supervised learning, the model adjusts its parameters until its output gets close to the desired output (ground truth).

To investigate the possibility of using machine learning models for the task of edge detection on noisy tomograms, we chose the U-Net architecture (Ronneberger et al., 2015), because it is the backbone of denoising diffusion models (commonly used for denoising tasks). U-Net is a fully convolutional network originally designed for semantic segmentation tasks, where the model learns to output 3 classes (foreground, background, not classified i.e. outline). To use this architecture for edge detection, we modified the original model to output 2 classes (edge, not edge). We trained the model on the BIPEDv2 dataset containing 250 images of urban scenes (Soria et al., 2023). The model performed well on the test set, and generalized quite well to other types of images, including tomographic images. Below we show our results:

In *Figure 8a* we show the noise-free tomographic picture (the same as in *Figure 1*) in a form compatible with the DL procedure. *Figure 8b* shows the edge detection result given by the (modified) U-Net architecture.

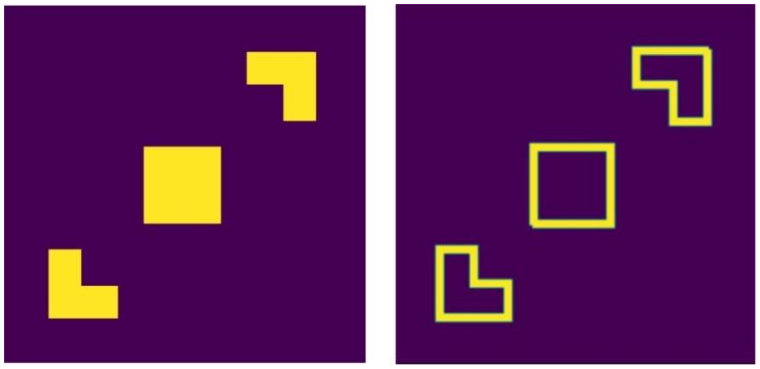

a) b)

Figure 8

a) The noise-free tomogram, b) Edge detection predicted by the modified U-Net model trained on noiseless images

In *Figure 9* the U-Net model is tested on noisy input data in the case when it is trained on noiseless images. *Figure 9a* shows (pixel-by-pixel) the non-filtered SIRT tomogram (the same data set is shown in *Figure 6a* using Golden Surfer tool) while *Figure 9b* presents edge detection given by the modified U-Net model trained on noiseless images (re-sampled to 128 × 128 pixels). As it was expected, the edges are well detected but the image is noisy.

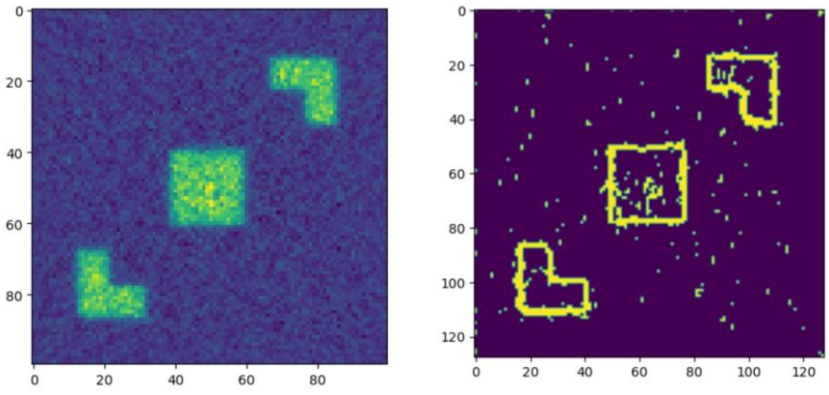

a) b)

Figure 9

a) The noisy SIRT tomogram, b) Edge detection predicted by the modified U-Net model trained on noiseless images

To be able to detect edges on noisy images, we added random Gaussian distributed noise to the BIPEDv2 dataset and trained the modified U-Net model on this new dataset, the desired output being the noiseless edge maps, as previously. *Figure 10* shows our result.

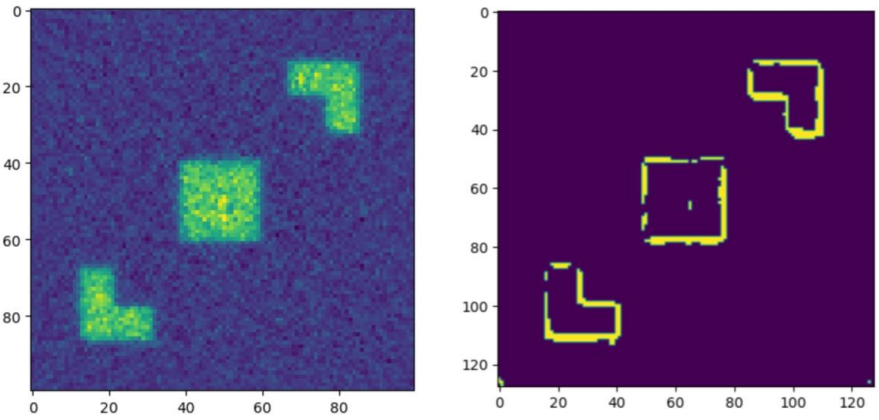

a) b)

Figure 10

a) The noisy SIRT tomogram, b) Edge detection predicted by the modified U-Net model trained on noisy images

The traditional (Sobel-filtered) and the new (DL-produced) edge detection of the noisy SIRT tomogram (shown in *Figure 2a*) can be compared. *Figure 11a* is the same as *Figure 6a* presenting the effect of the Sobel edge detector on the non-filtered SIRT tomogram. *Figure 11b* shows the edge detection result given by the Deep Learning procedure on the same SIRT tomogram. For the sake of comparability, the two files are presented in the same format. It can be seen that the DL procedure has sufficient noise rejection capacity, or in other words, it has robust features.

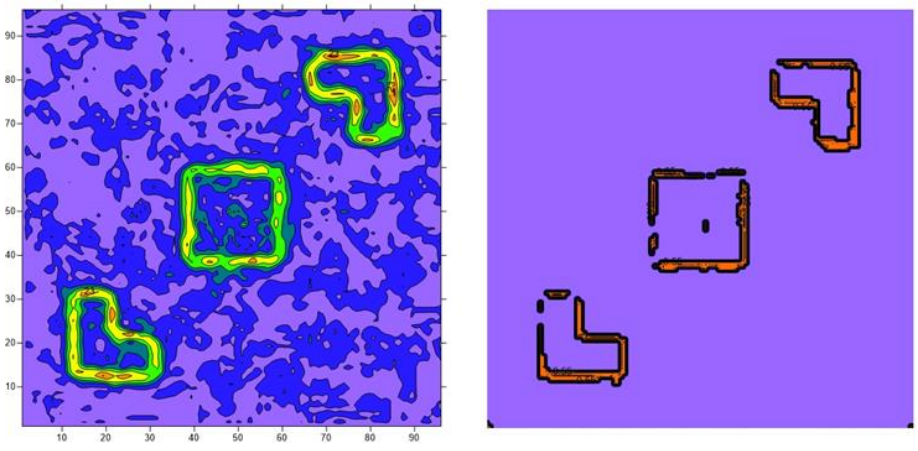

a) b)

Figure 11

a) The effect of the Sobel edge detector on the non-filtered SIRT tomogram b) the edge detection result given by the Deep Learning procedure

Of course, DL edge detection can be used in a broader range of earth sciences phenomena. As an example, we demonstrate a seismic application for edge detection in *Figure 12*.

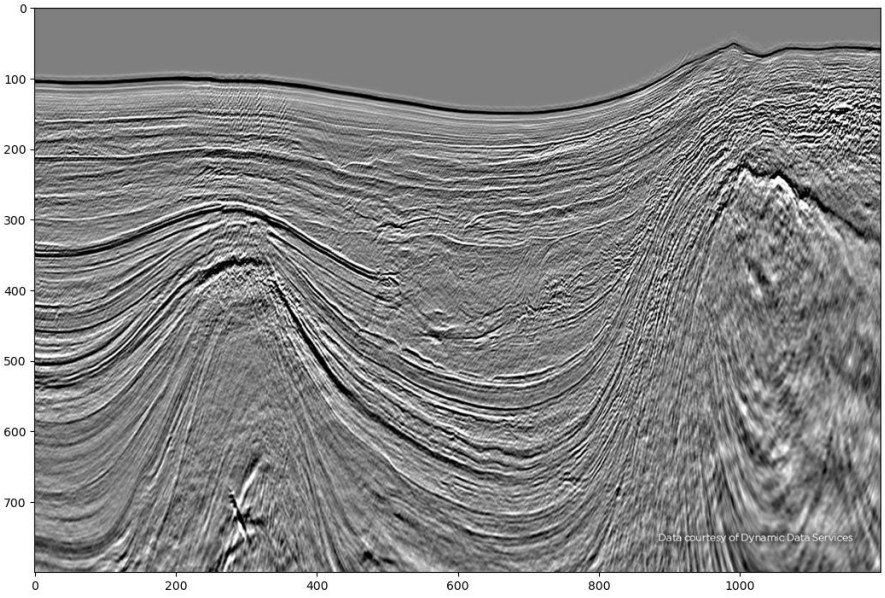

a)

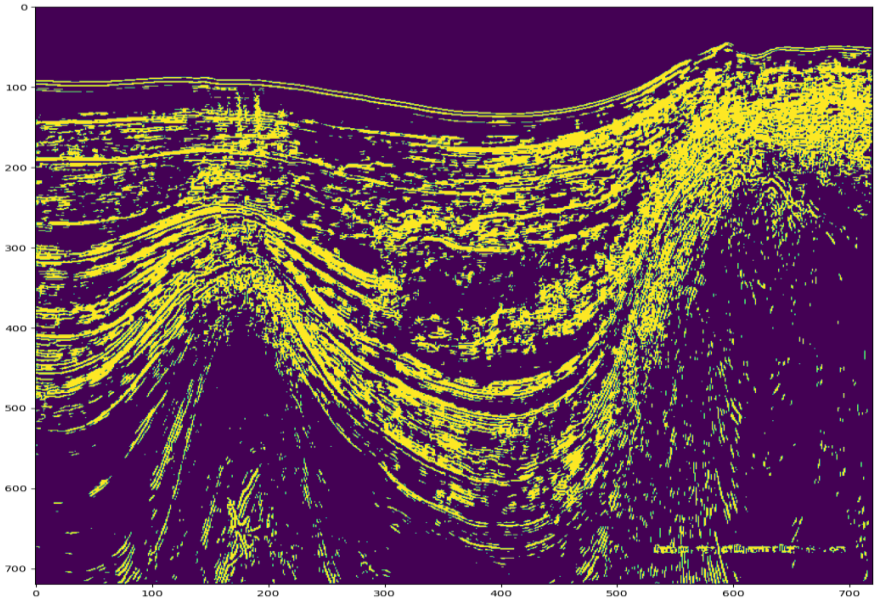

b)

Figure 12

a) Reflection seismic section as input and b) its DL edge detection image

4. CONCLUSIONS

In geophysical inversion, tomographic reconstruction, image processing and in the case of many interpretation procedures, it is of main importance to keep under control the propagation of data errors to the model space independently (as much as possible) of the statistical distribution of the noise. The methods fulfilling these requirements are usually called as robust. In the paper, we present two ways to perform robust edge detection. At first, remaining in the framework of traditional image processing a robust Cauchy–Steiner filter is used to improve the quality of edge detection in tomographic images. In the second part of the paper Deep Learning algorithm developed for edge detection is shown and investigating its noise sensitivity the robustness of the method is demonstrated.

As a new robust tool in image processing, the Steiner filter is introduced, in which the Most Frequent Value method developed by Steiner (1988) is applied to calculate the elements of the convolution mask. The effect of the filter was tested on medium-sized tomographic pictures. It was shown that the quality of the tomogram can be further improved by using the new filter. It was found that the Steiner filter acts as a robust tool and can be successfully applied also in edge detection tests.

Rather than establishing the parameter changes locally (pixel-by-pixel), Deep Learning tools can also be used as global alternatives to traditional image processing. In the second part of the paper, we applied the U-Net Convolutional Network architecture (UNCN), which is a widely used Deep Learning procedure developed for image segmentation. The method was tested on the same datasets used in the investigation of traditional image processing. The results show that the U-Net architecture can be applied to edge detection tasks and can be trained to solve edge detection and denoising tasks simultaneously. Based on this, it can have wide applications in applied earth sciences.

ACKNOWLEDGMENTS

The research was funded by the Sustainable Development and Technologies National Program of the Hungarian Academy of Sciences (FFT NP FTA). The first author is grateful for the support. The research was also supported by the National Research, Development and Innovation Office (NKFIH), Hungary, under project no. K-135323. The third author is grateful for the support.

REFERENCES

Nolet, G. (1987). Seismic wave propagation and seismic tomography. In: Nolet, G. (ed.): *Seismic Tomography.* Seismology and Exploration Geophysics. Vol. 5. Dordrecht, Springer.

Herman, G. T. (2009). *Fundamentals of computerized tomography: image reconstruction from projections.* 2nd ed. Dordrecht, Springer.

Scales, J. A., Gersztenkorn, A., Treitel, S. (1988). Fast Lp solution of large, sparse, linear systems: Application to seismic traveltime tomography. *Journal of Computational Physics*, 75 (1), pp. 314–333.

Amundsen, A. L. (1991). Comparison of the least-squares criterion and the Cauchy criterion in frequency-wavenumber inversion. *Geophysics*, 56, pp. 2027–2038.

Steiner, F. (1988). Most frequent value procedures. (A short monograph). *Geophysical Transactions*, 34 (2–3), pp. 139–260.

Dobróka, M. and Szegedi, H. (2014). On the generalization of seismic tomography algorithms. *American Journal of Computational Mathematics*, 4, pp. 37–46. https://doi.org/10.4236/ajcm.2014.41004

Kale, U. and Dobróka, M. (2016). An introduction to robust tomography methods. *Geosciences and Engineering*, 5 (8), pp. 98–110.

Ronneberger O., Fischer P., & Brox T. (2015). U-net: Convolutional networks for biomedical image segmentation. *Medical Image Computing and Computer-Assisted Intervention–MICCAI 2015: 18th International Conference*, Munich, Germany, October 5–9, 2015, proceedings, part III 18. Springer International Publishing, pp. 234–241, https://doi.org/10.48550/arXiv.1505.04597

Soria X., Sappa A., Humanante P., & Akbarinia A. (2023). Dense extreme inception network for edge detection. *Pattern Recognition*, 139, 109461. https://doi.org/10.1016/j.patcog.2023.109461

Geosciences and Engineering, Vol. 12, No. 1 (2024), pp. 139–148.
https://doi.org/10.33030/geosciences.2024.01.010

WHY FAILURES IN GEOTECHNICS ARE LESS FREQUENT THAN PREDICTED?

JOZSEF GARAI[1*], ZSOLT VADAI[2], IMRE KOVACS[3]
[1*]*Department of Civil Engineering, University of Debrecen, Hungary,*
jozsefgarai29@gmail.com
[2*]*Department of Civil Engineering, University of Debrecen, Hungary,*
vadai.zsolt@gmail.com
[3*]*Department of Civil Engineering, University of Debrecen, Hungary,*
dr.kovacs.imre@gmail.com
[1*]*https://orcid.org/0000-0001-8194-2697*
[2]*https://orcid.org/0000-0002-3519-9852*
[3]*https://orcid.org/0000-0002-7591-8946*

Abstract: One of the most important unresolved problems in geotechnical risk assessment is that "Why are failures less frequent than our reliability studies predict?" In order to answer this question the safety requirements of Eurocode 7 have been investigated. It has been concluded that the safety of soil mechanics parameters, defined by probability requirements, does not included in the calculated Overall Factor of Safety, which represents the overall reliability of a geotechnical design. Method, how to convert the probability requirements to factor of safety is proposed. Incorporating the probabilistic safety of soil mechanics parameters into the Overall Factor of Safety results in a reliable estimation for the failure of geotechnical structures.

Keywords: *Factor of safety, Overall Factor of Safety, EUROCODE 7, probabilistic safety requirements*

1. INTRODUCTION

John T. Christian and Gregory B. Baecher (2011) list the ten most important unresolved problems in geotechnical risk and reliability. The number one question in this list is "Why are failures less frequent than our reliability studies predict?". In order to answer this question the safety requirements of Eurocode 7 (EC7) are investigated.

The EC7 employs the limit state design criteria (Harris and Bond, 2012). The limit states are defined as "state beyond which the structure no longer fulfills the relevant design criteria". There are two limit states in EC7, the Ultimate Limit State (ULS) and Serviceability Limit State (SLS). The Ultimate Limit State is associated with the collapse or with other similar form of structural failure, like the failing of a foundation due to insufficient bearing resistance. The Serviceability Limit State corresponds to specific service requirements of the structure, which must be satisfied. One example could be – limiting the excessive non-uniform settlement. The aim of the design is to make sure these limit states are not exceeded (Gulvanessian et al., 2002). The safety of a geotechnical design is described by the Overall Factor of Safety (OFS), which is defined as the

ratio of the characteristic values of the resistance and the actions (Frank et al., 2013). In geotechnics, the uncertainties affecting the structures arouse from the soil layering, soil properties, actions, and resistances. In order to avoid both ULS and SLS failing, the allowed uncertainties in geotechnical designs are regulated. The uncertainties of the deferent contributing factors are limited by imposing factor of safety, probabilistic, or risk analysis requirements. These methods are summarized.

2. METHODS ENSURING SAFETY REQUIREMENTS

2.1. Factor of safety

This is the classical engineering method used for estimating the chance of failing. The method modifies the expected value relating to collapse by adding/deducting a constant or by multiplying/dividing with a factor.

Constant value for safety is used when the uncertainty is independent from the value of the risk component. An example could be the design value of Ground Water Level (GWL_d). The uncertainty in the estimation of the GWL is independent of its elevation. Thus the safety (F_s) is a constant and added to the characteristic value, when the design value is calculated.

$$GWL_d = GWL_c + F_s \tag{1}$$

If the uncertainty is proportional to the size of the investigated risk component, then the factor of safety is a multiplier of the base or the characteristic value. An example might be the relationship between the load and deformation or settlement (Atkinson, 2007). The load relating to collapse (q_c) gives the Ultimate Limit State with and excessive settlement. This can be avoided through the introduction of the factor of safety (f_s), which reduces the load to an allowable or safe load (q_s) *(Figure 1)* as:

$$q_s = \frac{1}{f_s} q_c \tag{2}$$

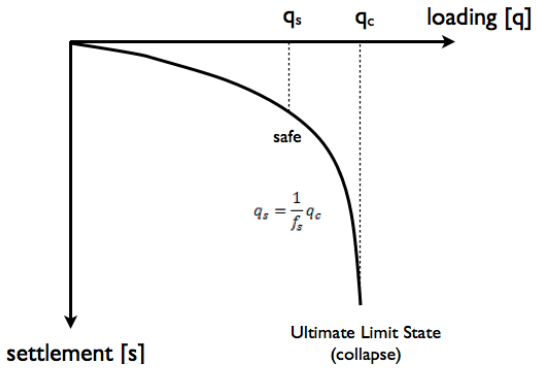

Figure 1

The essentials of Ultimate Limit State and the factor of safety are shown, where q_c is the load relating to failure or collapse and q_s is the safe load allowed by the standard. The factor of safety is $f_s = q_c/q_s$.

The factor of safety can be taken into consideration by using a lump value, which combines all the contributions of uncertainties, or through the introduction of partial factors representing the different sources of the uncertainties separately. The EC7 divides the uncertainties and uses partial factors to take into consideration the safety of the actions and the resistances.

2.2. Probabilistic method

Probabilistic method requires that failure should not occur more often than a giving probability. For soil parameters EC7 requires 95% confidence level for geotechnical designs. Thus 5 percent of the given parameters can have lower or higher value, which ever is safer, than the characteristic value of the parameter used for the design *(Figure 2)*.

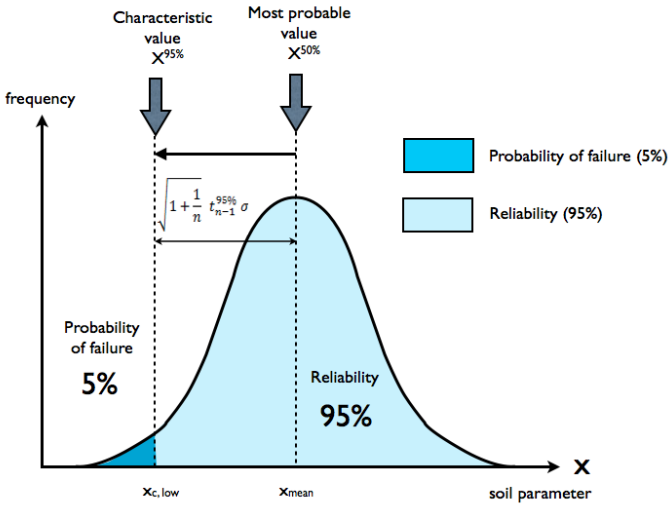

Figure 2

Probabilistic approach defines the characteristic values of soil parameters. The safety is introduced by reducing the most probable value of the parameter, $X_{mean} = X^{50\%}$, to the characteristic value of the parameter relating to 95% confidence level

In most of the cases it can be assumed that the probability distribution is normal and that student or t distribution can describe the convergence to this distribution. The calculation of the characteristic value then requires 2 statistical parameters, the arithmetic mean, and the standard deviation, which sometimes called variance, or the coefficient of variation (Schneider & Schneider, 2013). The characteristic value of a soil parameter (X_c) can be calculated then as:

$$X_c = X_{mean} \pm \sqrt{1+\frac{1}{n}}\, t_{n-1}^{95\%}\sigma \tag{3}$$

or

$$X_c = X_{mean}\left(1 \pm \sqrt{1+\frac{1}{n}}\, t_{n-1}^{95\%}\, c_v\right) \tag{4}$$

where n is the number of data, and X_{mean} is the value of the mean, which can be calculated as:

$$X_{mean} = \frac{\sum_{i=1}^{n} X_i}{n} \tag{5}$$

σ is the standard deviation, calculated as:

$$\sigma = \sqrt{\frac{\sum_{i=1}^{n}(X_i - X_{mean})^2}{n-1}} \tag{6}$$

c_v is the coefficient of variance, calculated as:

$$c_v = \frac{\sigma}{X_{mean}} \tag{7}$$

and $t_{n-1}^{95\%}$ is the student distribution parameter for n-1 freedom at 95% confidence level.
The characteristic value of the mean at 95% confidence level can be calculated as:

$$X_{c,mean} = X_{mean} + \sqrt{\frac{1}{n}}\, t_{n-1}^{95\%}\, \sigma \tag{8}$$

Despite the different forms, *Equations (3)* and *(4)* are identical. The characteristic values for known distributions can be calculated by using the t value of $t_{\infty}^{95\%} = 1.646$.

2.3. Probability risk analysis

The Hazard (H), the Vulnerability (V), and the Element at Risk (E) are estimated. The product of these three factors defines the Risk (R) (Cetina & Uzielli, 2012) as:

$$R = H \times V \times E \tag{9}$$

where H is the probability of particular threat occurring within a particular set of time ($P \times time^{-1}$), where P is the probability of the occurrence of the event. Vulnerability is the degree of loss to an element or a set of elements within the area affected by the hazardous event. It is expressed in the scale of 0 (no loss), and 1 (total loss). E is the value of the caused damage by the disaster; including repair and maintenance cost of the vulnerable assets. It can be expressed in monetary value, life etc. The risk is the probability of an adverse event multiplied with the consequences if the event occurs. The unit of risk is: probability $\times$value$\times time^{-1}$

3. THE UNCERTAINTIES REGULATED BY EC7

If the design is carried out by calculation method, then the uncertainties in civil engineering are emerging from three sources, actions, materials and resistance. In geotechnical engineering there is an additional source of uncertainty, which arises from the uncertainty of the spatial extent of the soil layering. The EC7 treats these four

uncertainties separately and uses different methods in order to ensure the required safety standard/s.

- The uncertainties arising from the actions and the resistant are taken into consideration by the application of standardized partial safety factors.
- The uncertainties of the material represented by the soil parameters in geotechnics. Using probabilistic method, the safety is insured by changing the value of the soil parameter from the most probable value relating to 50% confidence to 95 % confidence level. The value of the parameter at 95% confidence level defined as the characteristic value of the soil parameter. Depending on the design, either the characteristic value of the mean or the weak value can be used *(Figure 3)*.

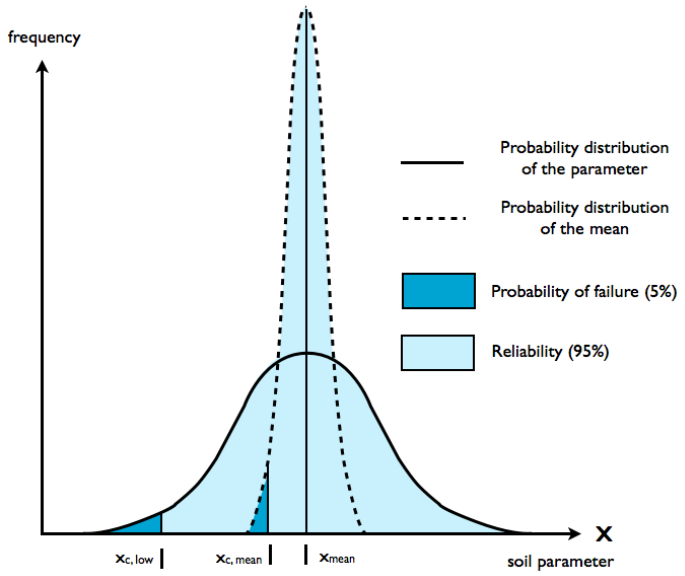

Figure 3

Probability distribution of the soil parameter and the probability distribution of the mean are shown. The characteristic values for the mean and the low or weak values are shown

If the overall stability is investigated, where the resistance can be averaged out, then the characteristic value of the mean should be used *(Equation 8)*, like calculating the weight from the unit weight or cohesion and internal friction in shaft resistance. On the other hand investigating a local equilibrium, like bearing capacity, where the weak value *(Equations 3, 4)* of the parameters should be used ***(****Figure 4****)***. The characteristic low values of the soil parameters many times would result in a very conservative (non-economical) design. In such cases it might be advisable and economical to intensify the ground investigations and determine the local mean soil parameters of these locations.

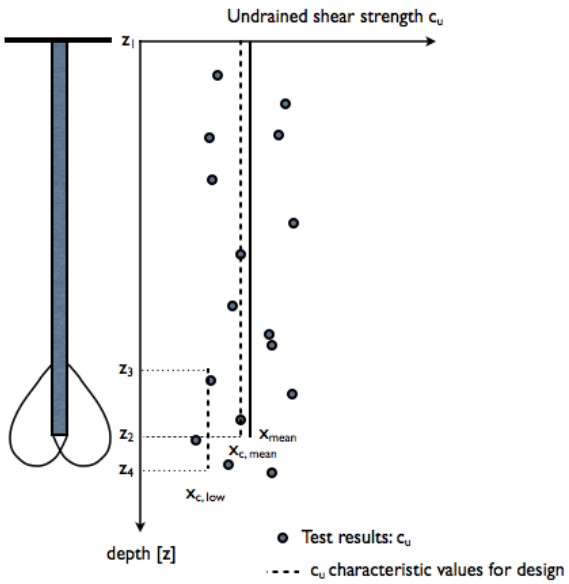

Figure 4

Investigating the overall stability of a structure, where the resistance can be average out, like the shaft resistance of the pile, the characteristic value of the mean should be used. For local equilibrium, where the resistance cannot be averaged out, like the bearing capacity of the pile, the low or weak value of the characteristic parameter should be used. Characteristic values of undrained shear strength for the design of pile shaft (z_1-z_2) and base resistance (z_3-z_4) are shown (Frank et al., 2013)

- The uncertainty in the spatial extent of the soil layering is taken into consideration by employing probability risk analysis. The design works are classified into categories, based on the complexity of the structure, the ground conditions, the loading, and the level of risk that is acceptable for the purposes of the structure. For each category recommendations are given to the required extent of site investigation and to the amount of effort in the checking of the design. The regulation does not quantify the risk but gives recommendation/s for the extent of the exploration, which is proportionate with the accepted level of risk.
- The Overall Factor of Safety (OFS), which represents the overall reliability of a geotechnical structure, is defined as the ratio of the characteristic values of the resistance and the actions. The problem with this representation of the total safety of a geotechnical design is that the calculated OFS does not include the safety of the soil mechanic parameters introduced by probabilistic requirements *(Figure 5)*.

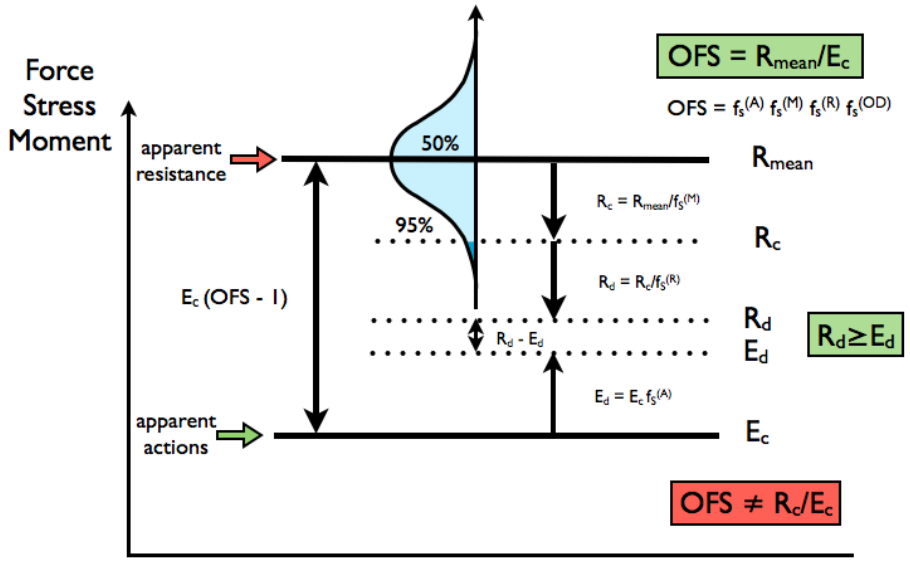

Figure 5

It is shown that the current recommendation of EC7 calculating the OFS as the ratio of R_c and E_c is incorrect. The uncertainty of soil parameters should be incorporated into the overall factor of safety as: $OFS = \frac{R_{mean}}{E_c}$.

The characteristic value of the soil mechanics parameters, which is used to calculate the resistance, represents the 95% confidence levels of the parameters. The increase of the confidence level from 50 to 95 induces safety in the values of the soil mechanics parameters. The current recommendations of EC7 do not incorporate this safety into the OFS. Neglecting the safety built into the soil mechanics parameters makes the geotechnical risk analysis unreliable (Ivandić et al., 2022). In order to incorporate the safety of soil parameters into the OFS, the safety induced by probabilistic requirements must be converted into factor of safety and vice versa *(Figure 5)*. EC7 does not give recommendations, how the safeties introduced by probabilistic method and factor of safety can be converted into each other.

4. CONVERTING PROBABILITY REQUIREMENTS TO FACTOR OF SAFETY

The safety introduced by changing the value of the soil parameter from 50 to 95 percent confidence level might be described as the ratio of the two confidence levels. Based on EC7 this value would be 1.9 for geotechnical designs. However, this "probability safety" is not equivalent with the conventional factor of safety used in engineering. Thus the safety calculated by probability method cannot be directly incorporated into the calculation of OFS.

In order to comply with the traditional factor of safety approach, which is used for the actions and resistance, the safety of the soil parameters should be considered

as the ratio of the resistances calculated by using the soil parameters at 50% and 95% confidence levels. Thus the partial factor of safety for the soil parameters (f_s^{soil}) should be defined as:

$$f_s^{soil} \equiv \frac{R_{mean}}{R_c} \tag{10}$$

where R_c is the characteristic value of the resistance calculated from the 95% confidence level soil parameters, and R_{mean} is the most probable resistance calculated from the mean value of the soil parameters, which relates to 50% confidence level.

5. OVERALL FACTOR OF SAFETY

Converting the safety, introduced by probabilistic method, to factor of safety allows incorporating this safety, representing the uncertainty of the material or soil parameters, into the OFS. It is suggested that the Overall Factor of Safety should be defined *(Figure 5)* as:

$$OFS \equiv \frac{R_{mean}}{E_c} \tag{11}$$

The partial factor of safeties (f_s) representing the different source of uncertainties, actions (A), soil/material (M), and resistance (R) can also be calculated separately.

- The partial factor of safety for the action ($f_s^{(A)}$) can be calculated as:

$$f_s^{(A)} = \frac{E_d}{E_c} \tag{12}$$

where E_d is the design and E_c is the characteristic values of the effects of all actions. EC7 defines the characteristic value of the actions as:

$$E_c = \sum_{j\geq 1} G_{c,j} + P + Q_{c,1} + \sum_{i>1} \Psi_{0,i} \times Q_{c,i} \tag{13}$$

where $G_{c,j}$ are the permanent actions, P is the prestress, $Q_{c,1}$ is the leading variable action, $Q_{c,i}$ is the accompanying variable actions, and $\Psi_{0,i}$ is the combinations factor of the variable actions.

- The partial factor of safety for the resistance ($f_s^{(R)}$) is:

$$f_s^{(R)} = \frac{R_c}{R_d} \tag{14}$$

where R_c and R_d are the characteristic and the design values of the effects of all resistance respectively. The defined partial factor $f_s^{(R)} \geq \gamma_R$, where γ_R is the partial factor for resistance in EC7

● The partial factor for the material ($f_s^{(M)}$) or soil in geotechnics should be calculated as given in Equation (10) as:

$$f_s^{(M)} = f_s^{soil} = \frac{R_{mean}}{R_c} \tag{15}$$

If $R_d = E_d$, most economical design, then the OFS is the product of the partial safety factors, contributing to the safety of the structure.

$$OFS = f_s^{(A)} \times f_s^{(M)} \times f_s^{(R)} \tag{16}$$

If $R_d > E_d$, then an additional factor of safety ($f_s^{(OD)}$), representing the factor of over design, which is introduced as the ratio of R_d and E_d:

$$f_s^{(OD)} \equiv \frac{R_d}{E_d} \tag{17}$$

The OFS in general case can be defined then as:

$$OFS \equiv f_s^{(A)} \times f_s^{(M)} \times f_s^{(R)} \times f_s^{(OD)} \tag{18}$$

Falling or the collapse or damage of the structure occurs when the value of the Overall Factor of Safety falls below one. Thus it is possible partial factor/s of safety fall below one without resulting in the failing of the structure as long as the OFS > 1 condition is satisfied.

Please note that the safety relating to the uncertainty of the spatial extant of the soil layers has no contribution to the OFS. The uncertainty of the soil layers is taken into account by regulations, which defines the extent and detail of the explorations in accordance to the risk assessment. The safety has been achieved by more detailed exploration and not by making the structure stronger. The safety required for the soil layering is not quantified.

6. CONCLUSIONS

The current version of EC7 defines the allowed uncertainties, emerging from different sources, by recommending different methods for the requirements of safety. No recommendation is given how the required safety of the different methods can be converted into each other. In order to overcome on this problem, a method, transferring the probabilistic safety requirements to factor of safety is proposed. Converting the probabilistic values of soil parameters into a partial factor of safety allows incorporating this uncertainty in the Overall Factor of Safety. Incorporating the probabilistic safety of the soil parameters into OFS increases its value approximately from 2 to 3. Thus, the proposed definition of the Overall Factor of Safety gives a reliable description of the safety of geotechnical designs and explains, “Why failures in geotechnics are less frequent than predicted” when the current recommendations of EC7 are used.

References

Atkinson, J. (2007). *The Mechanics of Soils and Foundations.* Second Edition. London and New York, Taylor & Francis Group.

Cetina, Z. M. and Uzielli, M. (2012). *Risk and Geotechnical Engineering.* ISSMGE webinar. https://www.issmge.org/education/recorded-webinars/risk-and-geotechnical-engineering.

Christian, J. T. and Baecher, G. B. (2011). Unresolved Problems in Geotechnical Risk and Reliability. *GeoRisk*, Atlanta, Georgia, USA, June 26–28.

Frank, R., Bauduin, C., Driscoll, R., Kavvadas, M., Krebs Ovesen, N., Orr, T., and Schuppener, B. (2013). *Designers' Guide to Eurocode 7: Geotechnical Design*. London, IEC Publishing.

Gulvanessian, H., Calgaro, J-A., and Holicky, M. (2002). *Designers' Guide to EN 1990: Eurocode: Basis of Structural Design*. London, UK, Thomas Telford Publishing.

Harris, A. J., and Bond, A. J. (2012). Stability of earthworks to Eurocode 7. *Geological Society, London, Engineering Geology Special Publications*, 26 (1), pp. 9–19. https://doi.org/10.1144/EGSP26.0

Ivandić, K., Dodigović, F., Soldo, B., Kovačević, S. (2022). Probabilistic Evaluations of Prescribed Safety Margins in Eurocode 7 for Spread Foundations. *Periodica Polytechnica Civil Engineering*, 66 (3), pp. 710–719. http://doi.org/103311/PPci.18212

Schneider, H. R., and Schneider, M. A. (2013). Dealing with uncertainties in EC7 with emphasis on determination of characteristic soil properties. In: Arnold, P. et al. (eds.): *Modern Geotechnical Design of Practice.* IOS Press, pp. 87–101.

Responsible: Prof. dr. Péter Szűcs Vice-Rector
Published by the Miskolc University Press under leadership of Attila Szendi
Responsible for duplication: Erzsébet Pásztor
Technical editor: Csilla Gramantik
Proofreader: Zoltán Juhász
Number of copies printed:
Number of permission: MERT-2024-305-ME
HU ISSN 2063-6997